STATIC AND DYNAMIC PROPERTIES OF RECONFIGURABLE MAGNETO-ELASTIC METASTRUCTURES

A Dissertation
Presented to
The Academic Faculty

By

Marshall Schaeffer

In Partial Fulfillment
of the Requirements for the Degree
Doctor of Philosophy in the
School of George W. Woodruff School of Mechanical Engineering

Georgia Institute of Technology

December 2016

STATIC AND DYNAMIC PROPERTIES OF RECONFIGURABLE MAGNETO-ELASTIC METASTRUCTURES

Approved by:

Dr. Massimo Ruzzene, Advisor
Daniel Guggenheim School of Aerospace Engineering
George W. Woodruff School of Mechanical Engineering
Georgia Institute of Technology

Dr. Michael Leamy
George W. Woodruff School of Mechanical Engineering
Georgia Institute of Technology

Dr. Alper Erturk
George W. Woodruff School of Mechanical Engineering
Georgia Institute of Technology

Dr. Aldo Ferri
George W. Woodruff School of Mechanical Engineering
Georgia Institute of Technology

Dr. Julian Rimoli
Daniel Guggenheim School of Aerospace Engineering
Georgia Institute of Technology

Dr. Karim Sabra
George W. Woodruff School of Mechanical Engineering
Georgia Institute of Technology

Date Approved: November 11, 2016

The fear of the LORD is the beginning of wisdom,

and knowledge of the Holy One is understanding.

Proverbs 9:10

To Rachel, my beloved wife, who bore the hardship of research with me

ACKNOWLEDGEMENTS

I will start by thanking Dr. Ruzzene, my advisor, for the opportunity to work under his guidance. He has provided opportunities for education in and beyond my research, which I would otherwise be without.

I would also like to thank my committee members Dr. Michael Leamy, Dr. Alper Erturk, Dr. Aldo Ferri, Dr. Julian Rimoli, and Dr. Karim Sabra. I have enjoyed learning from all of you and appreciate you being on my committee. In addition, thank you to Dr. Fabrizio Scarpa for hosting me at the University of Bristol on two occasions.

Thank you to Shane Lympany, William Storrs, and Akshay Umashankar for your research as part of your undergraduate education. You helped not only my research, but my own development as well.

To the many students and researchers from the US and around the world whom I worked alongside: Erik, Alberto, Nicola, Guglielmo, Yonqiang, Hannah, Matteo, William, Sepide, Yuan, Not, and Akio. You will not be forgotten. I acknowledge especially Aaron, Raj, and Giuseppe, with whom I was able to work closely at the end of my Ph.D. You have all shaped my perspective for better and helped me succeed.

Thank you to Alex Zelhofer, who provided a key FE calculation for the final pieces of my thesis! Also to my friends and family, too many to name, who have helped me to and through this point.

Finally, to my dear friend and lab-mate Olivier, whose friendship brought me through many obstacles.

Thank you.

TABLE OF CONTENTS

LIST OF FIGURES

SUMMARY

This thesis presents the investigation of lattice structures for the purpose of providing novel pathways for wave and mechanical property control. Structures of the type studied are often called "metamaterials" or "metastructures" as they behave in a way that is beyond their constituents. Magneto-elastic lattices are the primary focus, since they are generally multistable, allowing one structure to assume various geometric configurations, which can correspond to various functional modes, providing the possibility for adaptive structures. Periodic structures are considered for their unique wave properties, as well as for ease of design and application, including: 2D hexagonal, re-entrant, and kagome lattices.

A fundamental step to the analysis of reconfigurable structures is the identification of possible stable configurations. By minimizing energy a variety of configurations are identified for further study. A method for transition from one stable configuration to another is required to make use of the reconfiguration. So, dynamic reconfiguration is investigated as a fast and versatile method for switching configurations via transient numerical simulations. Bloch wave analysis is applied to models of magneto-elastic lattices to investigate the possible wave propagation changes. The introduction of anisotropic wave propagation, opening of bandgaps, and changes in wave speeds are observed as a result of geometric lattice reconfiguration. Reconfiguration also drastically effects static properties. The equivalent continuum properties of magneto-elastic lattice structures are calculated using a homogenization methodology. Reconfiguration from hexagonal to re-entrant lattices produces over an order of magnitude change in stiffness while converting the lattice from having isotropic to orthotropic properties.

While magneto-elastic structures are the primary focus, this thesis also addresses two other topics relevant to the development of periodic structures that seek to control wave energy. The first, pursuing novel wave control, is topologically protected edge modes, or edge states. Building by analogy from quantum mechanics, elastic mechanical structures

are designed that carry special waves modes, which are termed helical edge states, in only one direction along a lattice boundary. A hexagonal and Lieb lattice are investigated as examples of a methodology developed which defines a family of mechanical lattices that can exhibit such wave modes. Analytical approaches predict the phenomena and numerical simulations verify the predictions. Another topic is the development of a methodology for measuring in-plane waves in lattice structures, which is needed for the experimental validation of the theoretical wave propagation results found in this thesis. In-plane waves modes are very common in metastructures research, but there is presently no easy way to measure such waves. As a new methodology, digital image correlation is combined with high-speed photography. The transient propagation of in-plane waves in an elastic hexagonal honeycomb lattice is measured to develop the method, and comparisons are made to finite element predictions to show the efficacy.

CHAPTER 1
INTRODUCTION

1.1 Chapter overview

The goal of this thesis is to investigate the properties of lattice structures for the purpose of providing novel avenues for wave and mechanical property control. Structures of the type studied are often called "metamaterials" or "metastructures." Magneto-elastic lattices are the primary focus, in order to make use of their multistability for property control, and both static and dynamic properties are considered. This chapter first overviews the field of metastructures as it relates to this thesis. Next, the motivations for this thesis and its objectives are discussed. Finally the scientific contributions of this work are listed and the organization of the document is summarized.

1.2 Reconfigurable metastructures

1.2.1 Metastructures

In the endeavor to produce structures that are more useful, effort has been directed towards periodic structures, in which the architecture of a small-scale local structure, *i.e.* a unit cell, can be designed to control the properties of a global system. Such structures are comprised of repeating patterns and are attractive, in part, because the chosen geometry can often give the global structure properties that are much different and more desirable than the material from which the structure is made. Furthermore, studying only a unit cell is often sufficient to characterize a large system, which aids in the modeling and design process. Two of the most prominent positive attributes of periodic structures is their ability to be extremely stiff for their weight, or to exhibit novel wave propagation properties [1, 2, 3, 4, 5, 6]. Acoustic and phononic metamaterials or metastructures are periodic structures

used to control mechanical waves. The architecture of the unit cell controls the flow of wave energy, affecting the speed and direction at which energy flows as a function of its wave number and frequency. A common result of these dispersive properties of metastructures is the "wave beaming" phenomenon [7]. Bandgaps can also occur that prevent waves at certain frequencies from propagating through the system. The aforesaid wave properties are highly dependent on lattice geometry as well as stiffness and mass distributions. Changing the geometry and stiffness/mass distribution within a lattice therefore provides the means of tailoring and controlling wave motion and the subsequent onset of vibrations. Wave propagation control finds application in methods for isolation of vibrations in rotating machinery [8], for the protection of important locations (such as the brain) from waves resulting from blasts and impacts through their steering and redirection [9], for the harvesting of mechanical energy and its conversion for power generation by forming wave lenses and reflectors [10], or for the processing of acoustic wave signals [11].

1.2.2 Dynamic reconfiguration

When the units comprising a structure are bistable or multistable, the structure may reconfigure into geometries with different internal configurations, and/or global shape. Each unique configuration is a static equilibrium, *i.e.* a local potential energy minimum. Magnetoelastic systems generally have the ability to be multistable [12, 13], which makes them good candidates for the design of periodic lattices with geometries that can be toggled [14]. Changes in structural properties due to static or quasi-static reconfiguration have already been investigated, for example, in [15, 16, 17, 18, 19]. However, in order to access a richer set of final configurations and to find paths for faster transitions, dynamic lattice reconfigurations should be considered. The specifics of the dynamic reconfiguration can determine how certain regions of a structure reconfigure, allowing local property control and grading. A fast rate of reconfiguration could be valuable in applications intended for protection from short events and shocks that can damage organs, electronics, or other delicate objects. The

reconfiguration itself can even be a way of redirecting, dissipating, and storing incoming energy without damaging the protective structure, similar to the example given by [20].

One dimensional (1D) systems composed of bistable interactions have received attention for of their dynamic reconfiguration, including the study of "transition front" propagation, or the rate at which reconfiguration occurs [21, 22, 23, 24, 25]. The energy profile of bistable interactions, *i.e.* how the interaction potential varies with the distance between interacting entities, provides important insight into the paths leading to changes and the initial and final static configurations. The ability to shape such profiles could be the primary means by which the dynamic reconfiguration of a structure is designed. Of importance is the identification of energy minima which determine equilibrium configurations, and the estimated amount of energy required for reconfiguration. While the previously mentioned references focus on more general systems, dynamic reconfiguration has also been studied specifically to understand martensitic transformation in shape memory alloys, which includes both 1D [26, 27] and 2D [28, 29] studies. In contrast to 1D dynamic reconfiguration investigations, the study of 2D systems is still in need of much attention.

1.2.3 Wave propagation in reconfigurable lattices

The dependence of wave motion in a lattice on unit cell geometry has been extensively investigated. For example, differences of in-plane wave propagation between hexagonal and re-entrant lattices are investigated in [7, 30]. The effect on lattice undulations on wave propagations are studied in [31]. Similarly, the volume fraction and skewness of rhombic grid lattices are shown to greatly affect wave speed and directionality in [32]. As structures transition from near-continuum to beam lattices, wave beaming is a prominent phenomena that arises. Furthermore, increasing the skewness of the lattice affects the direction in which beaming occurs. Similarly, rotation of lattice components can be exploited to tune bandgaps in a reversible way [17, 33, 34, 19]. Specifically, in [17] and [19] the configuration of a highly deformable 2D structure changes as it buckles under a compressive load.

Periodic 2D systems of high-density rectangular inclusions in a fluid are investigated in [33, 34], where the rotation of the high-density inclusions is the mechanism used to tune bandgaps.

All of the aforementioned studies demonstrate that large changes in wave propagation can be induced by changing lattice geometry. Hence, the concept of adapting the mechanical wave properties of a structure through unit cell geometric reconfiguration is of interest [17, 33, 34], as it leads to the design of components with adaptive and programmable dynamic behavior. In this context, lattices featuring multiple stable equilibrium configurations, which are intrinsic to the structure, are of particular interest. Structures exhibiting more than one intrinsic stable configuration allow switching between operational modes associated with different dispersion, bandgap, and beaming properties, *i.e.* wave propagation properties, without the need for the continued application of an external control action. Such reconfiguration may allow, for example, a filter that can switch between two operational frequencies, or one structure that can turn a function on and off. Previous studies of relevance utilizing reconfiguration to control waves include the work of [11], which provides a good example of how changes in elastic moduli of magnetostrictive materials can be used to affect wave motion. Another tunable magneto-elastic system consists of magnetostrictive particles immersed in an elastic medium, as investigated in [35]. Analogous configuration and stiffness changes are applied in reconfigurable electromagnetic wave filters, as illustrated in [36, 37]. These devices reconfigure their circuit geometry through the activation of electrical switches, allowing a change in the frequencies that can propagate. Though the aforementioned studies utilized reconfiguration to modify wave propagation, the configurations are not stable without a constant input of some kind.

In the subset of magneto-elastic lattices the kagome lattice (KL) is considered as a specific example because it is a very versatile 2D structure regarding shape change [38], which is brought about by reorientation of its components. The 2D KL has already received attention because of its unique mechanical properties such as periodic collapse modes and

"isostatic modes" or "floppy modes" of wave propagation [39, 40, 41] which have low strain energy, or no strain energy in the idealized case. Furthermore, 3D analogs of the kagome pattern have gained interest for shape control in structures [42, 43, 44, 45]. Wave propagation has been studied in KLs for cases involving next-nearest-neighbor interactions [40], lattices including randomly added or removed bonds [46, 47], a 3D kagome analog [48], and even cases with magneto-electro-elastic interactions in solid-state structures [49]. However, the shape change capabilities of the KL have not been coupled with nonlinearities from magnetic interactions to produce engineered configuration changing structures with adaptable wave propagation properties.

1.2.4 Homogenized properties of lattice structures

Oftentimes, it is convenient to investigate periodic metamaterial systems as equivalent continua through homogenization. To show the properties of magneto-elastic lattices on a larger scale their equivalent continuum properties are calculated. The process of homogenization has been investigated for discrete periodic structures by, for example [50, 51, 52, 53]. The approach by [52, 53] is focused mainly on atomistic and molecular crystals. The approach found in [51] provides a generalized method that was extended in [50] to be applied to arbitrarily complex elastic structures. Work that appears very similar at first to the homogenization of magneto-elastic lattices has been published, [15], in which finite magneto-elastic structures show that their Poisson's ratio can be tuned with the application of a non-uniform external magnetic field and through changes in constituent dimensions. The magnetic dipole moments in the 2D structures discussed therein are oriented in the plane of the system and the changes in Poisson's ratio are a result of the re-orientation of the system's rigid entities, as described in [54], under the constant application of the external magnetic field. In contrast to the work in [15], the structures discussed herein contain magnetic dipole moments perpendicular to the lattice plane, and the constant application of a magnetic field is not required.

1.3 Topologically protected boundary modes

Topologically protected boundary modes (TPBM) are a recent development in physics which opens novel approaches in mechanical systems. Starting from the work of Haldane [55], who predicted the possibility of electronic edge states, topological edge modes in quantum systems have been the subject of extensive research due to their immense potential. Their existence has since been demonstrated experimentally [56] and they are called "chiral edge modes." Chiral edge modes are based on breaking time reversal symmetry to mimic the quantum hall effect and are analogous to "chiral" fermions. The bulk bands are characterized by a topological invariant called the Chern number. Recently, Kane and Mele [57, 58] discovered topological modes in systems with intrinsic spin orbit (ISO) coupling, which exhibit the quantum spin Hall effect. These modes are termed "helical edge modes." This system does not require breaking of time reversal symmetry, is characterized by the $Z2$ topological invariant, and has also been demonstrated experimentally [59]. Smith and coworkers [60, 61] studied the effect of next nearest neighbor interactions on a number of lattices and demonstrated competition between the helical and chiral edge states when both ISO coupling and time reversal symmetry breaking occur. These quantum mechanical systems have been extended to other areas of physics as well. For example, Haldane and Raghu [62] demonstrated boundary modes in electromagnetic systems following Maxwell's relations, which have subsequently been widely studied in the context of photonic systems [63, 64].

In recent years, numerous acoustic and elastic analogues of quantum mechanical systems have also been developed. Prodan and Prodan [65] demonstrated edge modes in biological structures, where time reversal symmetry is broken by Lorentz forces on ions due to the presence of weak magnetic fields. Zhang et al. [66] developed a systematic way to analyze eigenvalue problems which break time reversal symmetry by gyroscopic forces. Extending this line of work, Bertoldi and coworkers [67] demonstrated chiral edge modes

in a hexagonal lattice with the Coriolis forces obtained from gyroscopes which rotate at the same frequency as the excitation frequency. Another example is the recent work of Kariyado and Hatsugai [68], where Coriolis forces are generated by spinning the whole lattice. All these designs involve components rotating at high frequencies, or excitation of rotating masses. There have also been a few mechanical boundary modes, based on modulating stiffness in time. Examples include the works of Khanikaev and coworkers [69, 70], Yang et al. [71], Deymier and coworkers [72] and Carusotto et al. [73]. We remark here that all the above devices require energy input for operation and are based on active components. This need to provide energy is an obvious drawback for practical applications.

On the other hand, a few works have focused on mechanical analogues of the helical edge states that arise from ISO coupling and they typically require passive components. Süsstrunk and Huber [74] demonstrated these edge states experimentally in a square lattice network of double pendulums, connected by a complex network of springs and levers. Recently, Chan and coworkers [75] numerically demonstrated edge modes in an acoustic system, comprised of stacked hexagonal lattices and tubes interconnecting the layers in a chiral arrangement. Deymier and coworkers [76] demonstrated non-conventional topology of the band structure in $1D$ systems supporting rotational waves. Khanikaev and coworkers [77] numerically demonstrated helical edge modes in perforated thin plates by coupling the symmetric and antisymmetric Lamb wave modes. The edge modes occur at specially connected interfaces between two plates and it is not clear how to extend the framework to incorporate general building blocks. Indeed, there presently exists a paucity of works demonstrating a simple and systematic way to extend these concepts and build new lattices.

Previous topics discuss reconfiguration and magnetization as a means for controlling structure properties. The work in this thesis on TPBMs, though not including magnets or reconfiguration, is expected to benefit from the future inclusion of magnets due to their asymmetric linearized torsional stiffnesses [78], which might be used to break time reversal symmetry or induce effective spin-orbital coupling. Furthermore, systems exhibiting topo-

logically protected edge states can have changes in one-way wave propagation direction due to geometric reconfiguration [79]. Floppy TPBMs [80] are also a promising avenue for organized structural reconfiguration. Hence, the extension of the work on elastic structures herein is expected to produce useful reconfigurable magneto-elastic lattices exhibiting novel wave control possibilities.

1.4 Wave measurement in 2D lattices

With any new theoretical modelling, it is valuable to have direct validation of the theoretical models used. Therefore, experiments measuring the transient propagation of waves through a magneto-elastic lattice in various configurations are valuable for this research. However, methods suitable for measuring the transient propagation of waves are in short supply. Indeed, most of the work on wave propagation in lattices has been conducted theoretically, with few works focusing on experimental validation of the analyzed properties. Among those which do, the great majority study vibration isolation due to band gaps [81, 82], thus analyzing the steady-state behavior of the system. Transient phenomena, which showcase wave directionality, negative refraction index, and topologically protected edge modes are inherently more difficult to experimentally investigate, requiring full-field measurement of in-plane waves, and they possibly represent the most interesting features of structural lattices. Examples [83, 84] of such experimental investigations are performed by employing a 3D scanning laser Doppler vibrometer (3D SLDV), which has limitations in terms of cost, data acquisition time and applicability to lattice structures with slender elements. Therefore, an alternative approach able to overcome such limitations would be beneficial in aiding the validation process of the properties of magneto-elastic , and other structural lattices.

1.5 Motivations

Reconfigurable structures, which remain passively in their operating state once placed there, could prove valuable in applications requiring a operating state to be held for long periods of time and especially in those in which energy is scarce. Furthermore, their passivity could simplify the practical integration into an application. Though it is well understood that geometric changes have a significant effect on wave propagation in lattice structures, no structures have been recorded that allow for reconfiguration between multiple stable configurations that do not require constant input to maintain stability. Even the versatile kagome lattice has not been applied to produce configuration changing structures with adaptable wave propagation properties. In order to use reconfigurable lattices the means of reconfiguration must be understood, and certainly up to 3 spatial dimensions to be generally applicable. Though 1D dynamic reconfiguration already has a strong base of literature, the study of 2D systems is still in need of much attention. In order to realize reconfigurable devices as suggested previously, deeper understanding of reconfiguration dynamics in higher dimensions is required. Furthermore, if magneto-elastic structures are to be used as reconfigurable structures, quantification of the effect of lattice reconfigurations on the static properties of the lattice would aid in the application of such lattices. Currently, there is no methodology that can quantify the static properties of magneto-elastic lattices as desired. The methodology of [50] is well suited for periodic elastic lattices, but is not presented for use in systems exhibiting non-nearest neighbor interactions, such as magnetic interactions, and therefore requires extension for application to magneto-elastic lattices.

When in pursuit of novel wave control approaches, the notion of confining mechanical waves to one direction of propagation on a lattice boundary is very powerful. However, there are an insufficient number of works demonstrating a simple and systematic way to extend the concepts predicting topologically protected wave modes to arbitrary mechanical lattices.

Ideally, there would be a method to validate the in-plane wave propagation results predicted for magneto-elastic lattices experimentally. Looking also to the further development of metastructures – magneto-elastic , reconfigurable, or otherwise – waves with in-plane polarizations are commonplace. Yet, the only current method for measuring the transient propagation of an in-plane wave in an entire lattice is a 3D scanning laser Doppler vibrometer. An alternative approach able to overcome limitations of cost, data acquisition time, and applicability to lattices of slender elements would be beneficial in aiding the validation process of the properties of structural lattices, and the application of such lattices in the future.

1.6 Objectives

With the aforementioned motivations in mind, in order to provide new and useful work, the objectives of this research are to:

1. identify and evaluate new structures, which have adaptable wave properties,
2. identify practical methods for adapting wave properties,
3. calculate the effect of wave property adaptation on static mechanical properties,
4. improve the tools available for experimentally investigating wave propagation in lattice structures, and
5. increase the understanding of and practicality of mechanical topological insulators.

1.7 Contributions

To pursue the objectives listed in Section 1.6 the following contributions are made:

1. Introduction of magneto-elastic structures for adaptation of wave properties through geometric reconfiguration. Multiple stable configurations allow adaptation between

different stable states, which have different wave propagation properties. Both periodic configurations and arbitrary finite configurations are possible, allowing a rich set of possibilities.

2. Introduction of dynamic reconfiguration as a means for adapting wave properties of magneto-elastic structures. Controlled dynamic forcing leads to transient dynamics that determine a final structural configuration, as does tailoring the unit cell energy profile. By determining the final configuration, the wave properties of the structure are controlled.

3. Quantification of the effect of magneto-elastic structural reconfiguration on equivalent continuum properties. A methodology is extended to fit magneto-elastic lattices, showing that the equivalent orthotropic mechanical properties of magneto-elastic lattices can change by over an order of magnitude due to reconfiguration alone.

4. Identification of new mechanical topological insulators. A new mechanical lattices are added to a presently short list of lattices which can exhibit one-way wave propagation along their boundaries.

5. Development of a new technique for measuring in-plane waves in lattice structures. High-speed photography and digital image correlation (DIC) are combined with geometry recognizing algorithms to measure the time history of the in-plane displacements of lattice nodes. As the method is new, it is applied to the well studied hexagonal lattice.

1.8 Thesis organization

This thesis is organized as follows. Following this introduction, lattice reconfiguration is discussed in Chapter 2, which also contains the description of the model used for magneto-elastic lattices. Wave propagation analyses, and the effect of reconfiguration on wave propagation are discussed in Chapter 3. Homogenized properties of magneto-elastic structures

and their variation with reconfigurations are discussed in Chapter 4. The development of topologically protected boundary modes in a set of mechanical structures is discussed in Chapter 5. A new methodology for the experimental measurement of in-plane waves in metastructures and an experiment conducted to validate the dynamic numerical simulation code is presented in Chapter 6. Finally, conclusions are stated in Chapter 7.

CHAPTER 2

RECONFIGURABLE MAGNETO-ELASTIC STRUCTURES

2.1 Chapter overview

This chapter introduces magneto-elastic structures as a platform for demonstrating systems with multiple stable configurations. It also investigates dynamic reconfiguration between different stable states as a practical means of imposing a global or local geometric change. Tailoring of the unit cell energy profile during reconfiguration is seen to have a substantial effect on the final reconfigured result, determining whether a few or all cells in a lattice reconfigure due to the same forcing. First, the theoretical background of the magneto-elastic structure modeling is described, which uses a lumped parameter model, and the procedure for determining stable eqilibria is presented. Then unit cell energy calculations and numerical simulations are conducted to investigate dynamic transitions.

2.2 Lattice model

Magneto-elastic lattices are modeled as systems of permanent magnetic particles with translational and rotational degrees of freedom (DOFs). Axial and torsional springs connect the particles to form an elastic structure. The particles have a finite radius r_p, and feature both translational and rotational inertias. All particles are identical in terms of their inertial and magnetic properties. Similarly, all springs connecting the particles are massless and feature the same axial and torsional stiffness. The interactions between particles are governed by: (1) magnetic interactions, (2) elastic interactions through axial and torsional springs, and (3) axial and torsional viscous damping interactions. The energy functionals associated with the interactions above and the governing equations are described in the following subsections.

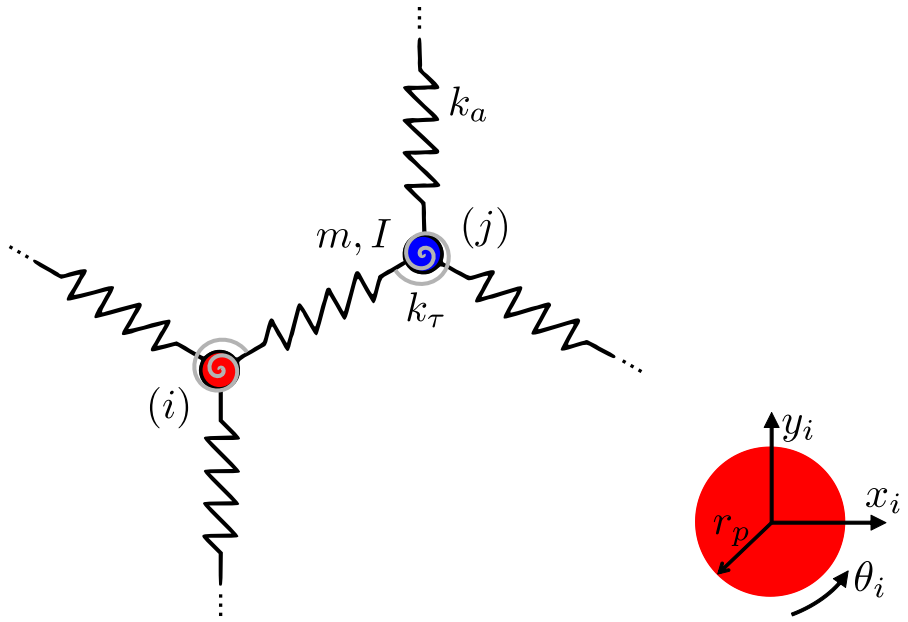

(a) (b)

Figure 2.1: Schematic of mechanical connectivity between two adjacent particles (a), and particle degrees of freedom (b).

2.2.1 Energy functionals

The behavior of the generic i-th particle of a 2D lattice is described by the position of its center of mass $\boldsymbol{r}_i = x_i\boldsymbol{i} + y_i\boldsymbol{j}$, and by a rotation angle θ_i. Accordingly, the vector of the generalized coordinates associated with the i-th particle is given by:

$$\boldsymbol{q}_i = [x_i,\ y_i,\ \theta_i]^T. \tag{2.1}$$

and the kinetic energy of each particle is expressed as:

$$T_i = \frac{1}{2}m(\dot{x}_i^2 + \dot{y}_i^2) + \frac{1}{2}I\dot{\theta}_i^2, \tag{2.2}$$

where $I = \frac{1}{2}mr_p^2$.

Mechanical interactions

The strain energy associated with the elastic interactions is defined in terms of axial and torsional contributions. A phenomenological, simplified model is formulated whereby the axial spring is characterized by a bilinear force-displacement relation, which is chosen as a simplified model for a contact condition between two particles (see Fig. 2.2) . The contact stiffness is described as proportional to the stiffness k_a through a parameter $\alpha > 1$. A contact distance $r_c = 2r_p$ defines the contact conditions. When the contact conditions are satisfied the axial stiffness of the bilinear spring is αk_a. The strain energy associated with the mechanical components connecting particles i and j is therefore given by:

$$\begin{aligned} U_{ij}^{(e)} = \frac{1}{2}k_a(r_{ij} - r_0)^2 + \frac{1}{2}(\alpha - 1)k_a\left(r_c - r_{ij}\right)^2 H(r_c - r_{ij}) \\ + \frac{1}{2}k_\tau(\theta_i - \theta_b)^2 + \frac{1}{2}k_\tau(\theta_j - \theta_b)^2 \end{aligned} \tag{2.3}$$

where k_τ denotes the torsional spring constant, $\boldsymbol{r}_{ij} = \boldsymbol{r}_j - \boldsymbol{r}_i$, r_0 defines the inter-particle distance when the axial springs are undeformed, and H is the Heaviside unit step function.

Magnetic interactions

The magnetic interaction force is described by modeling the permanent magnets as magnetically rigid dipole moments [85, 86]. Furthermore, all magnetic dipole moments are considered perpendicular to the direction of motion. The force between two dipoles is given by [87].

$$\boldsymbol{f}_{ij}^{(m)} = -\frac{\mu_0}{4\pi}\boldsymbol{\nabla}\left(\frac{\boldsymbol{m}_i \cdot \boldsymbol{m}_j}{r_{ij}^3} - 3\frac{(\boldsymbol{m}_i \cdot \boldsymbol{r}_{ij})(\boldsymbol{m}_j \cdot \boldsymbol{r}_{ij})}{r_{ij}^5}\right) \tag{2.4}$$

In the 1D and 2D lattices considered, the motion of the masses is constrained to the direction $\boldsymbol{i}$ and to the lattice plane $\boldsymbol{i}, \boldsymbol{j}$ respectively. This simplifies the expression of the

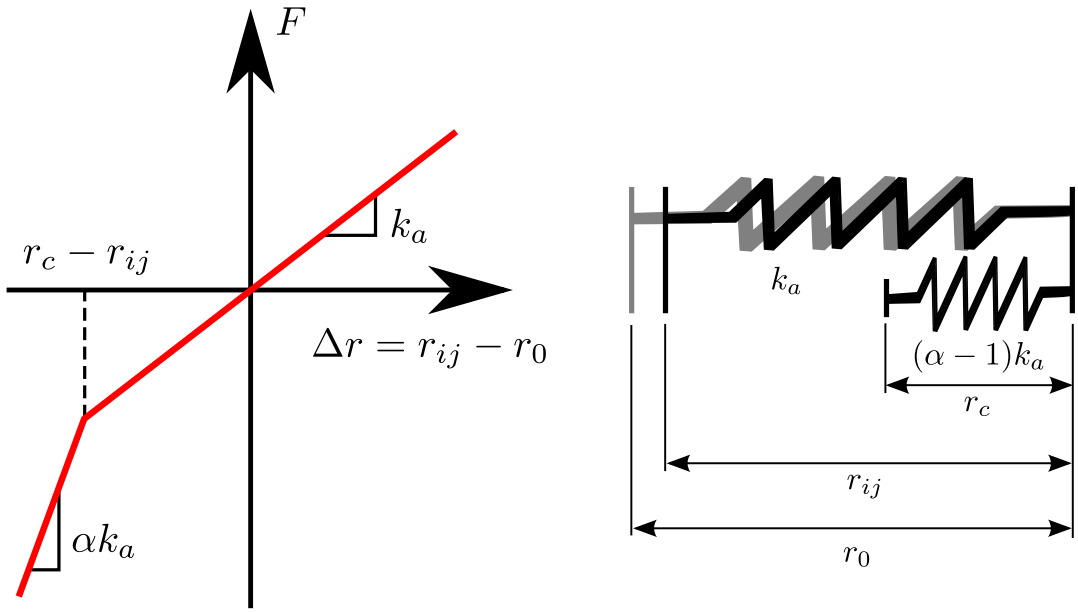

(a) (b)

Figure 2.2: Schematic of bilinear spring interaction model as a simplified description of contact (a), and corresponding force-displacement relation (b).

magnetic interaction force as follows:

$$\boldsymbol{f}_{ij}^{(m)} = \frac{3\mu_0}{4\pi}\frac{m_i m_j}{r_{ij}^4}\boldsymbol{n} = \frac{\psi^{(m)}}{r_{ij}^4}\boldsymbol{n} \tag{2.5}$$

where μ_0 is the permeability of free space, $\boldsymbol{m}_i$ and $\boldsymbol{m}_j$ are the dipole moments of particles i and j, $\boldsymbol{n} = \boldsymbol{r}_{ij}/r_{ij}$ is a unit vector and $\psi^{(m)} = m_i m_j 3\mu_0/(4\pi)$ contains all the magnetic constants. Evaluating the work of the magnetic force (Eq. (2.5)) from a reference state at $r_{ij} \to \infty$ to the current state r_{ij} defines a magnetic potential energy function $U_{ij}^{(m)}$.

$$U_{ij}^{(m)} = -\int_{\infty}^{r_{ij}} \frac{\psi^{(m)}}{r_{ij}^4}\boldsymbol{n} \cdot d\boldsymbol{r}_{ij} = \frac{1}{3}\frac{\psi^{(m)}}{r_{ij}^3} \tag{2.6}$$

The magnetic force described by Eq. (2.5) in theory acts for $r \to \infty$. This implies that the lattice is, in general, characterized by non-nearest neighbor interactions that extend to infinity. However, the magnitude of the magnetic force rapidly decays with inter-particle distance, which for practical purposes allows the introduction of a radius of influence r_∞,

beyond which magnetic interactions are neglected. As many as 3,000 particles may be included in a typical analysis of a magnetized structure. The radius of influence is defined through a tolerable error in energy calculations $\varepsilon_e^{(m)}$, i.e. the error that is introduced by omitting a single magnetic particle at the distance r_∞, given by:

$$\varepsilon_e^{(m)} = \frac{1}{3}\psi^{(m)}\frac{1}{r_\infty^3} \tag{2.7}$$

which can be solved for r_∞ to give:

$$r_\infty = \left(\frac{\psi^{(m)}}{3\varepsilon_e^{(m)}}\right)^{1/3} \tag{2.8}$$

The value of r_∞ defines the range of interactions to be considered, and therefore also dictates the number of particles interacting magnetically.

Dissipative Interactions

Dissipation is introduced in the model in the form of viscous forces acting in conjunction with the spring generalized forces. The work of the dissipative generalized forces is expressed as:

$$W_{ij}^{(d)} = -\int \boldsymbol{f}_{ij}^{(d)} \cdot d\boldsymbol{r}_{ij} - \int \phi_i^{(d)} d\theta_i - \int \phi_j^{(d)} d\theta_j \tag{2.9}$$

where:

$$\boldsymbol{f}_{ij}^{(d)} = \begin{cases} c_a \dot{r}_{ij}\boldsymbol{n} & r_{ij} > r_c \\ \beta c_a \dot{r}_{ij}\boldsymbol{n} & r_{ij} \leq r_c \end{cases} \tag{2.10}$$

where c_a is the damping coefficient and $\beta > 1$ defines the increase in damping coefficient during contact between particles. Also, in Eq. (2.9):

$$\phi_i^{(d)} = -c_\tau(\dot{\theta}_i - \dot{\theta}_b). \tag{2.11}$$

where c_τ is the damping coefficient associated with the particles' relative rotation.

2.2.2 Particle equations of motion

The equation of motion for a single particle can be derived by considering the associated Lagrangian $\mathcal{L}_i = T_i - U_i$ and the sum of the work of the external forces W_i. Here, U_i and W_i denote the contributions to the potential energy and work corresponding to the mechanical and magnetic connections with the neighboring particles affected by such interactions. Specifically, U_i can be expressed as:

$$U_i = \sum_{j}^{J} U_{ij}^{e} + \sum_{m}^{M} U_{im}^{m}$$

where the index j identifies the particles that are mechanically connected to particle i, and the contribution to the energy of the magnetic interactions includes the M magnetically connected particles, here denoted by the index m. The coordination number of the lattice is J, which in the considered configurations is equal to 2 for the 1D lattice, and equal to 3 for the 2D hexagonal and re-entrant lattices. Also,

$$W_i = \sum_{j}^{J} W_{ij}^{(d)}$$

Application of Lagrange equations leads to the following equation of motion in terms of the generalized coordinates $\boldsymbol{q}_i \in \mathbb{R}^{3\times1}$ of each particle:

$$\boldsymbol{M}_i\ddot{\boldsymbol{q}}_i + \sum_{j}^{J} [\boldsymbol{C}_j(\boldsymbol{q}_j)\dot{\boldsymbol{q}}_j + \boldsymbol{K}_j(\boldsymbol{q}_j)\boldsymbol{q}_j] = \boldsymbol{f}_i^{(m)}(\boldsymbol{q}_i, ..., \boldsymbol{q}_m, ..., \boldsymbol{q}_M) \tag{2.12}$$

where $\boldsymbol{M}_i, \boldsymbol{C}_j(\boldsymbol{q}_j), \boldsymbol{K}_j(\boldsymbol{q}_j) \in \mathbb{R}^{3\times3}$ are mass, damping and equivalent stiffness matrices that describe inertial, dissipative and mechanical interactions of the particles with its neighbors, while, $\boldsymbol{f}_i^{(m)} \in \mathbb{R}^{3\times1}$ is the generalized force vector describing the magnetic interactions with the M magnetically connected particles.

2.2.3 Lattice description and unit cell energy

The considered lattices are characterized by periodic distributions of masses along the $\boldsymbol{i}$ direction in the case of the 1D lattice, and over the plane $\boldsymbol{i}, \boldsymbol{j}$ for the 2D lattice. Their positions are described through a set of lattice vectors. For the 1D lattice, the position of the $n-th$ particle can be expressed as $\boldsymbol{r}_{i,n} = x_{i,n}\boldsymbol{i} = (x_i + nd)\boldsymbol{i}$, where x_i defines the particle position within a reference unit cell, while d denotes the spatial periodicity of the lattice. In the 2D lattice case, the generic particle is identified by two indexes and its position is expressed as $\boldsymbol{r}_{i,nm} = \boldsymbol{r}_i + n\boldsymbol{d}_1 + m\boldsymbol{d}_2$, where $\boldsymbol{d}_1, \boldsymbol{d}_2$ are the lattice vectors, while $\boldsymbol{r}_i$ is the position of the considered particle in the reference cell (Fig. 2.3).

The description of the behavior of the lattice relies on the identification of a unit cell, and on the study of its equation of motion including all interactions with other cells within the lattice. In this work, a unit cell is defined as the smallest structure which can be repeated to describe the mass, stiffness, damping, and magnetic characteristics of the assembly. The distribution of magnetizations within the lattice offers the opportunity to produce a large number of periodic configurations, or magnetic domains, in addition to the geometric connectivity of the particles. In the present study, we limit our attention to the case where nearest neighbor magnets are all in attraction. The considered unit cells for 1D and 2D lattices are shown in Fig. 2.4. Unit cells describing kagome lattices are also considered, but the study of kagome lattices and additional detail describing the modelling of them are discussed in the next chapter. Accordingly, both 1D and 2D lattices feature unit cells that include two particles with opposite magnetizations.

The total energy of the unit cell is given by the sum of the potential energy U and kinetic energy T and the work of the external forces W:

$$\mathcal{E} = \sum_{e=1}^{E} U_e + T_e + W_e \tag{2.13}$$

where $e = 1, ..., E$ identifies the particles belonging to a unit cell. The magnetic interac-

tions can be considered as external forces or, since they are magnetically rigid, they can be included in U_e. As the lattice is periodic, this energy functional is equal for all unit cells and its expression does not need to keep track of a specific unit cell identifier, which simplifies notation. The generalized coordinates for the unit cell are therefore:

$$\boldsymbol{q} = [\boldsymbol{q}_e, ..., \boldsymbol{q}_E]^T. \tag{2.14}$$

As the lattice is periodic, this energy functional is equal for all units and its expression does not need to keep track of a specific unit cell identifier, which simplifies notation.

The formulation of the unit cell governing equations describing the behavior of the cell and its interactions with connected units is a straightforward extension of the equation of motion of a single particle (Eq. (2.12)). The resulting set of governing equations describing the behavior of the cell and its interactions with connected units is expressed as follows:

$$\boldsymbol{M}\ddot{\boldsymbol{q}} + \sum_{n=-1}^{1}\sum_{m=-1}^{1}[\boldsymbol{C}_{n,m}(\boldsymbol{q}_{n,m})\dot{\boldsymbol{q}}_{n,m} + \boldsymbol{K}_{n,m}(\boldsymbol{q}_{n,m})\boldsymbol{q}_{n,m}] = \boldsymbol{f}^{(m)}(\boldsymbol{q}_{-N,-M}, ..., \boldsymbol{q}_{N,M}) \tag{2.15}$$

where $\boldsymbol{M}, \boldsymbol{C}_{n,m}, \boldsymbol{K}_{n,m} \in \mathbb{R}^{3E\times 3E}$ are unit cell level matrices, and $\boldsymbol{q}, \boldsymbol{f}^{(m)} \in \mathbb{R}^{3E\times 1}$ are unit cell level vectors of generalized coordinates and forces. The considered equations can be extended to the entire lattice through standard assembly procedures so that they may be used for dynamic simulations predicting the dynamic behavior of finite lattices.

2.3 Identification of stable equilibria

The energy functional in Eq. (2.13), restricted to the time constant terms, is employed for the identification of the periodic equilibrium configurations and for the analysis of their stability which is discussed in this section. The stable periodic equilibrium configurations are identified through an optimization search algorithm that seeks for local energy minima [88]. The considered energy functional includes contributions of all elastic and mag-

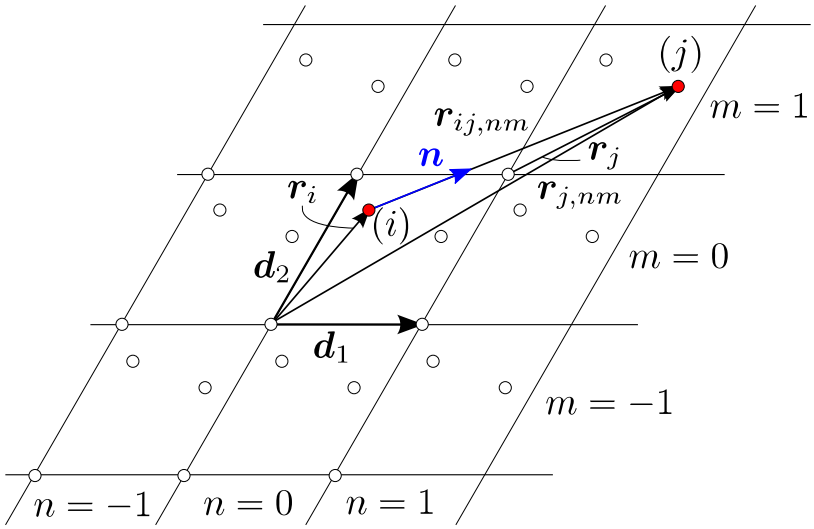

Figure 2.3: Schematic of 2D periodic lattice and index notation for the identification of a particle and of a unit cell.

netic interactions, which extend beyond the nearest neighbors. The cell interacting with a reference unit are denoted with the index $n = -N, ..., N$ in 1D lattices, and the index pair $n = -N, ..., N; m = -M, ..., M$ in 2D lattices. The case of $N, M = 1$ describe the limiting case where only nearest neighbor cell interactions are included in the energy balance and contribute to the equilibrium configuration.

The considered lattices include bilinear springs and magnetic interactions, which lead to the potential for multiple periodic patterns to exist. Periodicity is associated with the arrangement of masses and the chosen magnetization patterns. Moreover, the elongation of the springs allows for distinct inter-mass distances at equilibrium. As a result, unit cells with different number of masses can define different periodic configurations.

As indicated before, we limit this study to the case were adjacent magnets are in attraction. Even with this assumption, several periodic unit cells can be identified depending on the spatial distribution of the stable inter-mass distances within the lattice. For example, Fig. 2.5(a-c) illustrates examples of periodic equilibrium configurations for 1D lattices corresponding to unit cells consisting of two particles, where the unit cells are defined by alternating magnetizations and by equilibrium configurations corresponding to all springs at

rest in their most elongated configurations (a), by masses in contact alternating with masses separated by spring at rest (b), and by all masses in contact (c). Unit cells defined by 3 and 4 particles as a result of different spring elongations are shown in Fig. 2.5(d-g), while two-dimensional configurations are illustrated in Fig. 2.6. In order to reduce the number of possible combinations, and operate with a manageable set configurations, an additional assumption is made that only configurations consisting of 2 particles are considered. This is enforced by imposing a 2-particle periodicity as a constraint to the optimization problem defining the equilibrium conditions. This is practically implemented by imposing periodic conditions prior to the minimization of the static energy functional, i.e. by letting:

$$\boldsymbol{q}_{n,m} = \boldsymbol{q}$$

with $n = -N, ..., N; m = -M, ..., M$, and where for simplicity $\boldsymbol{q} = \boldsymbol{q}_{0,0}$ denotes the degrees of freedom of the reference unit. This implies that the unknowns of the nonlinear algebraic problem seeking for a minimum of the energy functional are: the unit cell degrees of freedom $\boldsymbol{q}$ including the coordinates x, y of the particles within a unit cell and their rotation θ, and the lattice vectors $\boldsymbol{d}_1, \boldsymbol{d}_2$ in the case of 2D lattices. The resulting nonlinear system of equations is expressed as:

$$\min_{\boldsymbol{u}} \quad \mathcal{E}(\boldsymbol{u}) \tag{2.16}$$

where $\boldsymbol{u} = [\boldsymbol{q}, \boldsymbol{d}_1, \boldsymbol{d}_2]$. The problem in Eq. (2.16) is solved through an unconstrained Quasi-Newton optimization scheme as described in [89].

Requiring a 2-particle periodicity is clearly an arbitrary choice which excludes many of the possible solutions and implicitly relies on the assumption of an infinite lattice. Some of the excluded equilibrium solutions may be associated with lower energy levels, and therefore may be energetically favorable with respect to the ones found herein. However, this choice limits the amount of investigations and provides a framework for the study of

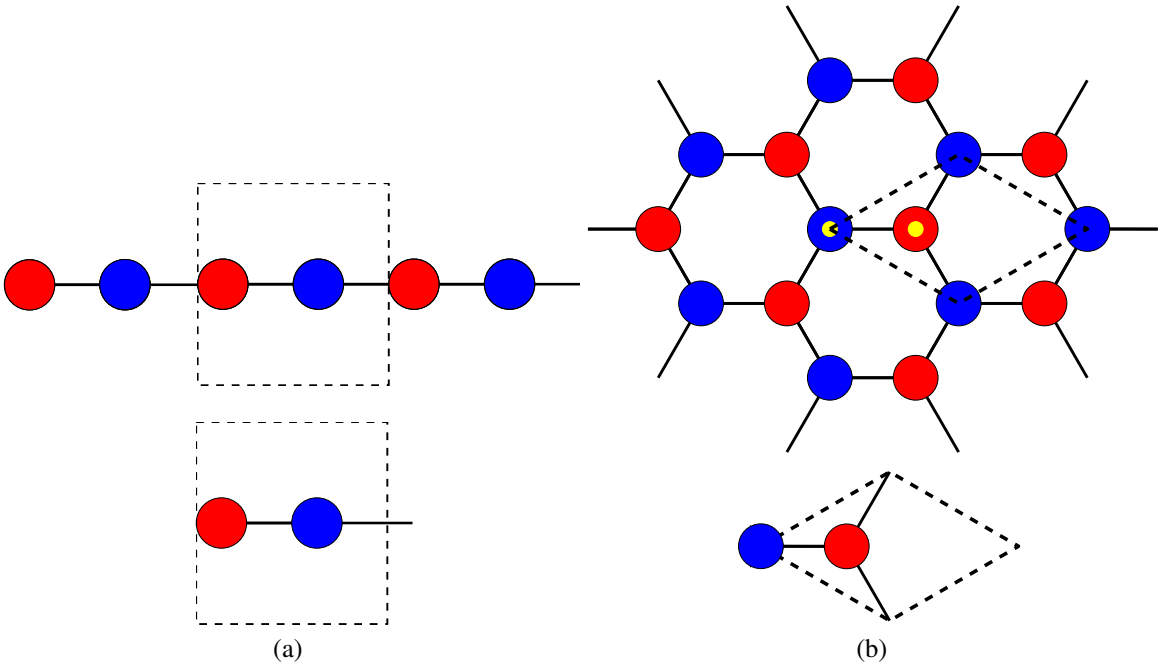

Figure 2.4: 1D and 2D lattices resulting from magnets in attraction as considered in this study. Red and blue circles denote magnets with dipole moments perpendicular to the lattice plane pointing towards and away from the reader respectively. Black lines denote elastic connections between magnets.

the lattice properties in the selected subset of possible periodic equilibrium configurations.

2.4 Dynamic reconfiguration of magneto-elastic hexagonal lattices

To add to the literature regarding 2D dynamic reconfiguration an initial study of dynamic structural changes in 2D structures is conducted using a magneto-elastic hexagonal honeycomb lattice as an example. The energy profile associated with a unit cell of the lattice is employed as a means to predict the reconfiguration characteristics. Though additional research is required to investigate the spatial extent of the reconfiguration in 2D systems, unit cell analyses and numerical experiments presented herein are expected to provide insights for future modeling and design of 2D dynamically reconfigurable structures.

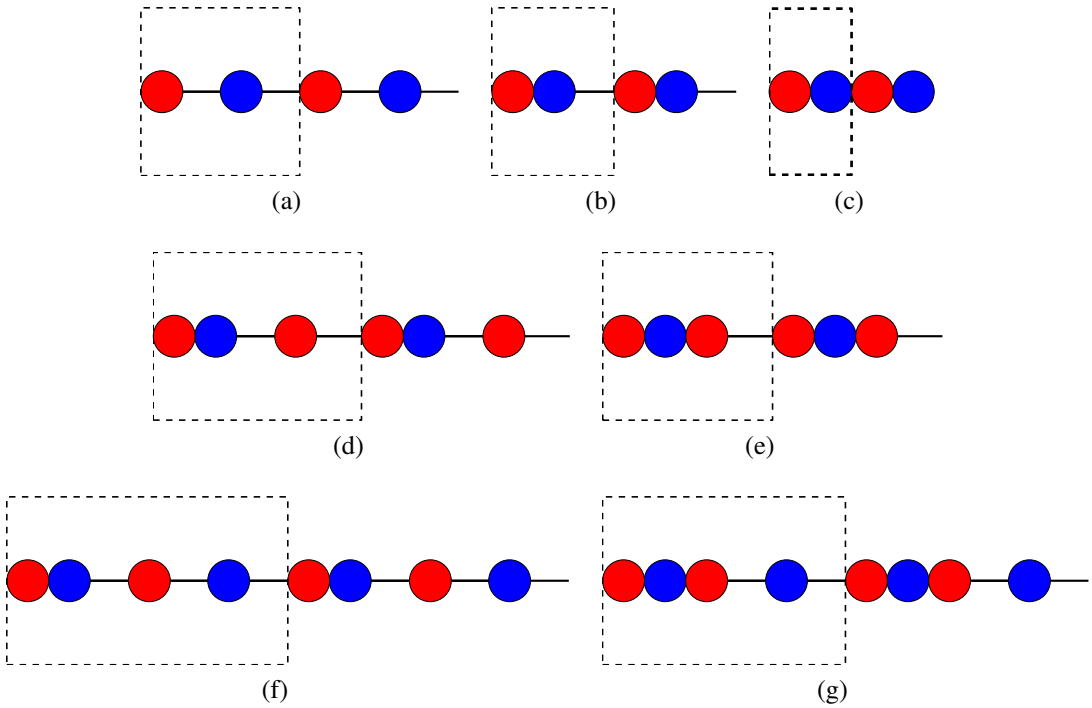

Figure 2.5: Examples of periodic equilibrium configurations for 1D lattices consisting of 2 particle unit cells (a-c), 3 particle unit cells (d,e), and 4 particle unit cells (f,g). Red and blue circles denote magnets with dipole moments perpendicular to the lattice plane pointing towards and away from the reader respectively. Black lines denote elastic connections between magnets.

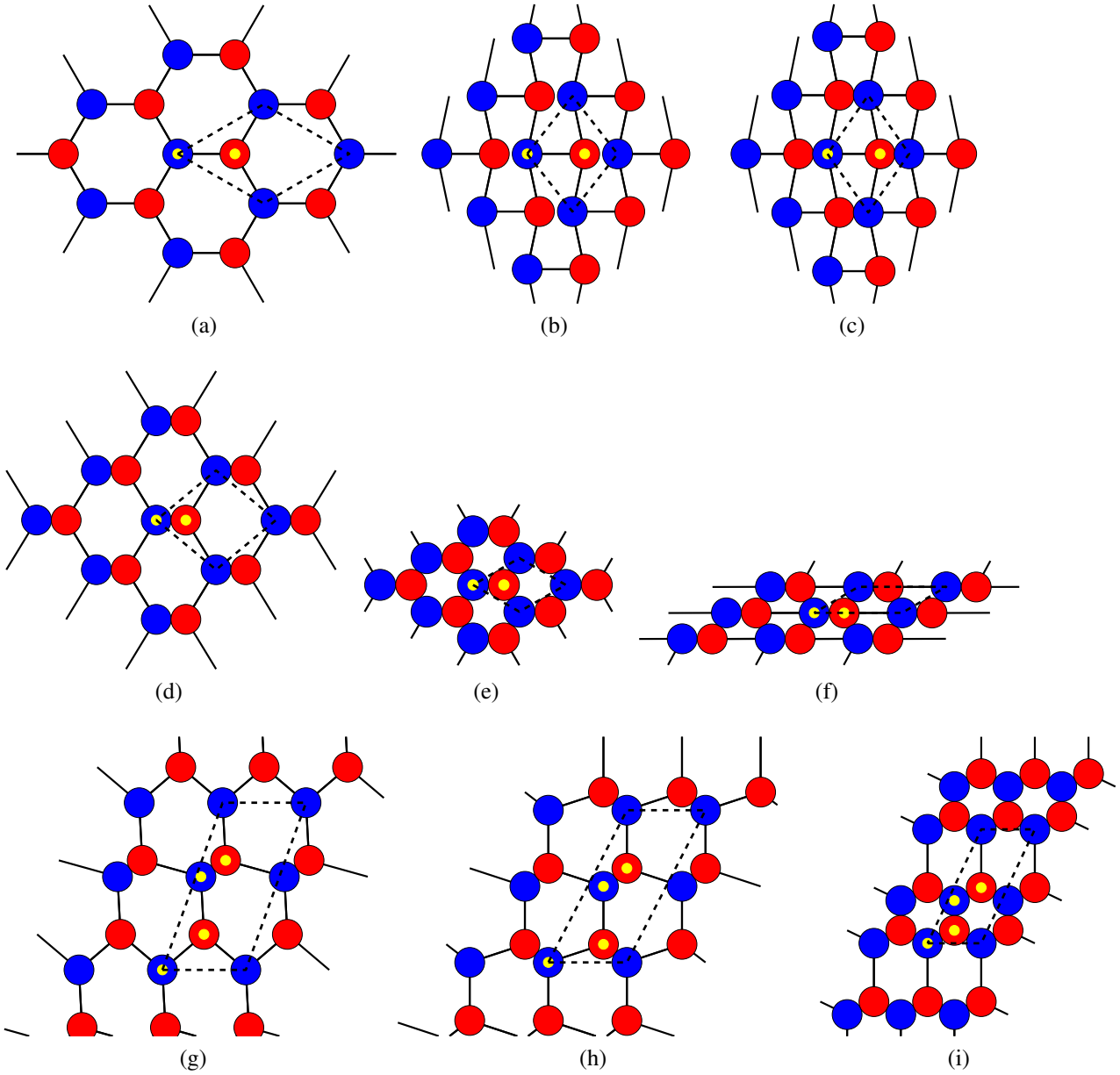

Figure 2.6: Examples of periodic equilibrium configurations for 2D lattices consisting of 2 particle unit cells (a-f), and 4 particle unit cells (g-i). Red and blue circles denote magnets with dipole moments perpendicular to the lattice plane pointing towards and away from the reader respectively. Black lines denote elastic connections between magnets.

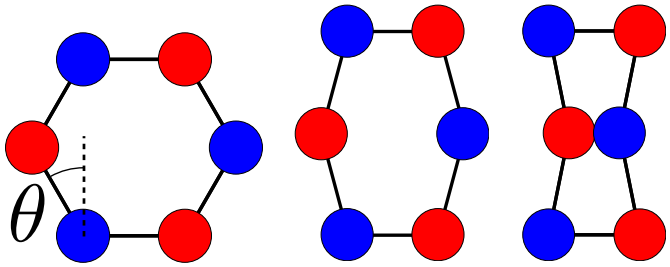

(a) $\theta = 30°$ (b) $\theta = 15°$ (c) $\theta \approx -14°$

Figure 2.7: Hexagonal (a) and re-entrant (c) lattices as two stable periodic equilibrium configurations. The angle θ describes the transition from one to the other and defines intermediate configurations (b). Red and blue circles denote magnets polarized into and out of the page respectively. Black lines represent elastic connections.

2.4.1 Analysis of equilibrium configurations

Because of magnetic interactions, the lattice can take different stable configurations, which correspond to different values of the angle θ (Fig. 2.7). When magnetized in the pattern shown (blue and red circles denote opposite magnetic polarizations), the hexagonal lattice (Fig. 2.7(a)) may reconfigure in stable configurations corresponding to various values of the internal angle θ, and may evolve into the re-entrant lattices of Fig. 2.7(c).

As discussed in Section 2.3, the minimization problem at the unit cell level is formulated by considering as unknowns the generalized coordinates $\boldsymbol{q}$ of the particle inside the unit cell, i.e. the red particle in Fig. 2.8, and the lattice vectors $\boldsymbol{d}_1, \boldsymbol{d}_2$. To look at the energy associated with a transition between configurations geometrical constraints are imposed on the energy minimization problem (Eq. (2.16)) as follows: (1) the center red particle can only move along the horizontal center line of the unit cell which is defined by the vector resultant $\boldsymbol{d}_1 + \boldsymbol{d}_2$, and (2) the two lattice vectors are of equal magnitude, i.e. $d_1 = d_2$. These two constraints enforce the unit cell symmetry about its horizontal center line. This problem is solved by imposing the angle θ and then looking for the geometrical configuration associated with a stable equilibrium configuration. The result for each input θ is a local energy minimum and associated configuration, giving insight to the energy required to transition from one value of θ to another.

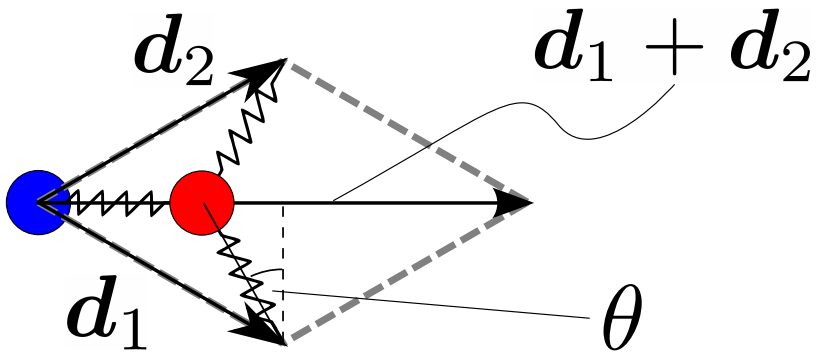

Figure 2.8: Unit cell of the hexagonal lattice, lattice vectors and main geometric parameters.

Equilibrium configurations are found for assigned values of $\theta \in [-20°,\ +35°]$ and for different magnetization levels. The loci of the corresponding equilibrium configurations are shown in Fig. 2.9 for three levels of magnetizations. The plots present the change in unit cell potential energy ΔU at equilibrium relative to the regular hexagonal unmagnetized case as a function of the imposed value of θ. In the plot of Fig. 2.9 and in the remainder of the chapter, unit cell energy and magnetization parameter are respectively normalized as follows:

$$\Delta\bar{\mathcal{E}} = \frac{2\Delta U}{k_a r_0^2} \tag{2.17}$$

where the denominator corresponds to the total energy stored by the axial spring when it is fully compressed and there is no contact (i.e. $r_{ij} = 0$, and $\gamma = 0$), with r_0 denoting the undeformed length of the axial springs, and

$$\bar{\psi}^{(m)} = \frac{\psi^{(m)}}{k_a r_0^5} = \frac{f^{(m)}(r_{ij} = r_0)}{k_a r_0} \tag{2.18}$$

which defines the ratio of the magnetic force at $r_{ij} = r_0$ to the force required to fully compress the axial spring in the absence of contact, i.e. $k_a r_0$. Hence, $\bar{\psi}^{(m)}$ provides a comparison of the strength of the magnetic interactions relative the axial spring restoring force.

The magnetization levels considered in Fig. 2.9 are $\bar{\psi}^{(m)}$ =0, 0.02, and 0.05, while the

lattice is defined by the following parameters: $\gamma = \alpha - 1 = 39$, $r_c = 0.5$, $c_a/m = 0.4$ s^{-1}, $c_\tau/(mr_0^2) = 0$ s^{-1}, $\beta = 50$, $I/(mr_0^2) = 1/32$, $\omega_0 = \sqrt{k_a/m} = 1$ rad/s, $\omega_r = \sqrt{k_\tau/I} = \sqrt{1/2}$ rad/s. In Fig. 2.9, the curve corresponding to the unmagnetized case, ($\bar{\psi}^{(m)} = 0$) is continuous, with a noticeable slope discontinuity near $\theta = -15^\circ$ which corresponds to the initial contact between particles. Of note is the fact that the initial, regular hexagonal case $\theta = 30^\circ$ is the most energetically favorable configuration, which therefore indicates that a lattice perturbed from this initial configuration is likely to return to it without undergoing any reconfiguration. The energetic advantage of this initial configuration is clearly shown in the detailed plot of Fig. 2.9(b). Thus, configurations with re-entrant angle and contact would require additional energy to be provided for the system to evolve into them from an initial configuration of $\theta = 30^\circ$. The magnetized cases, in contrast, have a significantly different behavior as indicated by the discontinuous red and blue dashed lines in Fig. 2.9. The range for $\theta > 0$ looks essentially identical to the case for $\bar{\psi}^{(m)} = 0$, while re-entrant magnetized configurations are characterized by equilibrium geometries associated with significantly lower energy levels. This indicates that the magnetized lattices, if provided enough energy in the form of external perturbations, can indeed evolve and transition to a different stable equilibrium geometries with $\theta < 0$. The amounts of energy that enable such a transition cannot be directly estimated from the curves in Fig. 2.9 as the dynamic terms associated with inertias and dissipation need to be accounted for in order to evaluate the transition through a saddle point in the energy profile, which is here not shown and not directly estimated. As expected, the energetic levels of the re-entrant equilibrium configurations for the magnetized lattices are lower for increasing magnetization levels. This is consistent with the fact that the magnets are all arranged in attraction due to their alternate polarization distributions. One may consider cases where repulsive configurations are present, which would lead to different geometries and periodic lay-outs defined by the distributions of magnetic polarizations.

The next section illustrates how these investigations can aid the interpretation of the

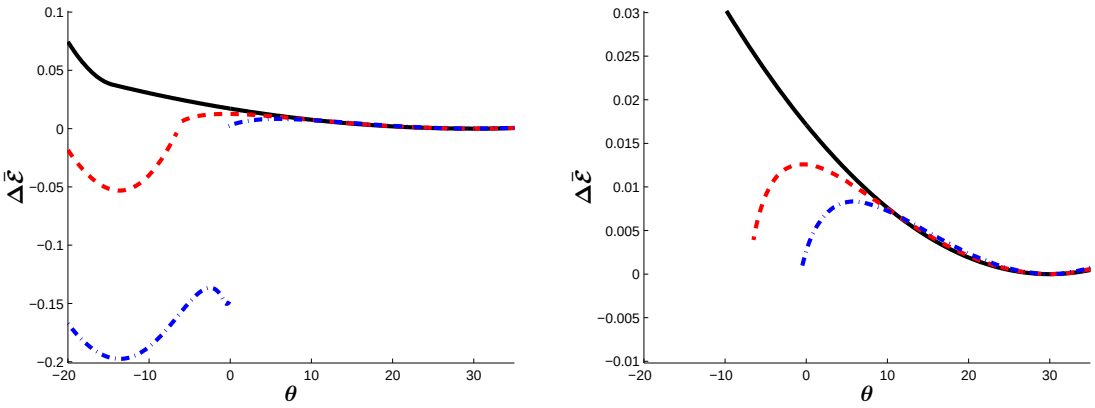

(a) (b)

Figure 2.9: Equilibrium loci for the unit cell as a function of internal angle θ: $\bar{\psi}^{(m)} = 0$ (black $-$), $\bar{\psi}^{(m)} = 0.02$ (red $--$), and $\bar{\psi}^{(m)} = 0.05$ (blue $\cdot-$) (a), and 10x zoom for detailed view in the $\theta > 0$ range (b).

dynamic behavior of the considered class of lattices and potentially inform their design for multi-stability.

2.4.2 Numerical simulation of dynamic reconfiguration

To gather information about how lattice magnetization can affect the transformation of the 2D magneto-elastic lattice, numerical simulations are performed by integrating the equations of motion (Eq. (2.12)) in time. A finite lattice is considered with a number of cells chosen so that boundary effects can have minimum influence on the transient behavior of the central portion of the lattice. The initial configuration for the finite lattice is determined by imposing an initial angle $\theta = 30^\circ$ and determining the lattice vectors as a function of the applied magnetization levels, and assuming that all springs are at rest when the lattice is in the initial regular hexagonal configuration in the absence of magnetization. Solution of the equilibrium configurations through minimization of the energy function for the entire finite lattice defines the initial geometry. Such geometry may be slightly different in the presence of magnetization, due to the magnetic attraction that leads to small changes in the lattice vectors. Such changes, which are accounted for in the simulations, are however

too small to be noticeable from the graphical representation of the lattice, given the small magnetization levels considered and the forces that are only a few percent of the magnitude of the spring restoring forces. Once the initial equilibrium configuration is identified, boundary conditions are applied to enforce the stability of the lattice and to avoid rigid body motions. The choice of the equilibrium conditions are based on the choice of enforcing symmetry along the mid horizontal line under an equally symmetric load distribution, which in this case is a horizontal point force applied at the middle point of the left vertical boundary. The selected boundary conditions are pins constraining horizontal and vertical displacements along the vertical right boundary, and roller-type constraints along the top and bottom edges to constrain only the vertical displacements. Along all boundaries, rotations remain unconstrained. A schematic of the finite lattice with point of loading and boundary conditions is shown in Fig. 2.10.

All simulations are conducted by applying a force varying in time as a rectangular pulse at the location shown. Pulse duration and amplitude are chosen empirically to be sufficient to induce transition in the magnetized cases. The energy associated with the pulse is sufficient to compensate for the energy needed to transition from the initial stable configuration to another in the case of multi-stable layouts. Such energy must overcome all kinetic contributions and dissipation terms. All simulations consider a pulse width of 0.08π s and an amplitude $F_0 = 6k_a r_0$. The response of the three different structures is presented in Fig. 2.11. In the unmagnetized case, this pulse perturbs the lattice, but it does not cause its re-configuration, since upon removal of the force the lattice returns to its initial configuration, which is the most energetically favorable. As a result no transition occurs in the lattice, as shown in Fig. 2.11(c). For $\bar{\psi}^{(m)} = 0.02$ the system becomes multistable. The re-entrant configuration has a lower energy. Therefore, energy will be released into the lattice during the transformation, with the potential to aid in further reconfiguration. Given the 2D geometry of the lattice, the energy associated with the input force decays with the distance from the point of application due to geometrical spreading. This leads to

the re-configuration to be only observed over a limited region of the lattice, within which the cells receive sufficient energy to transition to the lower energy states corresponding to the re-entrant configuration (Fig. 2.11(d-f)). For a higher magnetization, i.e. $\bar{\psi}^{(m)} = 0.05$, the entire lattice reconfigures by the end of the simulations due to the lower energetic level observed at the unit cell level for this magnetization (Fig. 2.11(g-h). The study of the dynamic behavior of the lattice can also be observed in terms of the energy within a unit cell. Specifically, the cell highlighted by the red dashed line in Fig. 2.10 is observed at various instants of time during the simulations. These variations are overlaid on the equilibrium curves for the corresponding magnetization levels in Fig. 2.12. The resulting plots show the time evolution of the trajectory of the unit cell configuration and its energy as black dots, while the minimum energy curve is the solid red curve. Each black dot shows the energy at an instant, evenly spaced in time, and the red curves are the curves of Fig. 2.9 without the shift. The plots illustrate how such configurations evolve dynamically from the initial configuration to a final. All the simulations begin at the local minimum at $\theta = 30^\circ$, which is the hexagonal lattice configuration. Then the cell energy increases due to the applied force, and through the dynamics of the structure it oscillates about and progresses to its final local energy minimum. Such oscillations are shown in the inset of the figures for better clarity. Note that all energy trajectory points are above the red curve for all intermediate dynamic configurations, which illustrates how the curve correctly provides a lower bound for the energy content of the unit cell under consideration. In the absence of magnetization (Fig. 2.12(a)) the unit cell undergoes significant distortions due to the forcing as illustrated by the large variations of the internal angle θ, which temporarily reaches negative values, but it returns to oscillate around the initial configuration. This is because there is no other equilibrium position for it to stop at. The magnetized cases shown in Fig. 2.12(b,c) clearly illustrate the transition of the unit cell energy from the initial configuration at $\theta = 30^\circ$ to the re-entrant state near $\theta = -15^\circ$, which is the point of arrival upon removal of the force and the free motion of the lattice.

Returning to Fig. 2.11, it is worth noting that the pattern of reconfiguration is not uniform and appears to be characterized by a pattern which is common to both magnetization cases. The results seem to suggest the existence of a triangular transition front that does not propagate uniformly within the lattice. The pattern of propagation of this front may be affected by the underlying isotropy, or lack thereof, of the lattice, which in turn is determined by the unit cell geometry. This aspect certainly deserves further investigation as it may have significant implications for the design of multi-stable lattices with desirable transition front propagation characteristics. Of note is also the fact that the energy profile of the $\bar{\psi}^{(m)} = 0.05$ structure allows faster reconfiguration for the same forcing, which is observed in comparing Figs. 2.11(d-e) and Figs. 2.11(g-h). This is likely because more energy is available to be converted into kinetic energy. The final configuration of the $\bar{\psi}^{(m)} = 0.05$ case (Fig. 2.11(i)) is much different than the initial configuration and the final configuration of the $\bar{\psi}^{(m)} = 0.02$ case. It has a much higher density and is composed entirely of anisotropic cells. Three sub-regions of re-entrant cells are separated by two bands of cells oriented approximately perpendicularly to the others. These bands can be denoted as "transition bands". The transition bands are the result of the dynamic reconfiguration of the lattice, and different forcing has been observed to produce different numbers and positions of transition bands. The local geometric variations seen in the transition bands affect the propagation of waves and are expected to aid in wave steering and energy absorption.

Finally, in simulating the collapse of magneto-elastic lattices such as those presented here it is observed that the damping characteristics of the system can greatly affect the dynamics of the system, which can ultimately change the final configuration. For the aforementioned study, the damping was all kept constant for simplicity, but if structures such as these are to be dynamically reconfigured in a predictable way, the effect of damping must be taken into account and properly characterized. For example, increasing the contact damping parameter β helps prevent overshooting when particles come into contact near their secondary stable position. To illustrate this, β is reduced to 5 from 50 for the

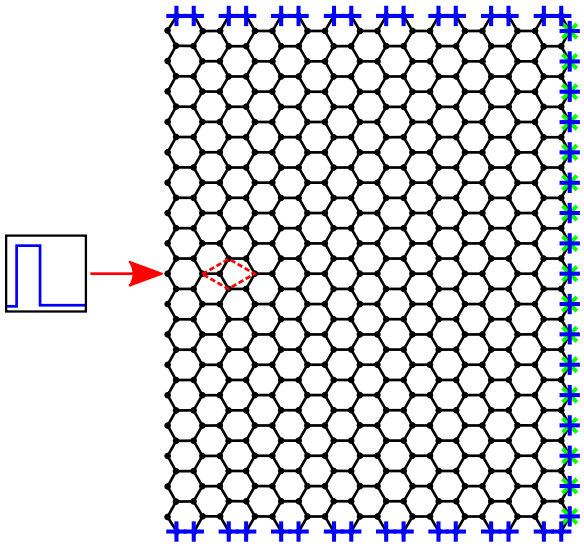

Figure 2.10: Numerical simulation setup for finite lattice. Black lines represent axial springs and black dots represent magnetized masses. Green "x"s denote constraint for horizontal displacements, and blue "+"s denote constraint of vertical motion. The dashed red lines show a unit cell for which energy is plotted in Fig. 2.12.

$\bar{\psi}^{(m)} = 0.02$ case and the simulation is repeated. Shown in Fig. 2.13(a-c), it is clear that the change in β does not allow some of the particle pairs to remain in contact. Instead, they bounce out of the local energy minimum and the final configuration has only one collapsed cell. It has also been observed that increasing the torsional damping c_τ allows the system to better distribute the applied force transversely, similar to increasing the viscosity of a fluid. For reference, in Fig. 2.11 there is no torsional damping. To contrast this, simulations of the $\bar{\psi}^{(m)} = 0.02$ case with $c_\tau/(mr_0^2) = 0.05$ s^{-1} and 0.50 s^{-1} were run. The first case (Fig. 2.13(a-c)) shows deformation spread more evenly across the left side of the structure than in Fig. 2.11(d-f) and results in only 3 collapsed cells in response to the forcing instead of 6. The second case (Fig. 2.13(g-i)) shows that with sufficient torsional damping the applied force will be distributed and dissipated so well that no reconfiguration can occur under the applied load. These 3 examples are merely an example of how reconfiguration can be further tailored through damping, and this aspect requires further investigation.

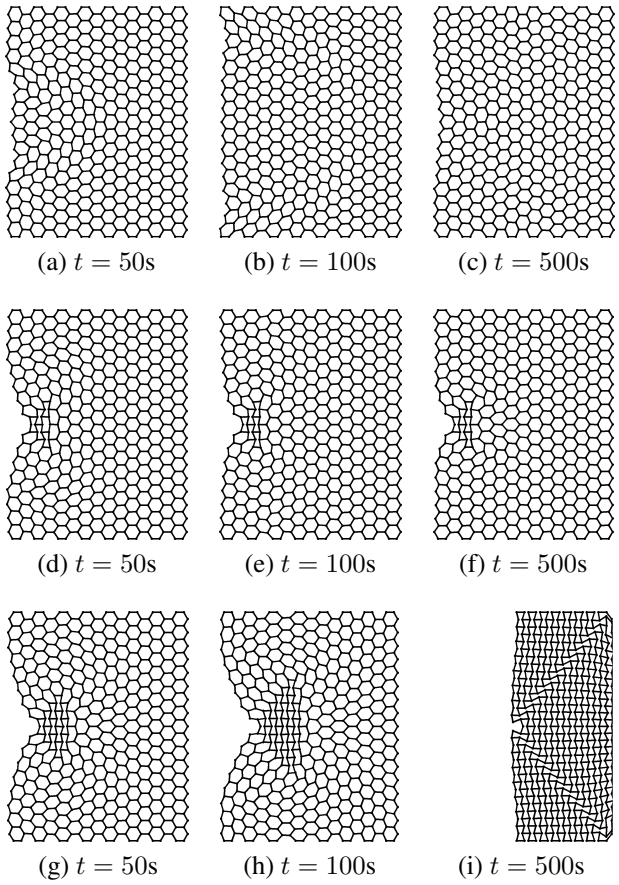

(a) $t = 50$s (b) $t = 100$s (c) $t = 500$s

(d) $t = 50$s (e) $t = 100$s (f) $t = 500$s

(g) $t = 50$s (h) $t = 100$s (i) $t = 500$s

Figure 2.11: Snapshots of deformed configuration of the lattices observed during dynamic simulations: $\bar{\psi}^{(m)} = 0$ (a-c), $\bar{\psi}^{(m)} = 0.02$ (d-f), and $\bar{\psi}^{(m)} = 0.05$ (g-i)

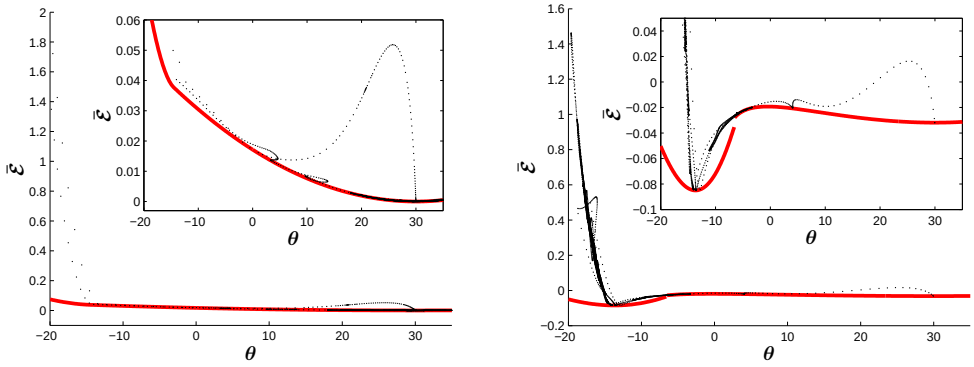

(a) $\bar{\psi}^{(m)} = 0$ (b) $\bar{\psi}^{(m)} = 0.02$

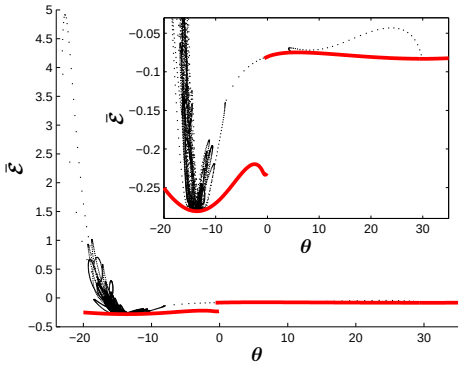

(c) $\bar{\psi}^{(m)} = 0.05$

Figure 2.12: Normalized potential energy $\bar{\mathcal{E}}$ of the unit cell highlighted in Fig. 2.10 for the three simulations discussed shown as the cell exhibits different values of θ during deformation.

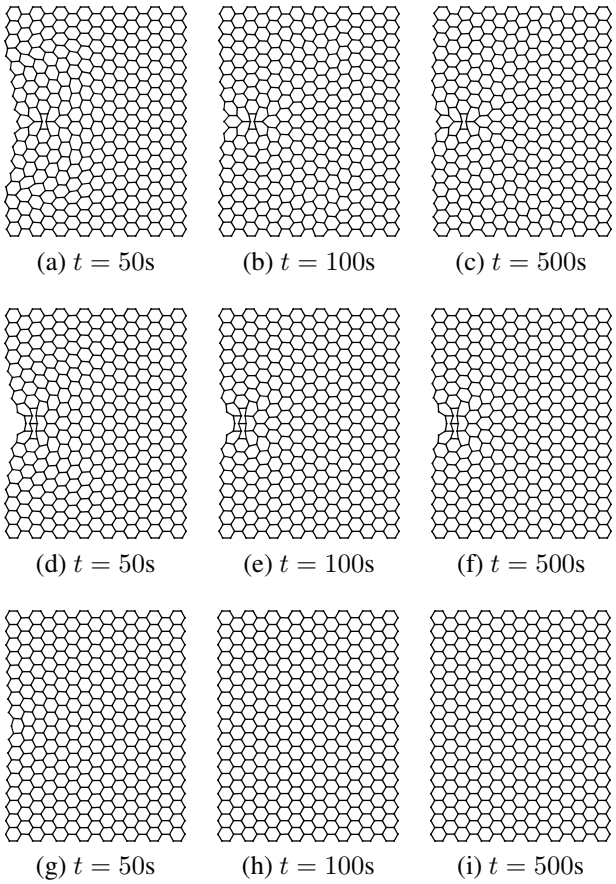

(a) $t = 50$s (b) $t = 100$s (c) $t = 500$s

(d) $t = 50$s (e) $t = 100$s (f) $t = 500$s

(g) $t = 50$s (h) $t = 100$s (i) $t = 500$s

Figure 2.13: Snapshots of the lattices with $\bar{\psi}^{(m)} = 0.02$ observed during dynamic simulations with different damping parameters: $\beta = 5$ (a-c), $c_\tau/(mr_0^2) = 0.05$ s^{-1} (d-f), and $c_\tau/(mr_0^2) = 0.50$ s^{-1} (g-i). Other lattice parameters are left unchanged.

CHAPTER 3

WAVE PROPAGATION IN MAGNETO-ELASTIC STRUCTURES

3.1 Chapter overview

The purpose of this chapter is to present the wave propagation properties of periodic magneto-elastic lattices and quantify how reconfigurations affect these properties. Bloch analysis is performed to provide analytical quantification of dispersion relations for both 1D and 2D lattices, and numerical simulations are used to verify and illustrate the findings of Bloch analysis. Drastic wave propagation changes are induced through the configuration changes, including the opening of bandgaps and wave beaming. First, the procedure for applying Bloch analysis to magneto-elastic structures is over-viewed. Then analytical and numerical results for 1D structures are presented. This is followed by results for 2D structures, which include hexagonal, re-entrant, and kagome lattices.

3.2 Application of Bloch analysis

Wave propagation within the considered lattices is investigated through the application of Bloch Theorem [90, 91], which requires the linearization of the governing equations. This is based on the assumption that propagating waves induce small perturbations of the lattice configuration about one of the stable equilibrium configurations. A first order Taylor series expansion is employed to linearize the magnetic force expressed in Eq. (2.5), which gives:

$$\bar{\boldsymbol{f}}_{ij}^{(m)} = \boldsymbol{f}_{eq_{ij}}^{(m)} - 4\frac{\psi^{(m)}}{r_{eq_{ij}}^{5}}(r_{ij} - r_{eq_{ij}})\boldsymbol{n} \tag{3.1}$$

where $r_{eq_{ij}}$ denotes the equilibrium distance of particles i, j obtained through the approach described in the previous section. Also, $\bar{\boldsymbol{f}}_{ij}^{(m)}$ is the linearized magnetic force, while $\boldsymbol{f}_{eq_{ij}}^{(m)}$

is the interaction force at equilibrium, i.e. when it is equilibrated by the mechanical interaction corresponding to spring elongations $r_{0_{ij}} - r_{eq_{ij}}$. The spring force is linear for small changes of the inter-particle distance, so further linearization is not necessary. In addition, a small angle approximation linearizes the contribution to the mechanical interactions of the torsional springs, as defined by the angle θ_b, which is simplified to:

$$\theta_b = \frac{y'_j - y'_i}{r_{eq_{ij}}} \tag{3.2}$$

where y'_j and y'_i are the displacements of particles i and j in the direction perpendicular to $\boldsymbol{r}_{eq_{ij}}$.

Upon linearization, the equations of motion for a unit cell (Eq. (2.15)) can be expressed as:

$$\boldsymbol{M}\ddot{\boldsymbol{q}}_{n,m} + \sum_{n=-N}^{N}\sum_{m=-M}^{M}\left(\boldsymbol{K}^{(e)}_{n,m} + \boldsymbol{K}^{(m)}_{n,m}\right)\boldsymbol{q}_{n,m} = \boldsymbol{0} \tag{3.3}$$

where, for the purpose of wave propagation analysis, dissipation is neglected, and the absence of external forcing is assumed. In Eq. (3.3), $\boldsymbol{K}^{(e)}_{n,m}, \boldsymbol{K}^{(m)}_{n,m}$ respectively describe the linearized elastic and magnetic interactions between the considered unit cell, here identified by the subscripts $n = 0, m = 0$, and the $(2N+1)(2M+1) - 1$ connected neighbors. In the case of nearest neighbor interactions, $N = M = 1$, while the magnetic forces cause long range interactions defined by the selected r_∞ value.

Plane wave propagation is investigated through the application of Bloch theorem, which seeks for solutions of the kind [3]:

$$\boldsymbol{q}_{n,m} = \boldsymbol{q}_0 e^{i(\omega t + \boldsymbol{\kappa}\cdot(n\boldsymbol{d}_1 + m\boldsymbol{d}_2))} \tag{3.4}$$

Its substitution in Eq. (3.3) gives:

$$\left[-\omega^2\boldsymbol{M} + \sum_{n,m}\left(\boldsymbol{K}_{n,m}e^{i\boldsymbol{\kappa}\cdot(n\boldsymbol{d}_1 + m\boldsymbol{d}_2)}\right)\right]\boldsymbol{q}_0 = \boldsymbol{0} \tag{3.5}$$

where $\boldsymbol{K}_{n,m} = \boldsymbol{K}^{(e)}_{n,m} + \boldsymbol{K}^{(m)}_{n,m}$. Letting:

$$\boldsymbol{K}(\boldsymbol{\kappa}) = \sum_{n,m} \left[\boldsymbol{K}_{n,m} e^{i\boldsymbol{\kappa}\cdot(n\boldsymbol{d}_1 + m\boldsymbol{d}_2)} \right]$$

leads to the following eigenvalue problem:

$$\left[\boldsymbol{K}(\boldsymbol{\kappa}) - \omega^2 \boldsymbol{M} \right] \boldsymbol{q}_0 = \boldsymbol{0} \tag{3.6}$$

which is solved in terms of ω for assigned values of the wave vector $\boldsymbol{\kappa}$. Equation (3.6) is a linear eigenvalue problem whose solution provides the dispersion relations $\omega(\boldsymbol{\kappa})$ characterizing wave motion associated with small perturbations around one of the equilibrium configurations. The dispersion properties characterize the propagation of waves within the lattice and provide the wave velocities and their directional dependence, which gives insight in the speed and direction of wave motion. Specifically, the group velocity, given by:

$$\boldsymbol{c}_g = \nabla \omega(\boldsymbol{\kappa}) \tag{3.7}$$

can be evaluated through numerical differentiation of the dispersion relations obtained from the solution of Eq. (3.6), and directly [92]. Both methods yield the same result.

3.3 Wave propagation in 1D magneto-elastic strcutures

One dimensional structures are discussed first to demonstrate wave propagation properties adaptation as a function of configuration and magnetization. A simple example of a 1D stable reconfigurable lattice is presented to illustrate these concepts.

3.3.1 Geometric adaptation

Geometric adaptation refers to the transition of the lattice between two of its stable configurations. In this case, we investigate the 2 particle unit cell lattice of Fig. 2.4(a), and its

transition between the configurations shown in Fig. 2.5(a) and 2.5(b), and also between the configurations shown in Fig. 2.5(a) and 2.5(c). Such a transition corresponds to the case where the magnetic attractive forces overcome the restoring force provided by the connecting springs and drive the particles in contact. The result is a shorter chain whose periodicity is dependent upon the contact radius of the particles in addition to the initial inter-particle distance r_0.

It is instructive to first evaluate the energy associated with the unit cell and its variation in terms of strength of magnetization and inter-particle distance. For illustration purposes, a first study considers the case where the spring force is purely linear, thus neglecting the contact model and assuming $\alpha = 1$ as the contact parameter in Eq. (2.3) (see also Fig. 2.2(b)). Furthermore, the inter-particle distance r between all neighboring particles is kept equal to r so that the period is $d = 2(x_2 - x_1) = 2r$. Although this constraint may require effort to apply to a manufactured structure, since the structure shown in 2.5(b) would typically be an intermediate configuration for a quasi-static transition between the configurations in Fig. 2.5(a) and 2.5(c), it is a convenient way to illustrate the change in energy as a function of the inter-particle distance r and make considerations that apply also to other reconfigurations.

The variation of the total static energy of interaction (Eq. (2.13)) as a function of inter-particle distance is shown in Fig. 3.1(a). The energy is normalized as follows:

$$\bar{\mathcal{E}} = \frac{2\mathcal{E}}{k_a r_0^2}$$

where normalization is conducted with respect to the total energy stored by the axial spring when it is fully compressed and there is no contact (i.e. $r = 0$, and $\alpha = 1$). The different curves represent different magnetization values $\psi^{(m)}$, where the following normalization is conducted:

$$\bar{\psi}^{(m)} = \frac{\psi^{(m)}}{k_a r_0^5} = \frac{f^{(m)}(r = r_0)}{k_a r_0}$$

The normalized value $\bar{\psi}^{(m)}$ can be interpreted as the ratio of the magnetic force at $r = r_0$ to the force required to fully compress the axial spring in the absence of contact, i.e. $k_a r_0$. Hence, this normalized quantity provides a reference of the strength of the magnetic interaction with respect to the spring restoring force, with a magnitude of $\bar{\psi}^{(m)} = 1$ corresponding to the magnets providing enough force at $r = r_0$ to theoretically reduce the inter-particle distance from the spring undeformed distance r_0 to zero. In the following results shown $\bar{\psi}^{(m)} > 0$ will be used to denote a structure with repelling nearest neighbors and $\bar{\psi}^{(m)} < 0$ will be used to denote a structure with attracting nearest neighbors. In general, $\bar{\psi}^{(m)}$ will simply denote magnitude for a structure, since attraction and repulsion of magnets depends on the specific magnet pair in a lattice. Therefore when the terms "high" and "low" are used to refer to $\bar{\psi}^{(m)}$ it is the magnitude that is being discussed.

The energy curve for $\bar{\psi}^{(m)} = 0$ in Fig. 3.1 (thin $\cdot-$ curve) is parabolic, since it is governed only by linear elastic springs. Therefore a single minimum defines the stable equilibrium inter-particle distance $r_{eq} = r_0$. For magnets in repulsion (thin $\cdot\cdot$ curve), the lattice is still characterized by a single equilibrium for $r_{eq} > r_0$, while nearest neighbor magnets in attraction (thick $-$ and thick $--$ curves) lead to a stable equilibrium $r_{eq} < r_0$, as well as to a second equilibrium point that corresponds to the local maximum of the energy curve and thus is unstable. As attraction increases (thick $\cdot\cdot$ curve), stable and unstable equilibria points get closer, and eventually no longer exist as a result of the magnetic force overpowering the spring restoring force. Of interest is the transition between the condition of existence of the equilibria and their absence, which is characterized by a finite range of inter-particle distance values which defines almost neutral equilibrium conditions. In this range, the lattice configuration may be altered with essentially no energy input. Also in Fig. 3.1(a), the loci of the energy minima and maxima are highlighted respectively by a solid black line, and by the dashed red line, which respectively display the change in

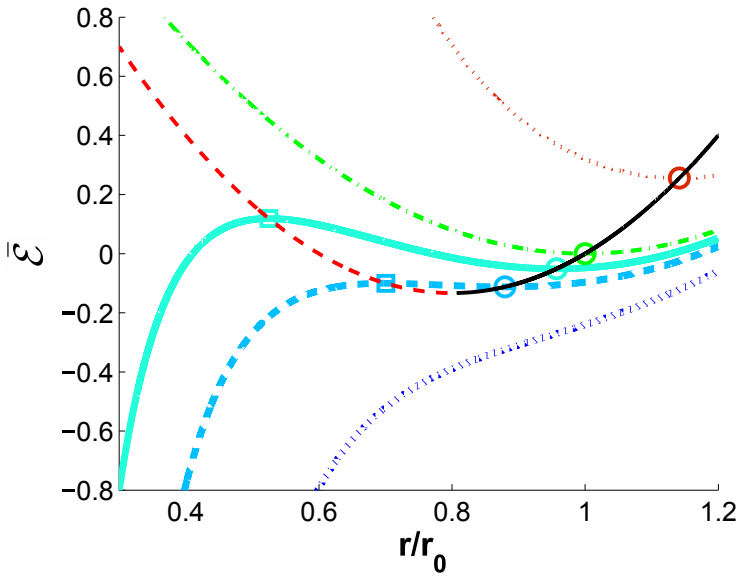

(a)

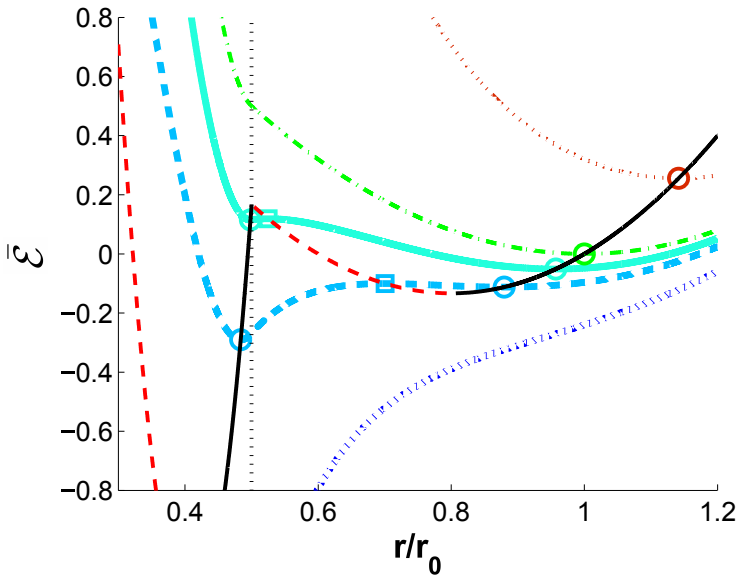

(b)

Figure 3.1: Interaction energy within a 2-particle unit cell lattice as a function of inter-particle distance for different levels of magnetization ($\bar{\psi}^{(m)} = 0.20$ thin $\cdot\cdot$, $\bar{\psi}^{(m)} = 0$ thin $\cdot-$, $\bar{\psi}^{(m)} = -0.04$ thick $-$, $\bar{\psi}^{(m)} = -0.08$ thick $--$, $\bar{\psi}^{(m)} = -0.20$ thick $\cdot\cdot$): no-contact ($\alpha = 1$) (a), and contact ($\alpha = 50$) (b) Circles and squares denote stable and unstable equilibria respectively, thin solid black line is the locus of stable equilibria, thin dashed red line is the locus of unstable equilibria.

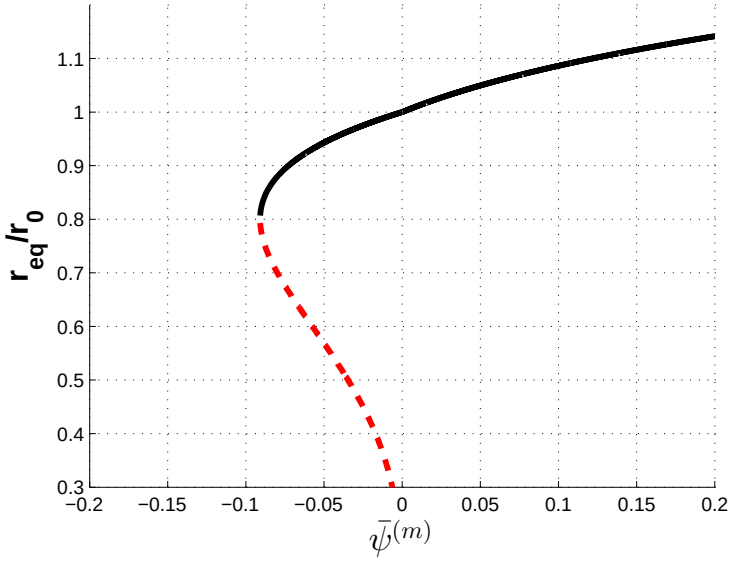

(a)

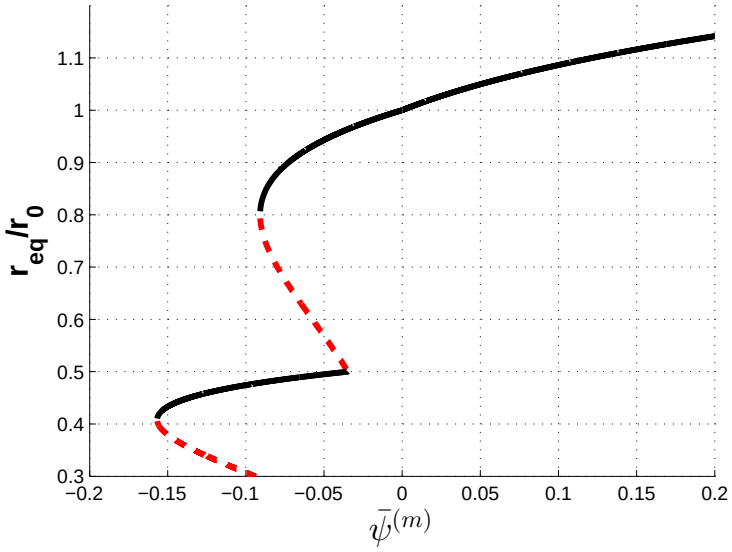

(b)

Figure 3.2: The normalized equilibrium distance r_{eq}/r_0 versus magnetization $\bar{\psi}^{(m)}$: no-contact ($\alpha = 1$) (a), and contact ($\alpha = 50$) (b) (Black solid lines denote stable equilibria while red dashed lines denote unstable equilibria).

location of stable and unstable equilibria as a function of magnetization. The energy plots become more interesting when particle contact is added by considering $\alpha \neq 1$ in the spring constitutive behavior. For example, the energy plot of Fig. 3.1(b) is obtained for $r_c = 0.5r_0$ (particle radius $r_p = 0.25r_0$) and a contact stiffness defined by $\alpha = 50$. The plots show that with magnets in attraction (thick $-$ and thick $--$ curves), there are values of magnetization that lead to a second stable equilibrium. Depending on the choice of parameters, the two energy wells may be characterized by either lower or higher energy, which in principle allows one configuration to be designed as more energetically favorable than the other.

Plotting the equilibrium distances r_{eq} (normalized to the inter-particle distance in the absence of magnetization r_0) against magnetization for the case of no particle contact (Fig. 3.2(a)) further reveals that there is a maximum attractive magnetization at which the particles can stably stay apart. Stable and unstable equilibria are shown by the solid and dashed lines respectively. When the stable equilibrium vanishes the magnets overpower the spring at all distances and there is no equilibrium. Furthermore, for repulsive magnetization there is no unstable equilibrium. Adding contact (Fig. 3.2(b)) introduces a second stable equilibrium condition that is also characterized by an attractive magnetization value beyond which there are no more equilibria. The value of the critical magnetization is dependent on the contact distance r_c and the contact relative stiffness α, which are again chosen as $r_c = 0.5r_0$ and $\alpha = 50$.

3.3.2 Dispersion diagrams and numerical results

Bloch wave analysis is conducted for the lattices in the two equilibrium configurations. The linearized equations of motion are considered according to the procedure described in Section 3.2, reduced to the case of 1D wave motion. The considered lattices are defined by the following set of parameters: $r_c = 0.5r_0$, $\alpha = 8$, $\omega_0^2 = k_a/m = 1$ rad/s, and $\bar{\psi}^{(m)} = -0.035$. The latter value leads to a non-local interaction which extends to 46 particles, which according to Eq. (2.7) corresponds to a residual error of $\varepsilon_e^{(m)} = 10^{-5}$.

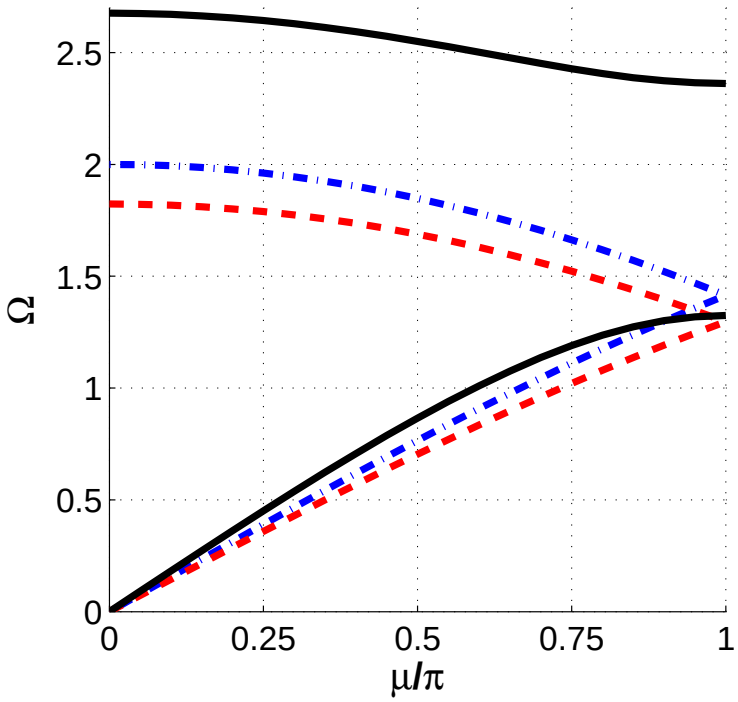

Figure 3.3: Band structure for the 1D lattices of Fig. 2.5(a) unmagnetized (blue $\cdot-$), Fig. 2.5(a) magnetized with $\bar{\psi}^{(m)} = -0.035$ (red $--$), and Fig. 2.5(b) magnetized with $\bar{\psi}^{(m)} = -0.035$ (black $-$). The plots illustrate the shift of dispersion branches due to the magnetization and the opening of a bandgap due to lattice reconfiguration from Fig. 2.5(a) to Fig. 2.5(b).

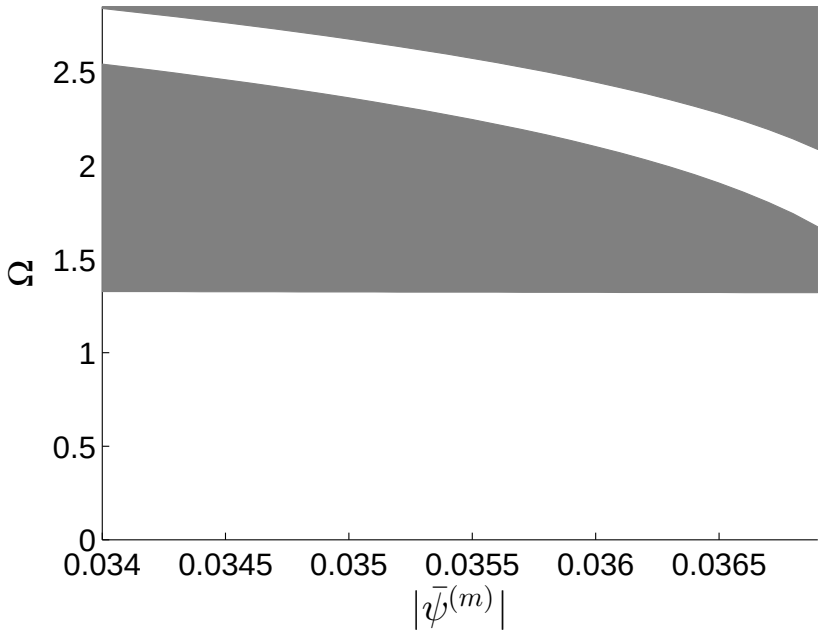

Figure 3.4: The bandgap of the lattice pictured in Fig. 2.5(b) changes with lattice magnetization. The gray denotes frequencies at which waves will not propagate for a given relative magnetization ($\bar{\psi}^{(m)}$).

The corresponding stable equilibrium configurations are those shown in Fig. 2.5(a) and (b), for which band diagrams are calculated and presented in Fig. 3.3. In both cases, the diagrams are plotted in terms of a non-dimensional frequency $\Omega = \omega/\omega_0$, versus the propagation constant $\mu = \kappa d$, where d is the period of the lattice identified as detailed in Section 2.3. The propagation constant allows the dispersion relations for both configurations to be plotted on the same axes even though the period d of each configuration is different. The results for the lattice in Fig. 2.5(a) (blue $\cdot-$ and red $--$ curves) show the absence of a bandgap, as optical and acoustic modes join at the edge of the Brioullin zone. This is to be expected, as the lattice effectively reduces to mono-atomic of period equal to twice the inter-particle distance defined by the stable equilibrium distance r_{eq} associated with the considered level of magnetization ($\bar{\psi}^{(m)} = -0.035$). The effect of the magnetization is to effectively reduce the mechanical stiffness of the connecting spring of a quantity corresponding to the linearized expression of the magnetic force (Eq. (3.1)). This results in

a downshift of the dispersion branches, which is consistent with the reduction in equivalent stiffness. However, no stiffness modulation is produced and therefore no bandgaps are generated. In contrast, the transition of the lattice to the configuration shown in Fig. 2.5(b) (black $-$ curve), obtained also with a magnetization of $\bar{\psi}^{(m)} = -0.035$, effectively introduces a periodic stiffness modulation that is defined by the two considered stiffness values k_a and αk_a. This modulation leaves the acoustic mode almost unaffected, but significantly shifts the optical mode towards higher frequencies, thus generating a large bandgap around $\Omega \approx 1.8$. This illustrates how the transition of the lattice between these two stable configurations reduces its ability to transmit mechanical waves in the considered frequency range. Such a transition is the result of perturbation of the lattice that provides the energy required for the system to evolve from one stable configuration to another.

The bandgap for the configuration of Fig. 2.5(b) can also be tuned through changes in the applied magnetization, which influences the equivalent stiffness of interaction. A map of bandgaps as a function of magnetization is shown in Fig. 3.4. The range of magnetizations chosen coincides with one where the considered configuration can exist as a stable equilibrium. If the magnetization magnitude is too low, the structure will open fully, while if it is too high, the contact interaction will be overcome by the magnets. This sensitivity of this structure to changes in magnetization allows its bandgap to be controlled through relatively small changes in magnetization ($< 10\%$). Less sensitive structures can also be designed, for example, by increasing the contact stiffness α. Here, the optical and acoustical branches are respectively associated with the contacting and non-contacting magnets. The optical branch appears more sensitive to magnetization changes than the acoustic branch because the magnetic interactions play a larger role in softening the shorter distance interaction between the contacting magnets than the longer distance interaction between the non-contacting magnets.

3.3.3 Numerical simulation of wave motion

The change in wave propagation properties, and the occurrence of a bandgap is evaluated by performing numerical simulations through integration of the fully nonlinear equations of motion of a finite lattice with a sufficiently large number of cells. Specifically, the lattice is chosen to include 32 particles, which is found as a good compromise between computational cost and number of units of the assembly. The number of units must be sufficiently large to allow observing wave propagation without being affected by boundary reflections that complicate the interpretation of the data. The lattices are excited by an imposed displacement of the left end mass. The displacement varies in time according to a 20 cycles tone burst at $\Omega = 1.5$ with an amplitude of $5 \times 10^{-5} r_0$. The amplitude is small enough for nonlinearities not to have a significant effect on wave motion. Furthermore, all magnetic interactions are included given the finite extent of the lattice. Results are presented in Fig. 3.5 as the position of the magnets over time. The time axis $\tau = t/t_0$ is normalized with respect to a characteristic time $t_0 = L/c$ which corresponds to the propagation time through the length of the lattice L at speed c. Such speed is here estimated as the slope of the dispersion diagrams of Fig. 3.3 for $\mu \to 0$, i.e. in the long wavelength limit. This speed does not correspond to the actual speed of wave motion at the considered frequency, but provides a reference value suitable for time normalization. The results of Fig. 3.5 show that the wave propagates along the structure when in the fully open configuration (Fig. 2.5(a)), but not when the structure is reconfigured to the so-called semi-packed configuration of Fig. 2.5(b). This observation verifies the presence of a bandgap at the considered frequency and that the dispersion relation in Fig. 3.3 can be useful for predicting whether or not waves will propagate as long as the linearized behavior holds.

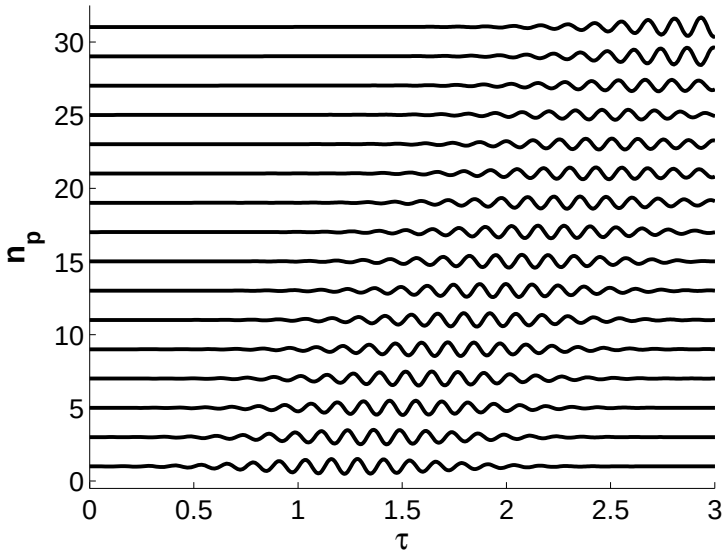

(a) Open Configuration

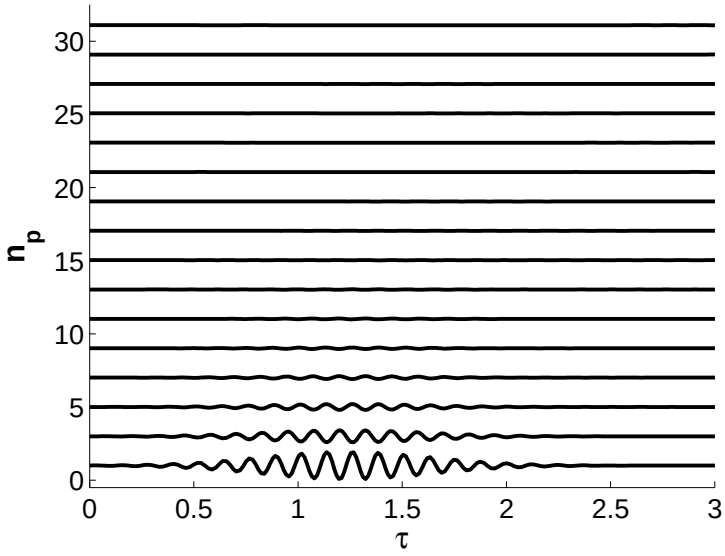

(b) Semi-closed Configuration

Figure 3.5: The existence of the bandgap at $\Omega = 1.5$ is verified through direct numerical simulation. Propagation along the length of the structure is depicted as a position vs. time plot where each line is the motion of one magnet (particle number n_p in the chain). For viewing clarity the displacement of the magnets is amplified and only every other magnet is plotted.

3.4 Wave propagation in 2D magneto-elastic structures

3.4.1 Hexagonal and re-entrant lattices

The investigations are extended to the case of 2D magneto-elastic lattices, which provide the opportunity to investigate the effects of magnetization and configurational changes on the in-plane wave properties, which include dispersion and directionality. Multi-stability leads to changes in the equivalent elastic moduli, mass distributions and anisotropy. Hexagonal lattices provide a good framework for this study, as their elastic properties and the associated wave propagation characteristics have been extensively studied [93, 30, 7].

Geometric Adaptation

The configurations of Fig. 2.6(a)-(c) are examples of lattices under investigation, and the transition between them can be geometrically described through the change of a single angle. As shown in [30], hexagonal lattices of the kind shown in Fig. 2.6(a), and re-entrant ones as in Fig. 2.6(b) differ in their mechanical properties, the former being isotropic, the latter being strongly anisotropic and featuring negative Poisson's ratios. As a result, their wave properties largely differ. Hence, the possibility of transitioning between an hexagonal and a re-entrant configuration provides the opportunity to induce both changes in mechanical properties as well as in the way waves are transmitted by the lattice.

Equilibrium configurations for the 2D lattices considered herein are investigated using the procedure described in Section 2.3. As previously indicated, the investigations are limited to cases where the unit cell includes two masses. Hence, potential equilibrium configurations are those shown in Fig. 2.6(a) and (c), which are obtained by considering lattices defined by the following parameters: $r_c = 0.5r_0$, $\alpha = 50$, $\bar{\psi}^{(m)} = -0.035$, and $\varepsilon_e^{(m)} = 10^{-6}$.

Dispersion diagrams and wave velocities

The dispersion relations for the two lattices of Fig. 2.6(a) and (c) are evaluated through the application of Bloch analysis based on the linearized equations of motion about the two equilibria. For these studies the parameters used are: $r_c = 0.5r_0 = 2r_p$, $\alpha = 40$, $\omega_0^2 = k_a/m = 1$ rad^2/s^2, $I = \frac{1}{2}mr_p^2 = \frac{1}{32}mr_0^2$ (cylindrical magnets), $\omega_r^2 = k_t/I = \frac{1}{2}$ rad^2/s^2, and values of $\bar{\psi}^{(m)} \in [0,\ -0.1]$. The contact distance and contact stiffness allow for stability of the re-entrant lattice pictured in Fig. 2.6(c) through a wide range of $\bar{\psi}^{(m)}$ values. The analysis includes non-local interactions with interaction distances determined by Eq. (2.8) with $\varepsilon_e^{(m)} = 10^{-6}$ and an assigned magnetization. Magnetization specifically induces a change in the effective stiffness of the lattice which produces shifts in the dispersion branches. In addition, magnetization and contact lead to multi-stability which is associated to a configurational change that has a dramatic effect on mechanical properties and dispersion.

Figure 3.6 and 3.7 show the band diagrams for the hexagonal and re-entrant lattices of Fig. 2.6(a) and (c) respectively, and illustrate the effect of varying magnetization. As is customary, the band diagrams are generated by identifying the first Brioullin zone and by varying the wave vector along the boundary of the irreducible zones which are shown respectively in Fig. 3.6(a) and Fig. 3.7(a). In the case of the hexagonal lattice (Fig. 3.6), the considered levels of magnetization have the effect of slightly altering the configuration of the lattice, and most importantly of changing the equivalent stiffness. Such stiffness change causes a noticeable change in slope of the dispersion curves in the long wavelength limit ($\kappa \to 0$). The branch corresponding to the longitudinal mode (P mode) undergoes a slope reduction which can be directly related to a reduction in the corresponding modulus caused by magnetic attraction. Less intuitive is the fact that the branch for the shear mode (S mode) is characterized by an increase in slope which suggests that the equivalent shear modulus for the lattice increases for increasing attractive magnetization. In addition, it is interesting to observe that magnetization generates a bandgap between frequencies $\Omega \approx 0.8$

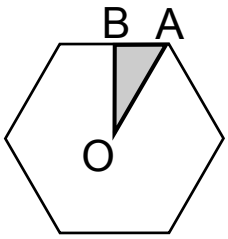

(a)

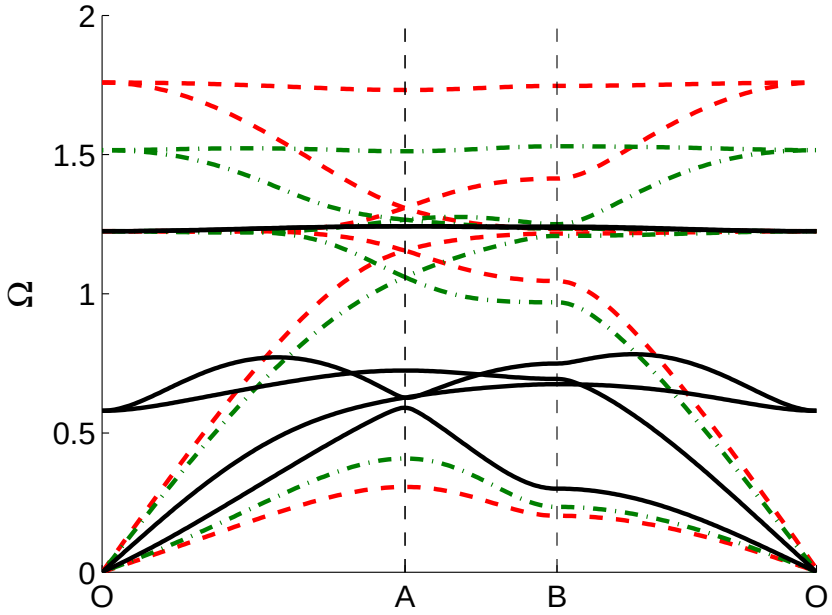

(b)

Figure 3.6: Irreducible Brillioun zone considered for the computation of the band diagram of the hexagonal lattice (a). Band structure for the hexagonal lattice and different levels of magnetization: $\bar{\psi}^{(m)} = 0$ (red $--$), $\bar{\psi}^{(m)} = -0.05$ (green $\cdot-$), and $\bar{\psi}^{(m)} = -0.1$ (black $-$) (b).

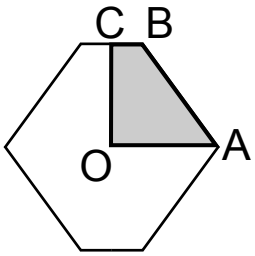

(a)

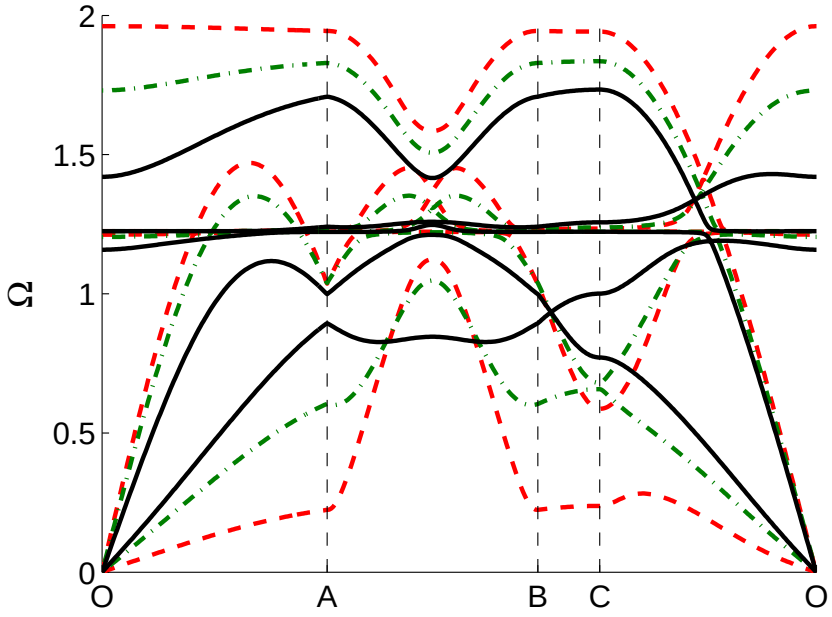

(b)

Figure 3.7: Irreducible Brillioun zone considered for the computation of the band diagram of the re-entrant lattice (a). Band structure for the re-entrant lattice and different levels of magnetization: $\bar{\psi}^{(m)} = -0.002$ (red $--$), $\bar{\psi}^{(m)} = -0.05$ (green $\cdot-$), and $\bar{\psi}^{(m)} = -0.1$ (black $-$) (b).

and $\Omega \approx 1.2$, which confirms the potentials for bandgap tunability of the considered designs observed in the 1D lattice analysis. The re-entrant lattice (Fig. 3.7) in the long wavelength limit ($\kappa \to 0$) is also characterized by the branch corresponding to the longitudinal mode (P mode) undergoing a slope reduction, while the slope of the shear mode (S mode) increases with magnetization. The re-entrant lattice experiences a significantly greater change in the S mode and there are no low frequency bandgaps ($\Omega < 2$) that open as the lattice is magnetized.

Of interest is also the evaluation of directionality of the dispersion surfaces and of the group velocity as indication of anisotropy of the lattice. Examples of iso-frequency contours of dispersion surfaces for the hexagonal and re-entrant lattices are shown respectively in Fig. 3.8 and Fig. 3.10, to illustrate their variation as a function of magnetization. A frequency value of $\Omega = 0.5$ is selected as representative of the behavior above the long wavelength limit. For the hexagonal lattice (Fig. 3.8), at this frequency only the P mode (black $-$ curve) propagates and its circular dispersion contour suggests the isotropic behavior of the lattice for low magnetization levels (Fig. 3.8(a,b)). In contrast, higher magnetizations lead to the propagation of both wave modes, which are anisotropic and reflect the six-fold symmetry of the lattice (Fig. 3.8(c)). This is further confirmed by the group velocity plots for both modes and the considered magnetization levels shown in Fig. 3.9. The group velocity directional variation illustrates the pattern by which the energy propagates within the lattice, and essentially describes the shape of the wavefront of a wave packet at this frequency. In Fig. 3.9 and Fig. 3.11 the group velocities are normalized with respect to the velocity of the P mode in an unmagnetized hexagonal lattice for the long wavelength case ($\kappa \to 0$). The group velocity directional variation illustrates the pattern by which the energy propagates within the lattice, and essentially describes the shape of the wavefront of a wave packet at this frequency. For low magnetizations (red $--$ curve), the P mode is characterized by circular group velocity plots, indicating that the velocity is constant in every direction. For the highest magnetization considered (black $-$ curve), both modes

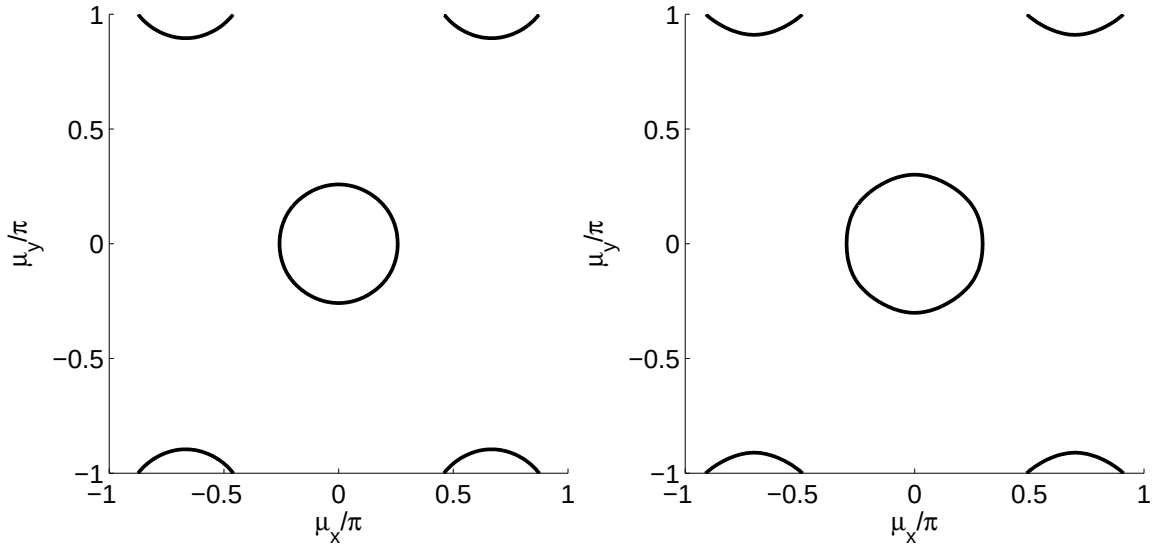

(a)

(b)

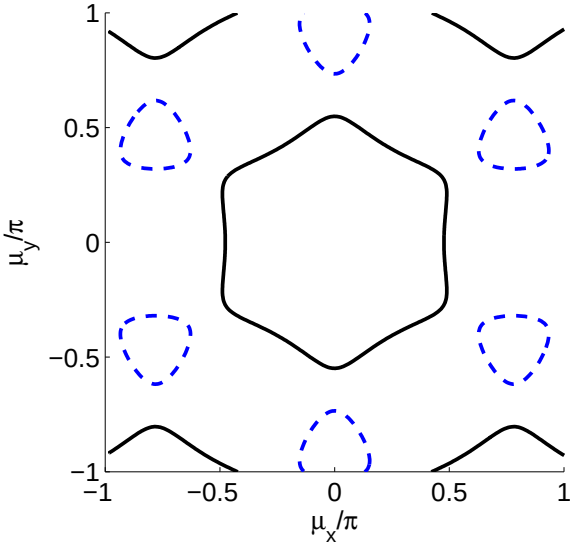

(c)

Figure 3.8: Isofrequency dispersion surfaces P mode (black $-$) and S mode (blue $--$) at $\Omega = 0.5$ for hexagonal lattice and various magnetization levels: $\bar{\psi}^{(m)} = 0$ (a), $\bar{\psi}^{(m)} = -0.05$ (b), $\bar{\psi}^{(m)} = -0.1$ (c).

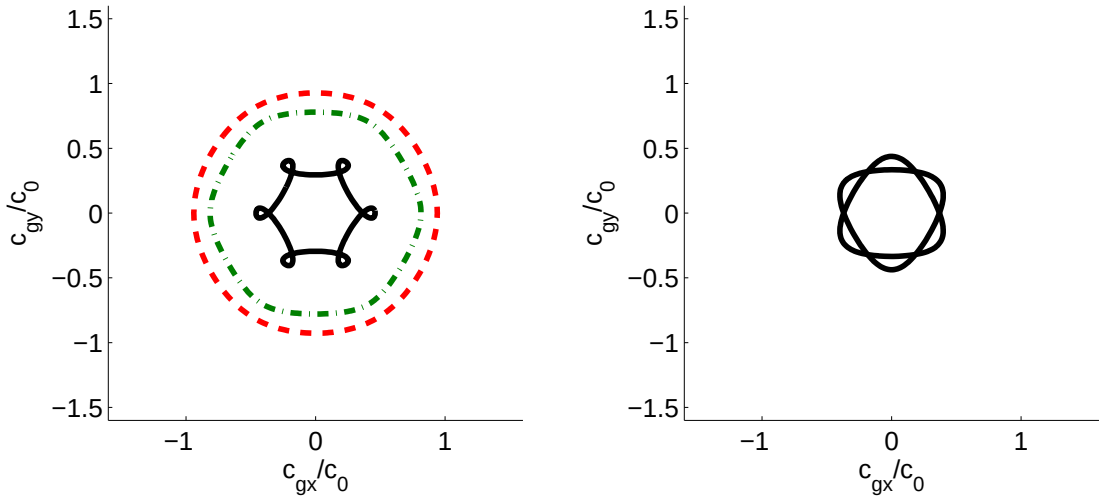

(a) P Mode

(b) S Mode

Figure 3.9: Variation of group velocity for hexagonal lattice at $\Omega = 0.5$ for various magnetizations ($\bar{\psi}^{(m)} = 0$ (red $--$), $\bar{\psi}^{(m)} = -0.05$ (green $\cdot-$), and $\bar{\psi}^{(m)} = -0.1$ (black $-$)): P mode (a) and and S mode (b). S mode does not exist at the considered frequency for lower magnetization levels.

feature angular changes in group velocity, and more importantly the occurrence of closed loops, or *caustics* at angles corresponding to the hexagonal structure. These closed loops are known to be indicative of directional wave motion and focusing [94]. The magnitude of the P mode group velocity also decreases with increasing magnetization, in accordance with the stiffness reduction caused by attractive magnets. At this frequency ($\Omega = 0.5$) the S mode is not present for all magnetizations. However, because of the shear stiffening caused by magnetization discussed earlier, the S mode exists at $\Omega = 0.5$ for high enough magnetizations. It is therefore interesting to note how the presence of magnetization can induce multi-modal wave propagation, as well as directional wave motion. Results for the re-entrant lattice are shown in Fig. 3.10, which illustrates a strongly anisotropic behavior for both modes at this frequency, and dispersion contours that vary significantly with magnetization in particular for the S mode (blue $--$ curve). The group velocity plots of Fig. 3.11 illustrate directional wave motion for both modes and the considered magnetization levels

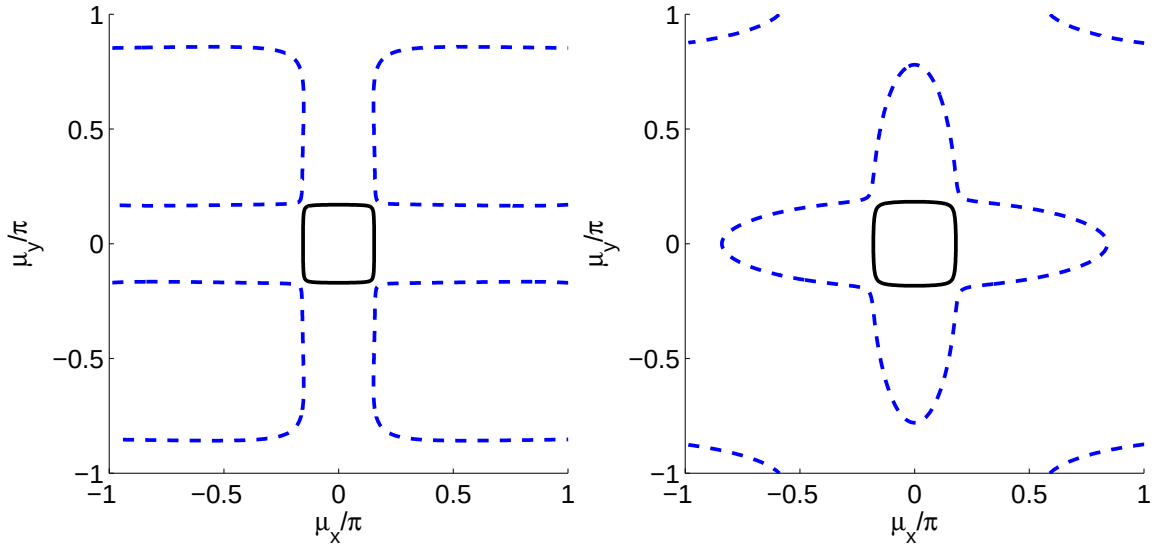

(a)

(b)

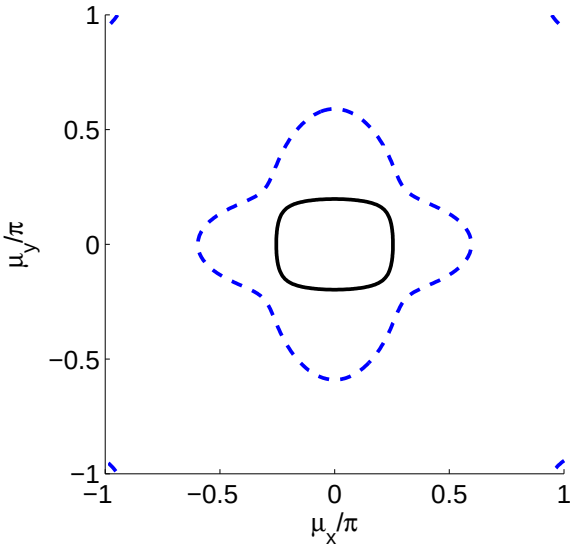

(c)

Figure 3.10: Isofrequency dispersion surfaces P mode (black $-$) and S mode (blue $--$) at $\Omega = 0.5$ for re-entrant lattice and various magnetization levels: $\bar{\psi}^{(m)} = -0.002$ (a), $\bar{\psi}^{(m)} = -0.05$ (b), $\bar{\psi}^{(m)} = -0.1$ (c).

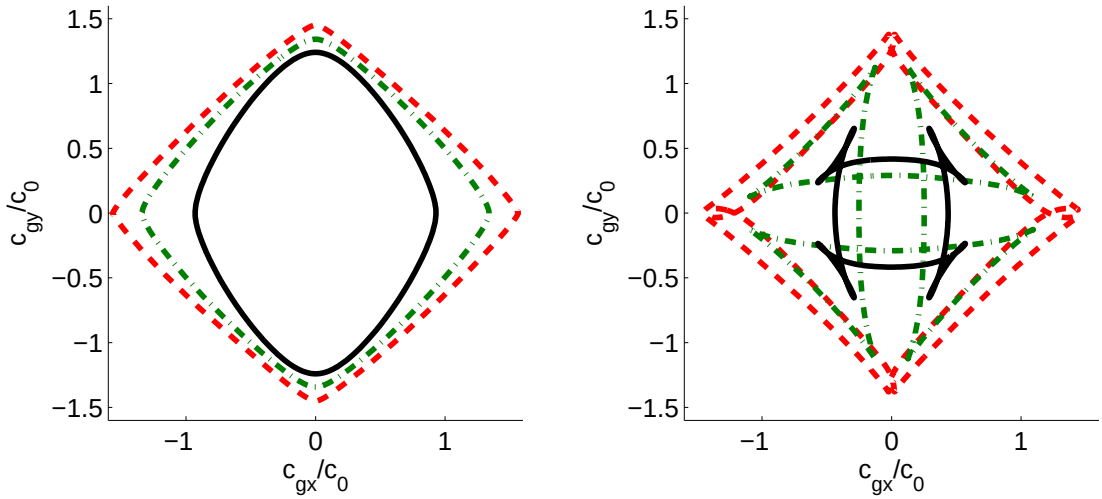

(a) P Mode (b) S Mode

Figure 3.11: Variation of group velocity for re-entrant lattice at $\Omega = 0.5$ for various magnetizations ($\bar{\psi}^{(m)} = -0.002$ (red $--$), $\bar{\psi}^{(m)} = -0.05$ (green $\cdot-$), and $\bar{\psi}^{(m)} = -0.1$ (black $-$)): P mode (a) and and S mode (b).

for the re-entrant lattice. As the magnetization is increased caustics form, suggesting that shear waves will be focused in the corresponding directions.

Numerical simulation of wave propagation

The propagation of perturbations through the lattices here considered is investigated through numerical simulations that account for all nonlinearities in the system. The finite lattice size is selected to include at least 10 unit cells along each dimension which provides sufficient spatial extent to observe the characteristics of wave motion and reduces the effects of boundaries. As previously, lattice size is limited by computational cost. The parameters considered are the same used for the dispersion analysis, i.e. $r_c = 0.5r_0$, $\alpha = 40$, $\omega_0^2 = k_a/m = 1$ rad^2/s^2, $I = \frac{1}{32}mr_0^2$, $\omega_r^2 = k_t/I = \frac{1}{2}$ rad^2/s^2, and $\bar{\psi}^{(m)}$ is set to -0.05. As in the 1D case, the time is normalized with respect to a characteristic time $t_0 = L/c_0$ with c_0 as the wave speed in an unmagnetized hexagonal lattice in the long wavelength limit ($\kappa \to 0$), just as in Section 3.4.1, and L as the width of the lattice. The lattice is excited by

a force applied to one point on the left side of the domain which varies as a Hanning windowed sine burst of 6 cycles, at frequency $\Omega = 0.5$, and amplitude of $F = 1 \times 10^{-3} k_a r_0$. This amplitude is chosen as a value that is expected not to lead to any reconfiguration of geometry and to be associated with a structural response that is governed by linear interactions. The results for the hexagonal lattice (Fig. 3.12(a-d)) show the nearly uniform propagation of the P mode as predicted in Fig. 3.6, and the noticeable absence of a shear-like mode for this level of magnetization (see Fig. 3.9). A reasonable agreement between the group velocity predicted by Bloch analysis and the wavefront velocity observed in this finite lattice simulation is noted. The re-entrant lattice results of Fig. 3.12(e-h) are in contrast of more difficult interpretation due to the presence of two wave modes as predicted by Fig. 3.7, 3.10, and 3.11. The limited size of the lattice makes the separation of the two modes difficult, possibly requiring the application of a modal filtering procedure similar to the one found in [32]. Of note, however, is the significantly different propagation pattern compared to the hexagonal lattice. The re-entrant lattice is here characterized by strongly directional propagation, and the presence of specific "beams" that correspond to the directions associated with the caustics in Fig. 3.11(b) for the shear-like mode.

Another set of simulations evaluates the response of the lattice to a broad-band, rectangular input of the kind shown in Fig. 3.13. The lattice configuration is shown in Fig. 3.14, whereby the horizontal motion of all nodes on the right boundary are constrained, and the point at mid height of the boundary is also constrained in its vertical motion as indicated respectively by the red and blue crosses in the figure. Time domain integration of the lattice equations is conducted for different amplitudes of forcing F, while keeping the duration of the pulse constant. The amplitude is progressively increased to allow the observation of the different propagation patterns that arise in the presence of configurational transitions and the comparison with instances where such transitions do not take place. The duration of the pulse is held constant to cover a range of frequencies that is associated with long wavelength deformations, and where the lattice is non-dispersive, to limit the number of studies.

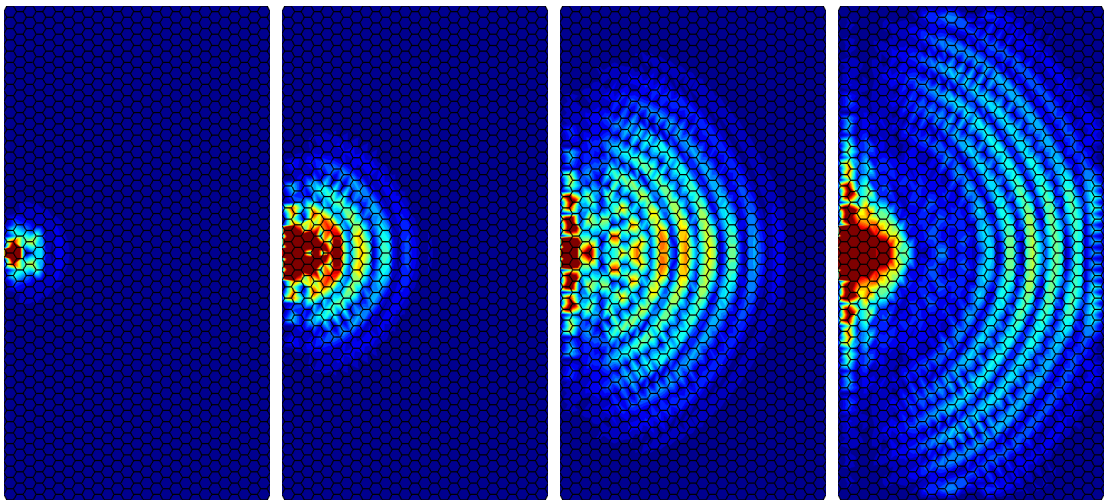

(a) $\tau = 0.4$ (b) $\tau = 0.8$ (c) $\tau = 1.2$ (d) $\tau = 1.6$

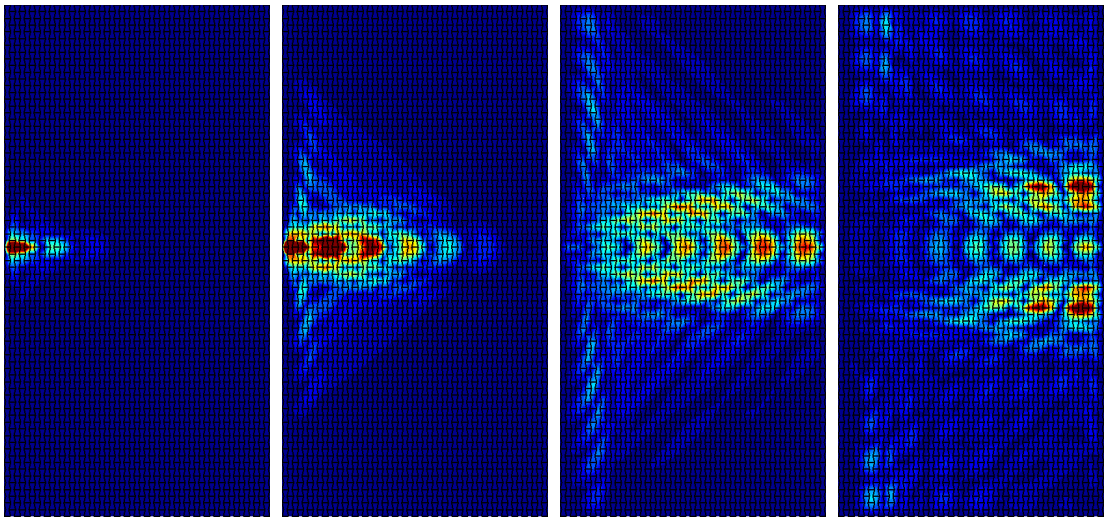

(e) $\tau = 0.4$ (f) $\tau = 0.8$ (g) $\tau = 1.2$ (h) $\tau = 1.6$

Figure 3.12: Snapshots of wave fields at dimensionless times $\tau = t/t_0$ propagating in hexagonal (a-d) and re-entrant (e-h) lattices for narrow band excitation at $\Omega = 0.5$ and small amplitude corresponding to linear wave motion. The color denotes the magnitude of the total displacment of a node with red denoting the greatest displacement and blue denoting none.

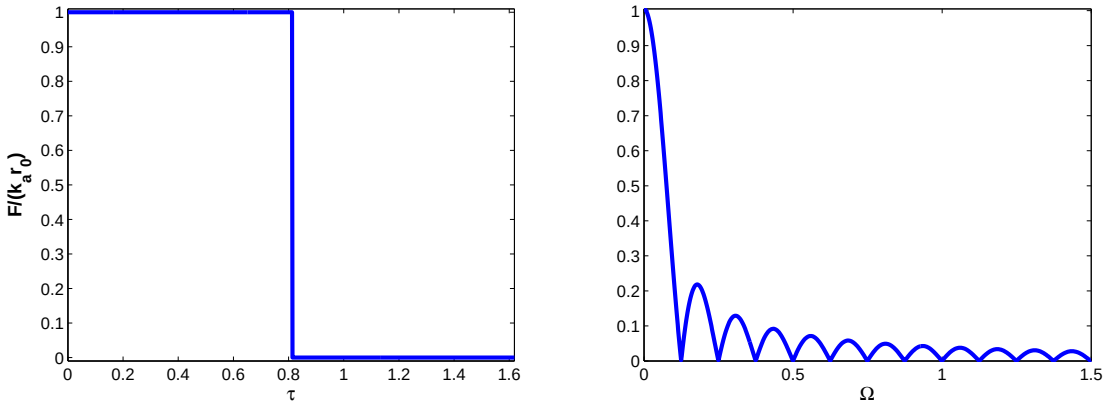

(a) (b)

Figure 3.13: Applied pulse: time domain (a) and frequency domain (b) representation showing bandwidth of excitation.

This range is of particular interest as in these conditions, the lattice can be considered as a solid with equivalent mechanical properties that are defined by elastic and magnetic interactions and by the lattice configuration. Figures 3.15 show snapshots of wave fields resulting from low amplitude pulses and illustrate some interesting differences with respect to the narrow band input case previously described. The case corresponding to Figures 3.15(a-d) is characterized by a circular wavefront followed by a second wavefront, most likely associated with the shear-like mode, that seems to reflect the six-fold symmetry of the lattice. This is even more evident for higher amplitude input as in the case of Fig. 3.15(e-h). The directional properties of the lattice deformation becomes evident for large amplitude inputs as considered in Fig. 3.16, where the first wavefront propagates preferentially along three directions that reflect the initial hexagonal symmetry of the lattice. The directional characteristics of the leading wavefront produces strongly directional transition patterns, i.e. the local reconfiguration of the lattice components is not the same in all directions. This is particularly evident in Fig. 3.16(e-h), which correspond to the highest amplitude forcing considered during these investigations. To visualize the lattice reconfiguration black lines representing the axial springs in the lattice have been superimposed on the colored plot of particle displacements. It is hypothesized that the large amplitude wave propaga-

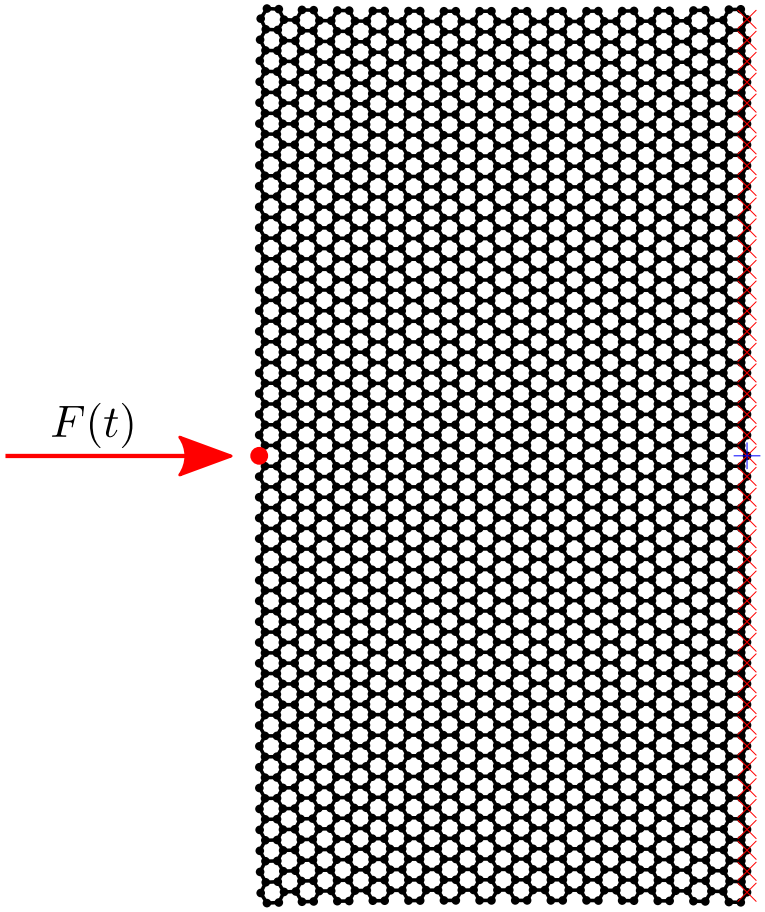

Figure 3.14: Loading configuration and boundary conditions considered for numerical simulations. Red and blue crosses denote constraints against horizontal and vertical motion respectively.

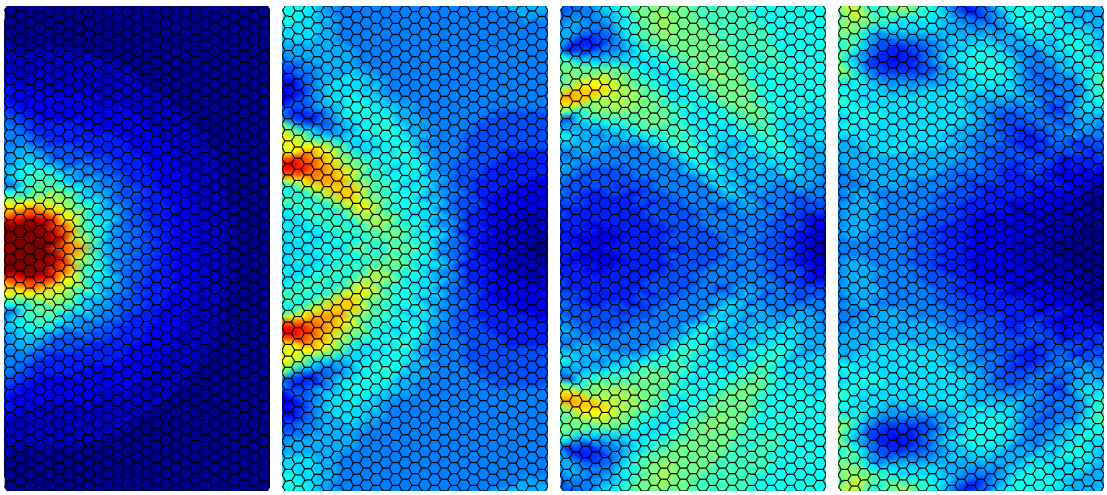

(a) $\tau = 1$ (b) $\tau = 2$ (c) $\tau = 3$ (d) $\tau = 4$

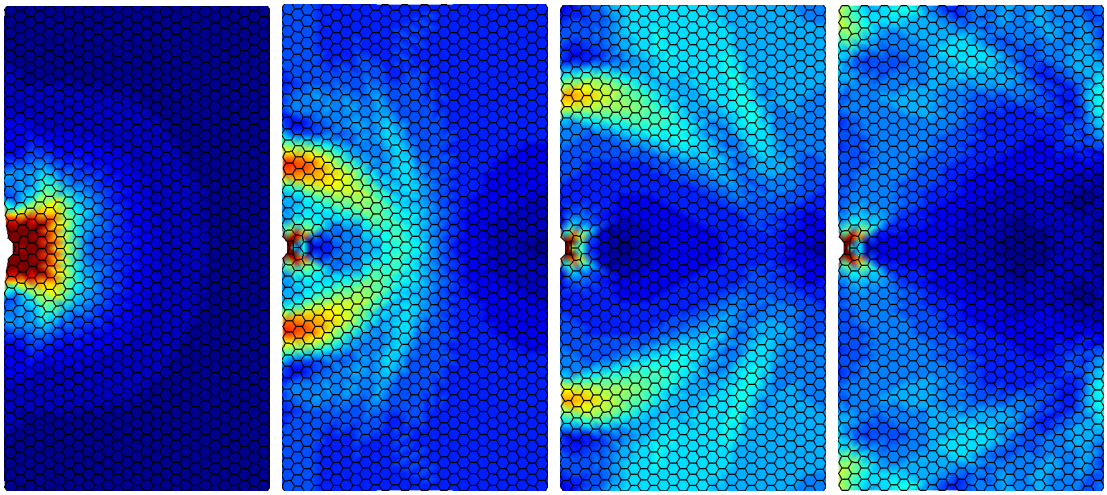

(e) $\tau = 1$ (f) $\tau = 2$ (g) $\tau = 3$ (h) $\tau = 4$

Figure 3.15: Snapshots of wave fields resulting from a low amplitude pulse. The pulse amplitudes are: (a-d) $F = 1 \times 10^{-4} k_a r_0$, (e-h) $F = 0.025 k_a r_0$. The color denotes the magnitude of the total displacment of a node with red denoting the greatest displacement and blue denoting none.

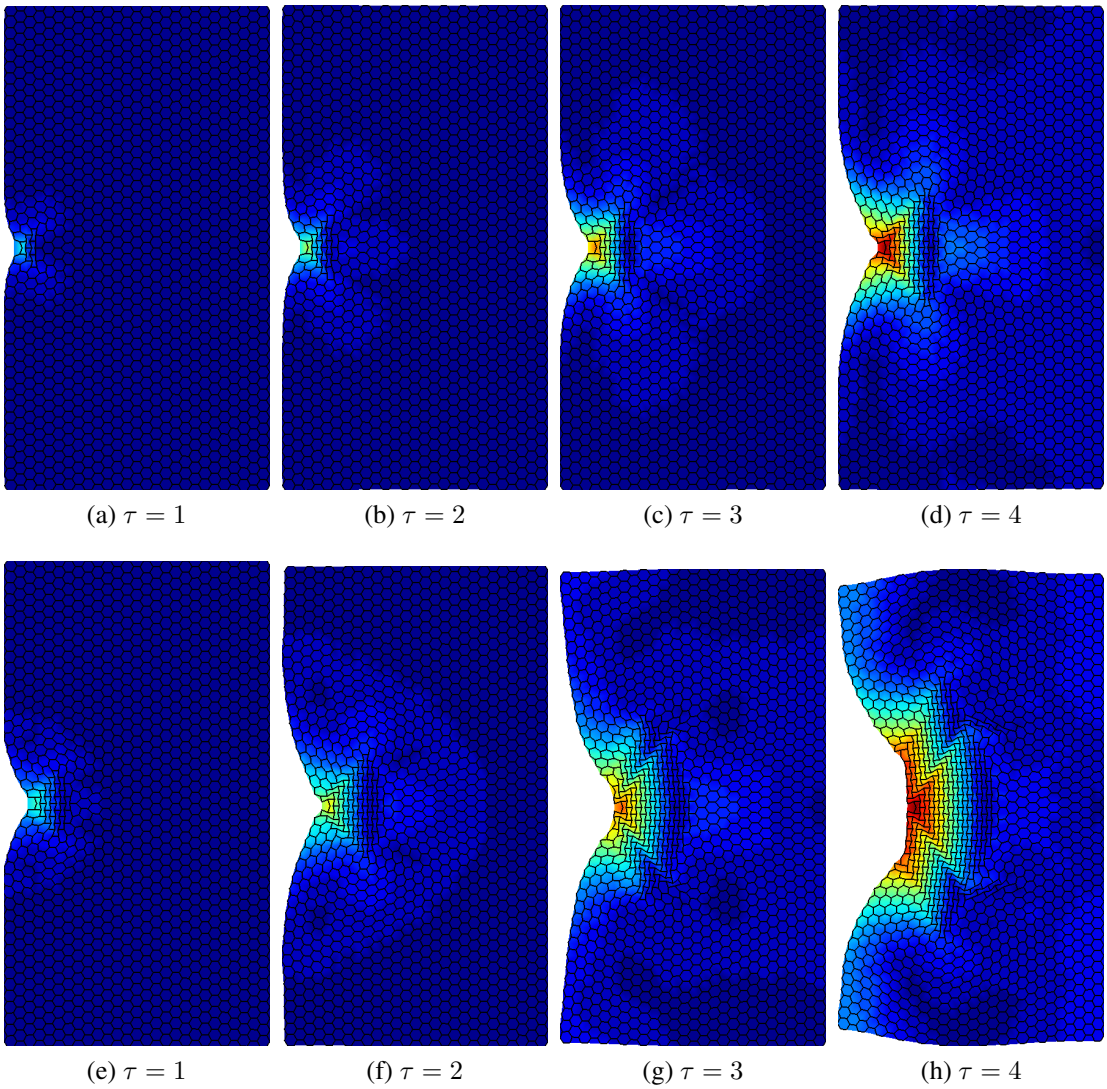

(a) $\tau = 1$ (b) $\tau = 2$ (c) $\tau = 3$ (d) $\tau = 4$

(e) $\tau = 1$ (f) $\tau = 2$ (g) $\tau = 3$ (h) $\tau = 4$

Figure 3.16: Snapshots of wave fields resulting from a high amplitude pulse. The pulse amplitudes are: (a-d) $F = 0.030 k_a r_0$, (e-h) $F = 0.100 k_a r_0$. The color denotes the magnitude of the total displacement of a node with red denoting the greatest displacement and blue denoting none.

tion properties of the structure effects the transformation patterns that occur. Hence, the directional characteristics of the wave front is likely the cause of the occurrence of "transition bands" that confine the propagation of the transition front. The so-called "transition bands" refer to the regions in Fig. 3.16(g-h) where there is a zigzag pattern in the locally emerging re-entrant patterns. Overall, the transition is characterized by strong directional characteristics, and may be related to the anisotropy of the lattice in one of its intermediate configurations in addition to the properties of the initial configuration.

3.4.2 Reconfigurable kagome lattices

Kagome lattice model description and geometric adaptation

The inspiration for the kagome lattice (KL) modeling discussed in this publication is the structure pictured in Fig. 3.17 where two of its possible stable configurations are shown. This structure is made of a molded elastomer, which allows it to undergo the large deformations required for reconfiguration. Permanent magnets are placed in the center of each of the triangular regions and nearest neighbor magnets attract. To model similar KL systems, which are not necessarily constructed in the same way, a lumped parameter approach is used which consists of linear axial and torsional springs connecting point masses. This simplified model still allows for the large geometric reconfigurations that bring about changes in global properties, which is of greatest interest in this publication. For simplicity, dissipative effects are neglected, but could be added by considering methodologies of the kind surveyed in [3]. These studies, however, go beyond the scope of this work.

The KLs to be modeled can be conceptualized as solid triangular elastic components with magnets at their centers connected by soft "hinges" at their corners. These hinges are assumed to have linear torsional elastic properties. The network of triangles is discretized into springs and point masses as represented by the unit cell in Fig. 3.18(a). The gray KL pattern pictured there shows the structure to be modeled and θ is the angle between triangles when the structure is undeformed. The entities representing the model of the structure are

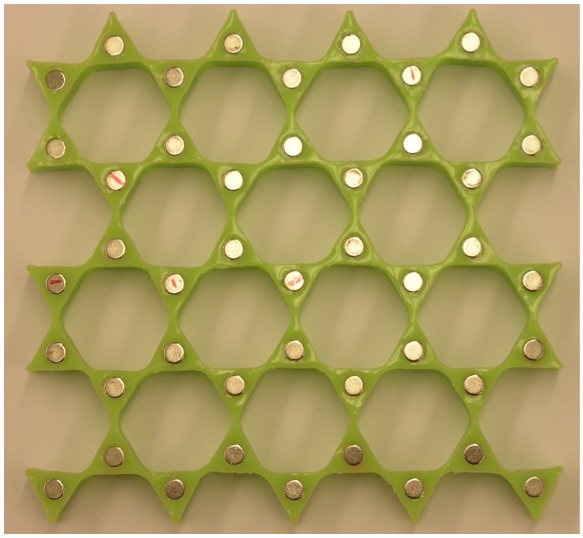

(a) Open Configuration

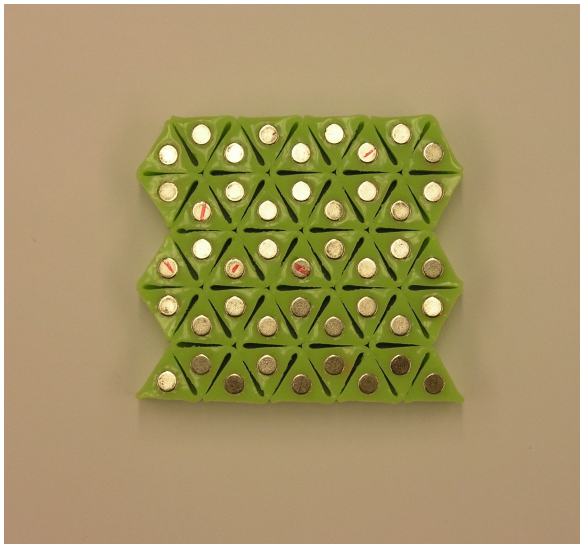

(b) Closed Configuration

Figure 3.17: Magneto-elastic kagome lattice structure.

as follows. The solid black lines represent linear elastic springs that do not bend. The large red circle and the blue ring are magnetized masses with anti-parallel polarizations and the smaller black circles are the mass that is lumped at the hinge locations. The torsional springs linking the rotations of the masses to the relative rotations of the axial springs are not shown. The dashed gray line bounds the unit cell and $\boldsymbol{d}_1$ and $\boldsymbol{d}_2$ are the lattice vectors. Very stiff torsional springs of stiffness $k_{\tau c}$ are placed around the magnetized mass in the center of each triangle, and softer torsional springs of stiffness $k_{\tau h}$ are placed at the hinges between the triangles. The radius of the hinge particles is r_p.

For simplicity only a few specific configurations are discussed in this publication (Fig. 3.18). These configurations are composed of the smallest unit cell that can describe a KL, which can be represented by 5 particles. The 4 general configurations that emerge in the lattices discussed are shown in Fig. 3.18. Two elastic lattices are used, which have an angle $\theta = 120^\circ$ (Fig. 3.18(a)) and $\theta = 60^\circ$ (Fig. 3.18(b)) between the triangles composing the unmagnetized structures. The $\theta = 120^\circ$ structure can exist in a so-called "open" (Fig. 3.18(c)) configuration, for low and no lattice magnetization, and its "closed" (Fig. 3.18(f)) configuration for magnetizations sufficient to overcome the torsional hinge springs. The $\theta = 60^\circ$ structure will exhibit its "open" configuration (Fig. 3.18(d)) when unmagnetized, intermediate configurations (Fig. 3.18(e)) for moderate magnetizations (with the angular deformation determined by the magnetization), and "closed" configuration (Fig. 3.18(f)) for sufficiently high magnetization.

Dispersion diagrams and wave velocities

The wave properties of a 2D KL with attractive nearest neighbor magnetic forces is considered. Since results are dimensionless for the purpose of generality ratios of parameters relative to one another are provided instead of parameters.

To model the KL the torsional springs about the centers of the triangles $k_{\tau c}$ are made much stiffer than those at the hinges $k_{\tau h}$ such that $k_{\tau c}/k_{\tau h} = 100$. This ratio of stiff-

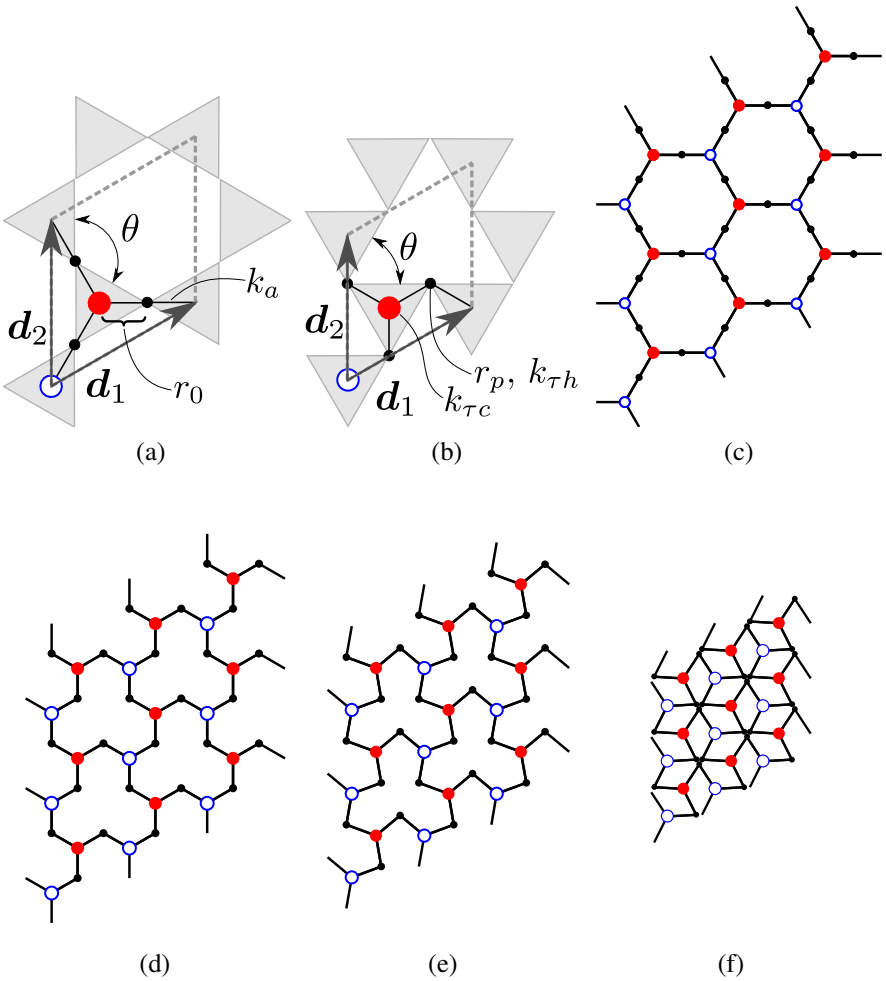

Figure 3.18: (a) KL unit cell for $\theta = 120°$ and (b) $\theta = 60°$. (c) Open KL configuration for $\theta = 120°$. (d,e) Open configuration for $\theta = 60°$ unmagnetized and magnetized respectively. (f) Closed KL configuration which is the same for $\theta = 120°$ and $60°$.

nesses qualitatively captures the fact that the solid triangles composing the lattice are stiff compared to the hinges at their corners.

Though the torsional interactions in the lattice are captured through the rotational degrees of freedom of each particle, wave propagation modes in which local particle resonances are prominent are not expected in the physical systems that the model is made to mimic. Therefore, to remove the effect of local particle rotational resonances on wave propagation, the rotational resonant frequency of the masses at the center of the triangles and at the hinges is chosen to be much higher than the frequencies of the modes containing motion of the triangles relative to one another, effectively removing the rotational inertia of the particles. Thus $\omega_c^2 = 3k_{\tau c}/I_c = \omega_h^2 = 2k_{\tau h}/I_h = 3 \times 10^5$ where I_c and I_h are the rotational inertia of the particles at the triangle centers and hinges respectively.

The contact distance is $r_c = 2r_p = 0.2r_0$ to match the approximate half-width of the web between triangles in a real structure. The contact stiffness γ is 7, which is somewhat arbitrary, and has little effect on the results shown if increased. The mass of the particles at the hinges relative to the magnets is 0.1, so not all mass is lumped in the center of the triangles. Furthermore, the stiffness of axial springs k_a is related to the magnet mass m by $\omega_n^2 = k_a/m = 1$ rad^2/s^2, and $k_{\tau c}/(mr_0^2) = 1$ rad^{-1} for convenience. Finally, $\varepsilon_e^{(m)} = 10^{-6}$ defines r_∞. In the following band diagrams let Ω be the dimensionless frequency of a plane wave defined as $\Omega = \omega/\sqrt{k_a/m}$.

A band diagram for the $\theta = 120^\circ$ structure (Fig. 3.18(a)) is presented in Fig. 3.19 for both the open and closed configuration. The lattice's band diagram in the open configuration (Fig. 3.18(c)) is relatively insensitive to changes in $\bar{\psi}^{(m)}$. Therefore, only small changes can be achieved on a broad band level by these means and only results for $\bar{\psi}^{(m)} = 0$ are shown. The lattice vectors shorten only about 3% between $\bar{\psi}^{(m)} = 0$ and $\bar{\psi}^{(m)} = 0.2$ due to the magnetic attraction, so there is not much of an effect on the equilibrium geometry. As $\bar{\psi}^{(m)}$ increases beyond 0.2 the open configuration of the lattice becomes unstable and the lattice will collapse or fold. The band structure of the collapsed/closed configuration

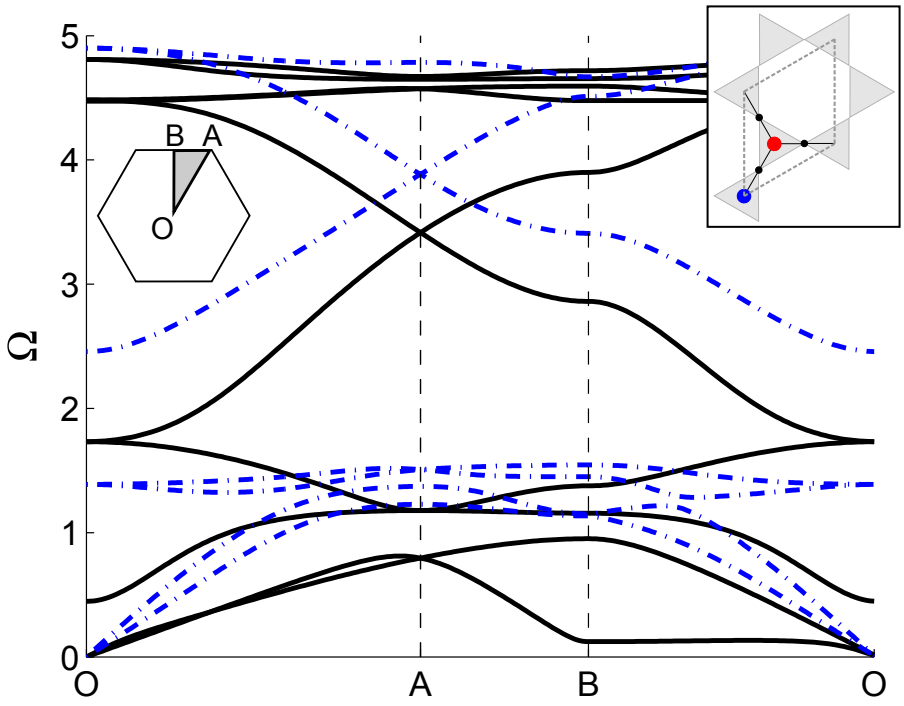

Figure 3.19: Band tunability of $\theta = 120°$. Open configuration $\bar{\psi}^{(m)} = 0$ (solid black), closed configuration $\bar{\psi}^{(m)} = 0.025$ (blue dot-dashed).

is shown near the lowest magnetization at which it can exist $\bar{\psi}^{(m)} = 0.025$ (Fig. 3.18(f)), since sufficient magnetic forces are required to hold the structure closed. Three of the bands have moved to higher frequencies and are not shown. The frequencies that they move to depend on γ, which is 7 in this case, with higher γ moving them to higher frequencies. The collapsed structure has a wide bandgap, which is a significant change from the open configuration. The width of this bandgap is slightly tunable with changing $\bar{\psi}^{(m)}$. The lower frequency bands of the KL also show a noticeable transformation due to the reconfiguration, which has a significant effect on the wave velocities shown later. One notable change is that the lattice is less dispersive for frequencies below $\Omega \approx 1$ once collapsed, as the shear (S) and pressure (P) mode move to higher frequencies.

A band diagram for $\theta = 60°$ (Fig. 3.18(b)) is presented in Fig. 3.20 for both the open and closed configuration. In contrast with the $\theta = 120°$ structure the bands are noticeably affected by changes in $\bar{\psi}^{(m)}$ and intermediate equilibrium configurations can be achieved

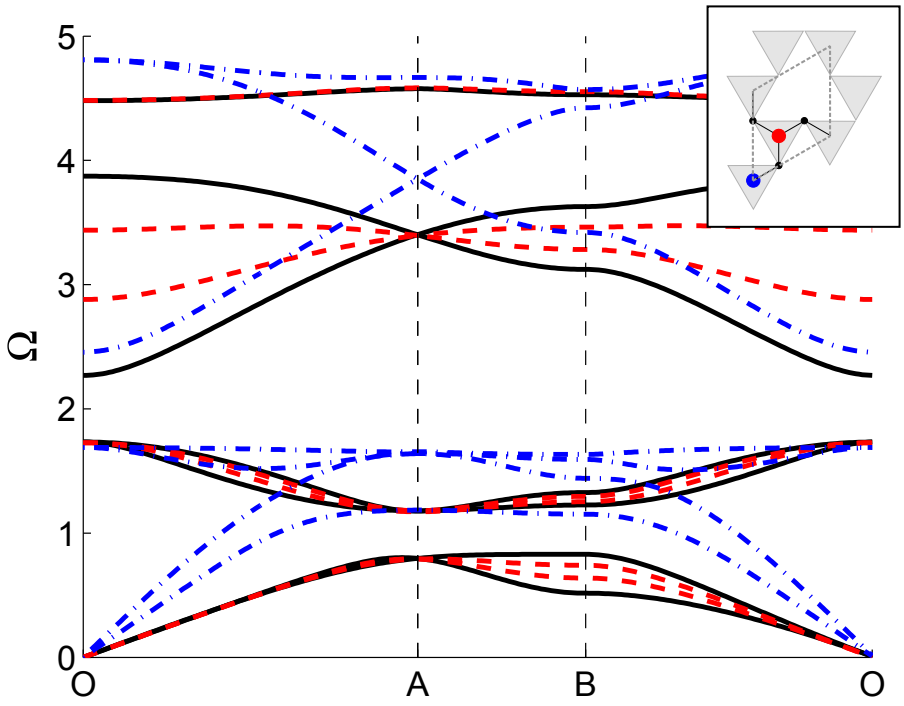

Figure 3.20: Band tunability of $\theta = 60°$. Open configuration $\bar{\psi}^{(m)} = 0$ (solid black), open configuration $\bar{\psi}^{(m)} = 0.019$ (red dashed), closed configuration $\bar{\psi}^{(m)} = 0.020$ (blue dot-dashed).

in which the angle between connected solid triangles will vary. The lattice vectors shorten by 11% between $\bar{\psi}^{(m)} = 0$ and $\bar{\psi}^{(m)} = 0.019$ and the angle between connected solid triangles changes by $9.8°$, all without collapsing to the closed configuration. Varying $\bar{\psi}^{(m)}$ through this range can double the width of the band gap at $\Omega \approx 2$. As $\bar{\psi}^{(m)}$ increases beyond 0.019 the open configuration of the lattice becomes unstable and the structure will assume the closed configuration (Fig. 3.18(f)). The band structure of the collapsed/closed configuration is shown at $\bar{\psi}^{(m)} = 0.020$ and it is similar to the band diagram shown for the collapsed $\theta = 60°$ structure. The bandgap at $\Omega \approx 2$ remains after the reconfiguration, but narrows somewhat from the $\bar{\psi}^{(m)} = 0.019$ open configuration.

Group velocities c_g for $\theta = 120°$ are shown in Fig. 3.21. The velocities are normalized with respect to the wave velocity c_0 of the $\theta = 120°$ structure when $\bar{\psi}^{(m)} = 0$ and $\Omega \to 0$. The frequency chosen captures the "quasi-isostatic" [40], i.e. low strain energy, mode of the unmagnetized KL in the S-mode band, which is very directionally biased. Without

the torsional hinge springs this would be a zero frequency "isostatic" mode of the kagome lattice between points O and B in Fig. 3.19. The restoring force in this mode is largely due to the rotational springs, and since they are fairly soft the mode exhibits a low frequency between points O and B in addition to slow group velocities. The loops or "caustics" in the plot are indicative of beaming, which is a focusing of the wave energy in certain directions [3]. There are so many curves for the S-mode of the unmagnetized case because at the frequency shown there is more than one wavelength that can propagate. The P-mode also shows faster propagation along some of the the same directions for which the S-mode shows beaming. For waves propagating in the closed configuration at the same frequency the length of the waves compared to the unit cell becomes large enough that the continuum assumption may be valid. At this point the structure is essentially non-dispersive, which is shown in the linearity of the bands in Fig. 3.19. Furthermore, the group velocities are essentially constant with changing direction in the closed configuration, as in an isotropic material. The maximum P-mode wave speed seen in the open configuration is nearly the same wave speed observed for minimal magnetization of the closed configuration. It is also seen that increasing the magnetization of the closed configuration reduces the wave speeds at this frequency because the attractive magnetic forces have a softening effect on the effective stiffness of the structure. In addition, though not shown for brevity, increasing $\bar{\psi}^{(m)}$ of the closed configuration at higher frequencies $\Omega > 0.5$ can introduce small directional biases.

Group velocities for $\theta = 60^\circ$ are shown in Fig. 3.22. The frequency chosen for the plots ($\Omega = 0.3$) shows how magnetization of the open configuration of $\theta = 60^\circ$ can reduce the anisotropy of the lattice and tune the wave speeds. The values of $\bar{\psi}^{(m)}$ shown are the full range for which the open configuration remains stable and therefore show the full amount by which the open configuration can be tuned with changing magnetization. The closed configuration for $\theta = 60^\circ$ is quite similar to the one for $\theta = 120^\circ$ so the results of further magnetization are not shown.

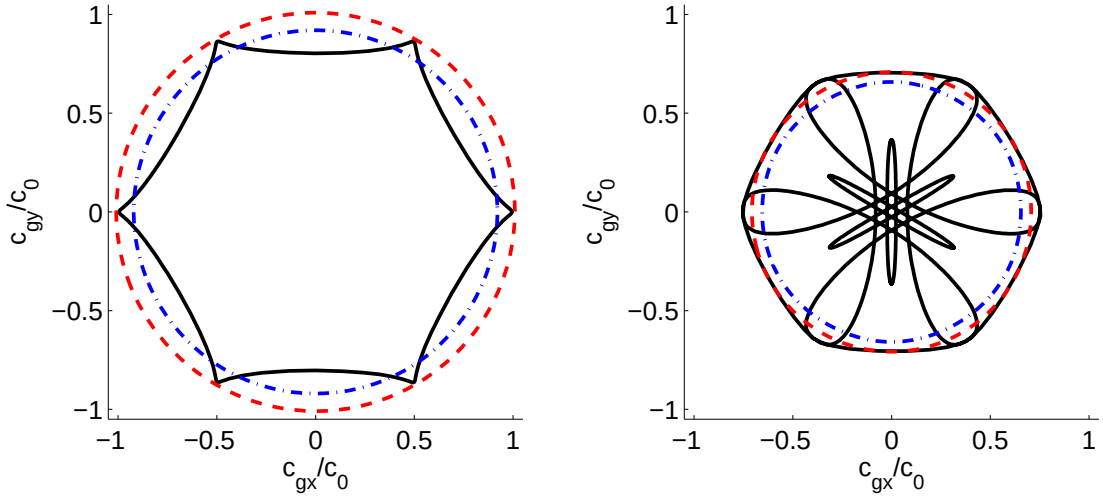

(a) P-Mode (b) S-Mode

Figure 3.21: Variation in group velocity at $\Omega = 0.127$ due to reconfiguration and magnetization for $\theta = 120°$. Open configuration $\bar{\psi}^{(m)} = 0$ (solid black), closed configuration $\bar{\psi}^{(m)} = 0.025$ (red dashed), closed configuration $\bar{\psi}^{(m)} = 0.125$ (blue dot-dashed).

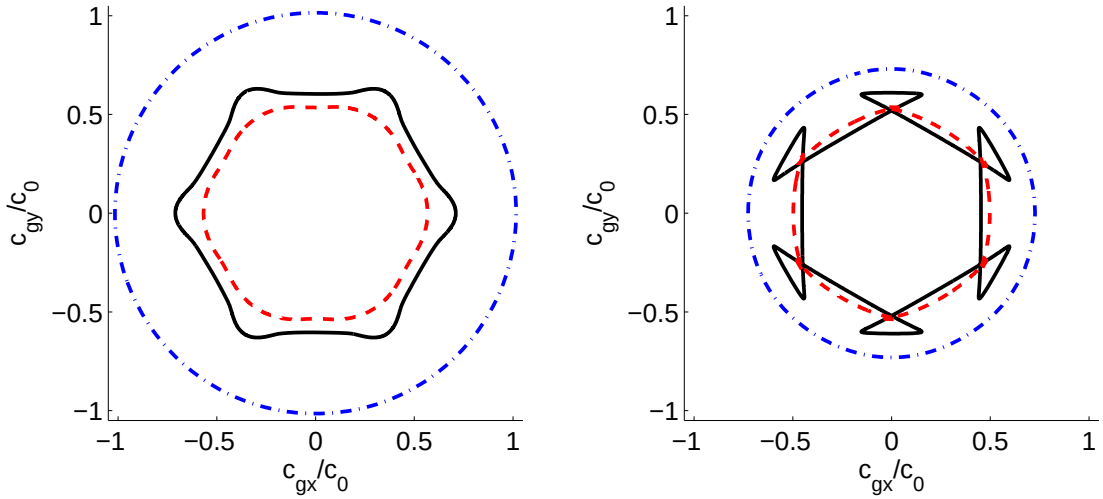

(a) P-Mode (b) S-Mode

Figure 3.22: Variation in group velocity at $\Omega = 0.3$ due to reconfiguration and magnetization for $\theta = 60°$. Open configuration $\bar{\psi}^{(m)} = 0$ (solid black), open configuration $\bar{\psi}^{(m)} = 0.019$ (red dashed), closed configuration $\bar{\psi}^{(m)} = 0.020$ (blue dot-dashed).

CHAPTER 4
HOMOGENIZATION OF MAGNETO-ELASTIC STRUCTURES

4.1 Chapter overview

The purpose of this chapter is to quantify the effect that lattice reconfiguration has on the equivalent continuum properties of a lattice. To do so, a homogenization methodology for elastic lattices [50] is extended and applied to some of the lattices discussed previously in Chapters 2 and 3. Over an order of magnitude change in homogenized stiffness is seen to be possible through reconfiguration, in addition to the introduction of anisotropy. 1D lattices are considered as linear elastic continuua and 2D lattices are considered as linear elastic orthotropic continuua. First the homogenization procedure is described. Then results for 1D cases are presented including numerical simulations for verification of the method. Finally, results for 2D hexagonal and re-entrant lattices are presented.

4.2 Homogenization procedure

4.2.1 Linearization about equilibrium

The considered homogenization approach assumes a linear elastic continuum. This requires linearization of the governing equations under the assumption that the lattice undergoes small displacements from a stable equilibrium. A first order Taylor series expansion is employed to linearize the forces. Thus, the gradient of the forces with respect to the unit cell DOFs defines a stiffness matrix, and the equations of motion for a unit cell can be expressed as in Eq. (3.3).

4.2.2 Reduction of the degrees of freedom

The homogenization method, developed by [50], derives an equation of motion from the lattice structure that is compared to the continuum equations of motion in order to extract the mechanical properties. Before the method is applied the lattice must be reduced to an equivalent system with only one particle per unit cell, which ensures that the spacing between the particles makes a square grid in the lattice coordinate space. This is required to achieve cancellation between the 1st order partial derivatives that would otherwise manifest in the equation of motion derived by the homogenization method and break the analogy to the continuum equation of motion. Guyan reduction [95] accomplishes this task. Through the algebraic manipulation and substitution in Guyan reduction the n_m DOFs of the master particles m are used to define the n_s DOFs of the slave particles s. Any particle in a unit cell can be chosen as the master particle as long as the same particle is chosen in each unit cell. Partitioning the equation of motion into master and slave DOFs gives:

$$\left(\boldsymbol{K}-\omega^2\boldsymbol{M}\right)\boldsymbol{q} = \left(\begin{bmatrix}\boldsymbol{K}_{mm} & \boldsymbol{K}_{ms}\\ \boldsymbol{K}_{ms}^T & \boldsymbol{K}_{ss}\end{bmatrix} - \omega^2\begin{bmatrix}\boldsymbol{M}_{mm} & \boldsymbol{M}_{ms}\\ \boldsymbol{M}_{ms}^T & \boldsymbol{M}_{ss}\end{bmatrix}\right)_{n_{dof}\times n_{dof}}\begin{Bmatrix}\boldsymbol{q}_m\\ \boldsymbol{q}_s\end{Bmatrix}_{n_{dof}\times 1} = \boldsymbol{0} \tag{4.1}$$

where $n_{dof} = n_m + n_s$ is the number of DOFs describing the particles within the distance r_∞ from a reference unit cell.

Though the equilibrium geometry of the structure is periodic, the deformation is arbitrary and cannot be described by the reference unit cell alone. Therefore, Eq. (4.1) is the equation of motion for an entire structure, not just one cell as Eq. (3.3), and $[\boldsymbol{q}_m;\boldsymbol{q}_s]$ contains the $\boldsymbol{q}_{m,n}$ corresponding to all m,n pairs. Having Eq. (4.1), a transformation matrix is then calculated, which, when applied, solves for the master DOFs in terms of the slave

DOFs.

$$\boldsymbol{T} = \begin{bmatrix} \boldsymbol{I}_{n_m \times n_m} \\ -\boldsymbol{K}_{ss}^{-1}\boldsymbol{K}_{ms}^{T} \end{bmatrix}_{n_{dof} \times n_m} \tag{4.2}$$

where $\boldsymbol{I}$ is the identity matrix. Applying the transformation matrix produces the reduced mass and stiffness matrices $\boldsymbol{M}^{(r)}, \boldsymbol{K}^{(r)} \in \mathbb{R}^{n_m \times n_m}$, and the displacement vector $\boldsymbol{q}^{(r)} \in \mathbb{R}^{n_m \times 1}$.

$$\begin{aligned} \boldsymbol{M}^{(r)} &= \boldsymbol{T}^T \boldsymbol{M} \boldsymbol{T} \\ \boldsymbol{K}^{(r)} &= \boldsymbol{T}^T \boldsymbol{K} \boldsymbol{T} \\ \boldsymbol{q}^{(r)} &= \boldsymbol{q}_m \end{aligned} \tag{4.3}$$

In final preparation for homogenization methodology the mass and stiffness matrices are partitioned into blocks, each of which describe the effect of cell m, n's DOFs on the reference cell's DOFs. For the lattices studied, Eq. (4.4) separates out 3 equations from the n_m reduced equations of motion, which correspond to the three degrees of freedom of the master node in the reference unit cell.

$$\sum_{m=-M}^{M} \sum_{n=-N}^{N} \left(\boldsymbol{M}_{m,n}^{(r)} \ddot{\boldsymbol{q}}_{m,n}^{(r)} + \boldsymbol{K}_{m,n}^{(r)} \boldsymbol{q}_{m,n}^{(r)} \right) = \boldsymbol{0} \tag{4.4}$$

It is worth noting here that for a static problem Guyan reduction introduces no assumptions, and thus no error regarding static elastic properties.

4.2.3 Long-wavelength approximation

The homogenization method follows the procedure described in [50] and is summarized here. First the lattice coordinate space η_1, η_2 is defined using the lattice vectors $\boldsymbol{d}_1, \boldsymbol{d}_2$.

$$\begin{Bmatrix} x \\ y \end{Bmatrix} = \mathbf{E} \begin{Bmatrix} \eta_1 \\ \eta_2 \end{Bmatrix} \tag{4.5}$$

$$\mathbf{E} = \begin{bmatrix} \boldsymbol{d}_1 & \boldsymbol{d}_2 \end{bmatrix} = \begin{bmatrix} e_{11} & e_{12} \\ e_{21} & e_{22} \end{bmatrix} \tag{4.6}$$

Then it is assumed that the displacement of the particles is continuous in space and can be represented by a second order Taylor series in the lattice coordinate space η_1, η_2. Thus, the master DOFs of the cell $m\boldsymbol{d}_1 + n\boldsymbol{d}_2$ away from the reference unit cell may be approximated as:

$$\boldsymbol{q}_{m,n} \approx \boldsymbol{q}(\eta_1, \eta_2) + m\frac{\partial \boldsymbol{q}}{\partial \eta_1} + n\frac{\partial \boldsymbol{q}}{\partial \eta_2} + \frac{1}{2}m^2\frac{\partial^2 \boldsymbol{q}}{\partial \eta_1^2} + \frac{1}{2}n^2\frac{\partial^2 \boldsymbol{q}}{\partial \eta_2^2} + mn\frac{\partial^2 \boldsymbol{q}}{\partial \eta_1 \partial \eta_2} \tag{4.7}$$

Application of Eq. (4.7) to Eq. (4.4) produces:

$$\boldsymbol{F}'_m\ddot{\boldsymbol{q}} + \boldsymbol{A}'\frac{\partial^2 \boldsymbol{q}}{\partial \eta_1^2} + \boldsymbol{B}'\frac{\partial^2 \boldsymbol{q}}{\partial \eta_1 \partial \eta_2} + \boldsymbol{C}'\frac{\partial^2 \boldsymbol{q}}{\partial \eta_2^2} + \boldsymbol{D}'\frac{\partial \boldsymbol{q}}{\partial \eta_1} + \boldsymbol{E}'\frac{\partial \boldsymbol{q}}{\partial \eta_2} + \boldsymbol{F}'\boldsymbol{q} = \boldsymbol{f} \tag{4.8}$$

where, although the absence of external forcing will be assumed, a force vector $\boldsymbol{f}$ continuous in x, y is included for generality. Equation 4.8 assumes that $\boldsymbol{M}^{(r)}_{m,n} = \mathbf{0}$ for $m, n \neq 0$, meaning there is no inertial coupling between cells. Of note is the fact that the matrices in Eq. (4.8) are dependent not on nearest neighbors only but on the cells up to M or N indexes away, where $M, N \neq 1$ in general, allowing the inclusion of non-nearest neighbor

magnetic interactions. The matrices in Eq. (4.8) are defined:

$$\begin{aligned}
\boldsymbol{A}' &= \frac{1}{2}\sum_{m=-M}^{M}\sum_{n=-N}^{N} m^2 \boldsymbol{K}_{m,n}^{(r)} \quad & \boldsymbol{B}' &= \sum_{m=-M}^{M}\sum_{n=-N}^{N} mn\boldsymbol{K}_{m,n}^{(r)} \\
\boldsymbol{C}' &= \frac{1}{2}\sum_{m=-M}^{M}\sum_{n=-N}^{N} n^2 \boldsymbol{K}_{m,n}^{(r)} \quad & \boldsymbol{D}' &= \sum_{m=-M}^{M}\sum_{n=-N}^{N} m\boldsymbol{K}_{m,n}^{(r)} \\
\boldsymbol{E}' &= \sum_{m=-M}^{M}\sum_{n=-N}^{N} n\boldsymbol{K}_{m,n}^{(r)} & \boldsymbol{F}' &= \sum_{m=-M}^{M}\sum_{n=-N}^{N} \boldsymbol{K}_{m,n}^{(r)} \\
\boldsymbol{F}'_m &= \sum_{m=-M}^{M}\sum_{n=-N}^{N} \boldsymbol{M}_{m,n}^{(r)}.
\end{aligned} \tag{4.9}$$

Equation (4.9) differs from that in [50] as the typo omitting the $1/2$ from $\boldsymbol{A}'$ and $\boldsymbol{C}'$ has been fixed. In order to convert to the physical space x, y from the lattice coordinate space η_1, η_2 the derivatives are converted using:

$$\begin{Bmatrix} \frac{\partial}{\partial \eta_1} \\ \\ \frac{\partial}{\partial \eta_2} \end{Bmatrix} = \mathbf{E}^T \begin{Bmatrix} \frac{\partial}{\partial x} \\ \\ \frac{\partial}{\partial y} \end{Bmatrix} \tag{4.10}$$

$$\begin{Bmatrix} \frac{\partial^2}{\partial \eta_1^2} \\ \\ \frac{\partial^2}{\partial \eta_2^2} \\ \\ \frac{\partial^2}{\partial \eta_1 \partial \eta_2} \end{Bmatrix} = \begin{bmatrix} e_{11}^2 & e_{21}^2 & 2e_{11}e_{21} \\ \\ e_{12}^2 & e_{22}^2 & 2e_{22}e_{12} \\ \\ e_{11}e_{12} & e_{21}e_{22} & e_{12}e_{21} + e_{11}e_{22} \end{bmatrix} \begin{Bmatrix} \frac{\partial^2}{\partial x^2} \\ \\ \frac{\partial^2}{\partial y^2} \\ \\ \frac{\partial^2}{\partial x \partial y} \end{Bmatrix}. \tag{4.11}$$

Note that these equations differ from those in [50] slightly as two small typos have been fixed. The change of basis gives the continuum equation of motion in the physical space x, y:

$$\boldsymbol{F}_m \ddot{\boldsymbol{q}} + \boldsymbol{A}\frac{\partial^2 \boldsymbol{q}}{\partial x^2} + \boldsymbol{B}\frac{\partial^2 \boldsymbol{q}}{\partial x \partial y} + \boldsymbol{C}\frac{\partial^2 \boldsymbol{q}}{\partial y^2} + \boldsymbol{D}\frac{\partial \boldsymbol{q}}{\partial x} + \boldsymbol{E}\frac{\partial \boldsymbol{q}}{\partial y} + \boldsymbol{F}\boldsymbol{q} = \boldsymbol{f} \tag{4.12}$$

where $\boldsymbol{A}$, ..., $\boldsymbol{F}$, $\boldsymbol{F}_m$ are defined in terms of $\boldsymbol{A}'$, ..., $\boldsymbol{F}'$, $\boldsymbol{F}'_m$ and $\mathbf{E}$ as follows:

$$\begin{aligned}
\boldsymbol{A} &= e_{11}^2\boldsymbol{A}' + e_{11}e_{12}\boldsymbol{B}' + e_{12}^2\boldsymbol{C}' \\
\boldsymbol{B} &= 2e_{11}e_{21}\boldsymbol{A}' + (e_{12}e_{21} + e_{11}e_{22})\boldsymbol{B}' + 2e_{22}e_{12}\boldsymbol{C}' \\
\boldsymbol{C} &= e_{21}^2\boldsymbol{A}' + e_{21}e_{22}\boldsymbol{B}' + e_{22}^2\boldsymbol{C}' \\
\boldsymbol{D} &= e_{11}\boldsymbol{D}' + e_{12}\boldsymbol{E}' \\
\boldsymbol{E} &= e_{21}\boldsymbol{D}' + e_{22}\boldsymbol{E}' \\
\boldsymbol{F} &= \boldsymbol{F}' \\
\boldsymbol{F}_m &= \boldsymbol{F}'_m.
\end{aligned} \tag{4.13}$$

As a comparison will be made with the equation of motion for a continuum the equation must be expressed per unit volume V, which for a 2D structure is:

$$V = |\boldsymbol{d}_1 \times \boldsymbol{d}_2|b \tag{4.14}$$

where b is the out-of-plane thickness of the structure. The new equation of motion is:

$$\frac{1}{V}\left(\boldsymbol{F}_m\ddot{\boldsymbol{q}} + \boldsymbol{A}\frac{\partial^2\boldsymbol{q}}{\partial x^2} + \boldsymbol{B}\frac{\partial^2\boldsymbol{q}}{\partial x\partial y} + \boldsymbol{C}\frac{\partial^2\boldsymbol{q}}{\partial y^2} + \boldsymbol{D}\frac{\partial\boldsymbol{q}}{\partial x} + \boldsymbol{E}\frac{\partial\boldsymbol{q}}{\partial y} + \boldsymbol{F}\boldsymbol{q}\right) = \frac{\boldsymbol{f}}{V} = \boldsymbol{b} \tag{4.15}$$

where $\boldsymbol{b}$ is a vector of body forces.

From here the procedure of [50] is continued, omitting terms that decrease with the length scale of the micro structure ϵ^3. Then the rotational DOF θ is algebraically removed (assuming no moments are applied) and the 2 resulting equations are:

$$\begin{aligned}
f_{m_{xx}}\ddot{q}_x - a\frac{\partial^2 q_x}{\partial x^2} - b\frac{\partial^2 q_x}{\partial y^2} - c\frac{\partial^2 q_y}{\partial x\partial y} &= b_x \\
f_{m_{yy}}\ddot{q}_y - d\frac{\partial^2 q_y}{\partial x^2} - e\frac{\partial^2 q_y}{\partial y^2} - f\frac{\partial^2 q_x}{\partial x\partial y} &= b_y
\end{aligned} \tag{4.16}$$

where q_x, q_y and b_x, b_y are the components of $\boldsymbol{q}$ and $\boldsymbol{b}$ respectively, and $a \cdots f$ are constants.

Equation (4.16) is compared with the equations of motion for a thin orthotropic material (plane stress) which are:

$$\begin{aligned}\rho\ddot{q}_x - E_1'\frac{\partial^2 q_x}{\partial x^2} - G\frac{\partial^2 q_x}{\partial y^2} - (E_{12}' + G)\frac{\partial^2 q_y}{\partial x \partial y} &= b_x \\ \rho\ddot{q}_y - G\frac{\partial^2 q_y}{\partial x^2} - E_2'\frac{\partial^2 q_y}{\partial y^2} - (E_{12}' + G)\frac{\partial^2 q_x}{\partial x \partial y} &= b_y\end{aligned} \tag{4.17}$$

Comparing like terms allows algebraic solution of the density ρ the Young's moduli E_1 and E_2, the Poisson's ratios ν_{12} and ν_{21}, and the shear modulus G_{12} in terms of $a \cdots f$.

4.3 Homogenization of 1D magneto-elastic lattices

The procedure is first applied to the 1D lattices shown in Fig. 4.1(a) and Fig. 4.1(b). The analytical expressions of the equivalent properties of both structures derived below are used to check the convergence of the approximate solutions described in the previous section.

For both lattices the same approach is used. A variable s, used to denote the pattern type, allowing specification between the two lattices mathematically. It is -1 for alternating polarities (Fig. 4.1(b)) and 1 if all polarities are the same (Fig. 4.1a). First the equation of motion for the generic particle i is derived. It is assumed that the lattice is in equilibrium, and evenly spaced with distance h between all nearest-neighbor magnets. The equation of motion is:

$$m_p\ddot{u}_i + k_a(-u_{i-1} + 2u_i - u_{i+1}) + \sum_{n=1}^{\infty} k_n^{(m)}(-u_{i-n} + 2u_i - u_{i+n}) = 0 \tag{4.18}$$

where u_i is the displacement of particle i in the x direction, and $k_n^{(m)}$ is the equivalent linearized stiffness of the magnetic interaction with a particle distance hn away from particle i.

Assuming a continuous distribution of displacement, a second order Taylor series can be expanded about particle i for a step n, which approximates u_{i+n}. The i is dropped from

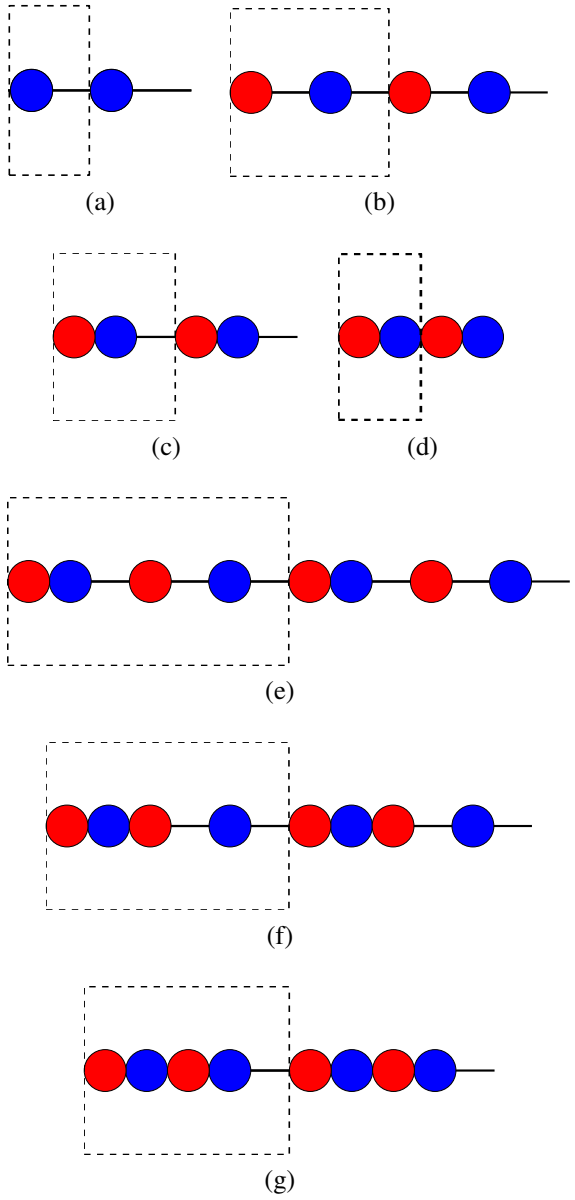

Figure 4.1: Periodic equilibrium examples for 1D structures with 1 (a), 2 (b-d), and 4 (e-g) particle unit cells. Red and blue circles denote magnets with dipole moments perpendicular to the lattice plane pointing towards and away from the reader respectively. Black lines denote elastic connections between magnets.

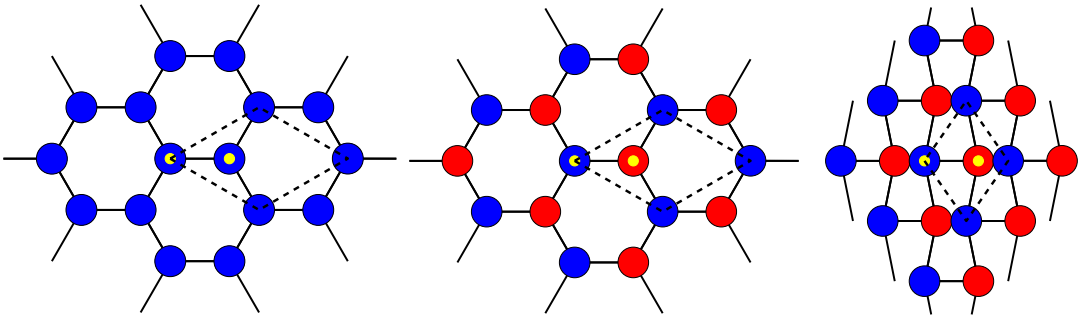

Figure 4.2: Periodic equilibrium examples for 2D structures with 2 particle unit cells. Red and blue circles denote magnets with dipole moments perpendicular to the lattice plane pointing towards and away from the reader respectively. Black lines denote elastic connections between magnets. Particles in the unit cell have been highlighted by placing yellow dots in their centers.

the notation as its value is not important so $u_i, u_{i+n} \rightarrow u, u_n$, yielding:

$$u_n \approx u + hn\frac{\partial u}{\partial x} + \frac{1}{2}(hn)^2\frac{\partial^2 u}{\partial x^2} \tag{4.19}$$

For 1D lattices the unit cell volume V is:

$$V = hbw \tag{4.20}$$

where b and w are the thicknesses of the rectangular prism unit cell in the 2 directions perpendicular to the length of the lattice. Substituting Eq. (4.19) into Eq. (4.18) and dividing by the unit cell volume V simplifies to:

$$\frac{h^2}{V}\left[k + \sum_{n=1}^{\infty} k_n^{(m)} n^2\right]\frac{\partial^2 u}{\partial x^2} - \frac{m_p}{V}\ddot{u} = 0 \tag{4.21}$$

By comparing Eq. (4.21) to the 1D wave equation

$$E\frac{\partial^2 u}{\partial x^2} - \rho\ddot{u} = 0 \tag{4.22}$$

where ρ is the material density, it can be seen that the equivalent Young's modulus E is:

$$E = \frac{h^2}{V}\left[k + \sum_{n=1}^{\infty} k_n^{(m)} n^2\right] \tag{4.23}$$

Linearizing Eq. (2.5) it can be determined that:

$$k_n^{(m)} = 4\frac{\psi^{(m)}}{r_n^5}s^n = 4\frac{\psi^{(m)}}{n^5 h^5}s^n \tag{4.24}$$

where r_n is the distance from particle i to particle n and s is defined above.

4.3.1 Young's modulus for 2 particle cells

For convenience, the modulus of elasticity is normalized to the unmagnetized case ($\psi^{(m)} = 0$), E_o. If all magnets are repelling ($s = 1$) (Fig. 4.1(a)) the normalized modulus of elasticity is:

$$\frac{E}{E_o} = h_o\left[1 + 4\frac{\bar{\psi}^{(m)}}{h_o^5}\zeta(3)\right] \tag{4.25}$$

where $h_o = h/r_0$ and ζ is the Reimann zeta function defined as [96]:

$$\zeta(p) = \sum_{n=1}^{\infty}\frac{1}{n^p}. \tag{4.26}$$

Since there exist methods to accurately calculate the Reimann zeta function and it is computationally reasonable to achieve a value for it to machine precision the radius of influence r_∞ is not used in this case and no modeling error is introduced by omitting magnetic interactions in this 1D structure. Furthermore, the normalized magnetization is defined as in Eq. (2.18). If the polarity of the magnets alternates ($s = -1$) (Fig. 4.1b) the normalized modulus of elasticity is:

$$\frac{E}{E_o} = h_o\left[1 - 3\frac{\bar{\psi}^{(m)}}{h_o^5}\zeta(3)\right] \tag{4.27}$$

Now only h_o must still be defined. The distance between each particle h is a stable critical point of the energy functional Eq. (2.13) when reduced to its static terms. This leads to the following polynomial problem for nearest neighbors repelling and attracting respectively:

$$h_o^5 - h_o^4 - \bar{\psi}^{(m)}\zeta(3) = 0 \tag{4.28}$$

$$h_o^5 - h_o^4 + \frac{3}{4}\bar{\psi}^{(m)}\zeta(3) = 0 \tag{4.29}$$

The variation of the equivalent Young's modulus with $\bar{\psi}^{(m)}$ is presented in Fig. 4.3. The figure describes the tunability of the stiffness with changes in magnetization for simple structures defined by a 1 and 2 magnet unit cell. It is observed that the presence of repulsive magnetic interactions produces a hardening of the structure (solid black curve), and the presence of attractive nearest neighbor magnetic interactions has a softening effect (dashed red curve). There is a critical magnetization for the case with attracting nearest neighbors near $\bar{\psi}^{(m)} = 0.09$ where the structure approaches 0 stiffness as the structure becomes unstable. This is the magnetization magnitude at which the magnetic forces overpower the elastic forces from the axial springs. Beyond this point only reconfigured versions of the structure are stable.

4.3.2 Young's modulus for 4 particle cells

The larger a unit cell becomes, the more possible configurations there are. The 1D results in this paper only consider unit cells of up to 4 magnets for simplicity. Furthermore, not all possible magnetic polarity patterns are considered. The results from 4 magnet unit cells are now discussed, with 2 magnet unit cells considered as a special case of 4 magnet unit cells. The group of configurations considered here are those pictured in Figs. 4.1(b), 4.1(c), 4.1(d), 4.1(e), 4.1(f), and 4.1(g). The configurations in this group can reconfigure into any other configurations in the group, provided that both can exist for a given magnetization.

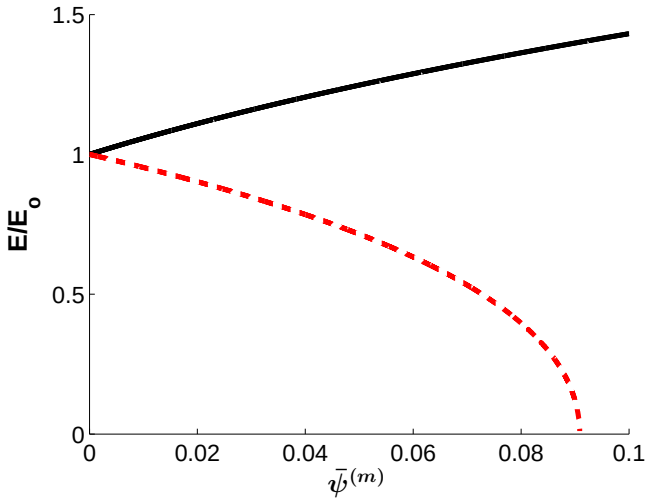

Figure 4.3: Exact analytical solution of normalized modulus of elasticity for: the structure pictured in Fig. 4.1a (black $-$) and the structure pictured in Fig. 4.1b (red $--$).

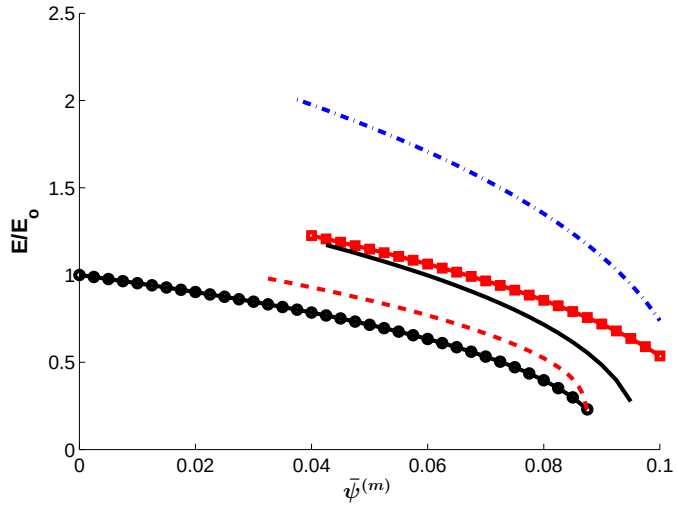

Figure 4.4: Normalized modulus of elasticity of structures with an even number of magnets per unit cell; configuration in Fig. 4.1b (black circles), configuration in Fig. 4.1c (red squares), configuration in Fig. 4.1e (red $--$), configuration in Fig. 4.1f (black $-$), configuration in Fig. 4.1g (blue $-\cdot$).

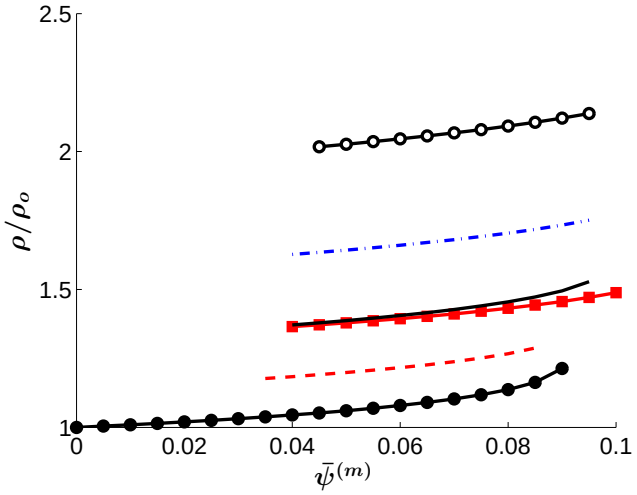

Figure 4.5: Normalized density of structures with an even number of magnets per unit cell; configuration in Fig. 4.1b (black circles), configuration in Fig. 4.1c (red squares), configuration in Fig. 4.1d (black rings), configuration in Fig. 4.1e (red $--$), configuration in Fig. 4.1f (black $-$), configuration in Fig. 4.1g (blue $-\cdot$).

Any structures that have contacting particles require a minimum magnetization to hold the particles in contact against the compressed spring's force. In addition, when a structure is magnetized highly enough certain configurations will not be possible as magnetic forces will overcome elastic forces. Therefore, there are values of $\bar{\psi}^{(m)}$ that do not permit all the configurations. For the following results a contact stiffness of $\alpha = 40$ and a contact distance of $r_c = 0.5r_0$ are used. The properties of the different configurations are shown in Figs. 4.4, and 4.5. For $\bar{\psi}^{(m)} \approx 0.045$ to 0.090 this single system can take any of the 6 studied configurations, which have different stiffnesses and densities. The modulus of elasticity E and density ρ are normalized by the modulus of elasticity and density calculated when $\bar{\psi}^{(m)} = 0$, which are E_o and ρ_o. Conveniently, the normalized density is the reciprocal of the normalized equilibrium unit cell width d, i.e. $d/d_0 = (\rho/\rho_o)^{-1}$, where d_0 is the equilibrium distance calculated when $\bar{\psi}^{(m)} = 0$. For the simplest cases, which are shown in Fig. 4.3, $d/d_0 = 2h/(2r_0) = h_o$.

The Young's modulus and its variation with $\bar{\psi}^{(m)}$ is presented in Fig. 4.4. Through reconfiguration alone there are as many values available as configurations. The structures

corresponding to Fig. 4.4 all soften in response to an increase of their magnetization. This is due to nearest neighbors that are in attraction, because the linearized model of attracting magnets exhibits negative axial stiffness. If both reconfiguration and changes in $\bar{\psi}^{(m)}$ are considered there is no stiffness between the values of $E/E_o \approx 0.2$ and 2 that cannot be achieved by at least one configuration, and there are some stiffnesses which can be achieved by as many as 4 configurations. This shows that stiffness adaptation is not limited to a few discrete values, allowing easier integration into possible design applications. The structure pictured in Fig. 4.1(d) is shown separately in Fig. 4.7 because its stiffness is much greater than the other structures' as the contact stiffness used is $\alpha = 40$. The structure is not a full 40 times stiffer though because the attractive magnetic interactions soften the structure, even under the minimum magnetization required for it to exist. Having only contact interactions, the structure in Fig. 4.1(d) is the stiffest possible configuration for a structure with alternating magnetic poles and the parameters considered here, and thus gives an upper bound. The same can be said for the density, as contacting particles provides the closest packed structure.

The densities of the 2 and 4 magnet configurations are presented in Fig. 4.5. The density is primarily effected by the configuration, but there is some change with $\bar{\psi}^{(m)}$. The density can be approximately doubled through reconfiguration. The configurations pictured in Fig. 4.1(c) and Fig. 4.1(f) exhibit similar densities because both have the same ratio of contacting to non-contacting magnets.

The configurations pictured in Fig. 4.1(c) and Fig. 4.1(f) are worthy of note because they would be considered equivalent in terms of E and ρ if only nearest neighbor interactions were considered. In fact, for low enough $\bar{\psi}^{(m)}$ they have almost equivalent properties. But with higher values of $\bar{\psi}^{(m)}$ their dissimilar properties show that non-nearest-neighbor interactions have a significant effect. Even so, the density does not change significantly with increasing $\bar{\psi}^{(m)}$, which means that a structure can have little change in its global size but a significant change in its stiffness by changing only its internal configuration. For

example, if $\bar{\psi}^{(m)} = 0.09$ reconfiguring from the configuration in Fig. 4.1(c) to the one in Fig. 4.1(f) would produce only a 2.7% increase in density, but a 33% decrease in stiffness.

4.3.3 Numerical simulations

For the purpose of validating the homogenization method, as applied to the magneto-elastic lattices, numerical simulations are completed. The equations of motion are integrated using an explicit, variable-step Runge-Kutta method to obtain the time history of the positions of the particles in a finite lattice. This provides a framework for performing numerical experiments. A finite sample of each configuration to be validated, 40 particles long, is compressed quasi-statically over a strain of less than 0.001, in which the structure can be considered linear. The compression is performed through an applied displacement of one end of the system while the other end is held fixed. There is linear damping included to damp out vibrations, so slow enough forcing will ensure that dynamic forces are negligible. To obtain a strain rate slow enough to consider quasi-static a convergence study is performed. The force vs. displacement information is used to calculate a stiffness simply by comparing the change in reaction force to the structure's axial strain. By normalizing to the case when $\bar{\psi}^{(m)} = 0$ the simulation results can be compared with the homogenization results directly. Their comparison is shown in Figs. 4.6 and 4.7, with curves representing the approximate analytical results and the shapes representing the numerical results.

4.4 Homogenization of 2D magneto-elastic lattices

For simplicity the results presented for 2D magneto-elastic structures are restricted to systems described by a 2 magnet unit cell. A magnetization pattern where all magnets repel (Fig. 4.2(a)) is used to investigate and compare to the pattern where nearest neighbors attract (Fig. 4.2(b)). The magnetization pattern with attracting nearest neighbors is used to showcase the drastic changes in properties that can be achieved by reconfiguration. The reconfiguration considered is the transition to the re-entrant lattice (Fig. 4.2(c)) as this

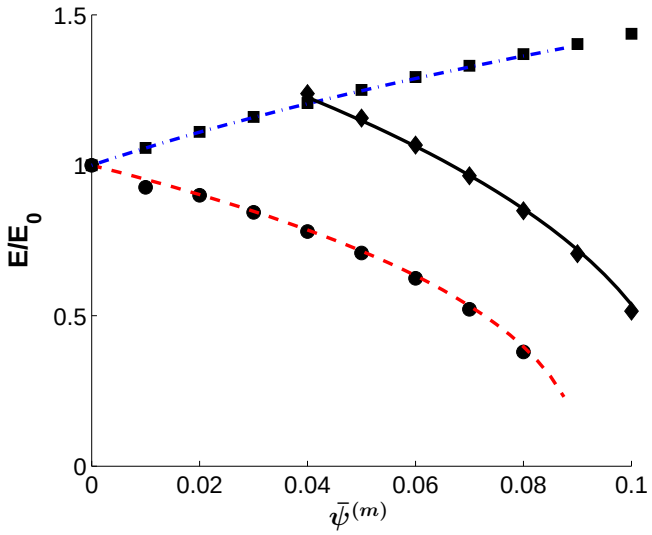

Figure 4.6: Comparison between normalized modulus of elasticity calculated by homogenization and numerical simulation for the configuration in Fig. 4.1a (blue $-\cdot$ and black squares respectively), the configuration in Fig. 4.1b (red $--$ and black circles respectively), and the configuration in Fig. 4.1c (black $-$ and black diamonds respectively).

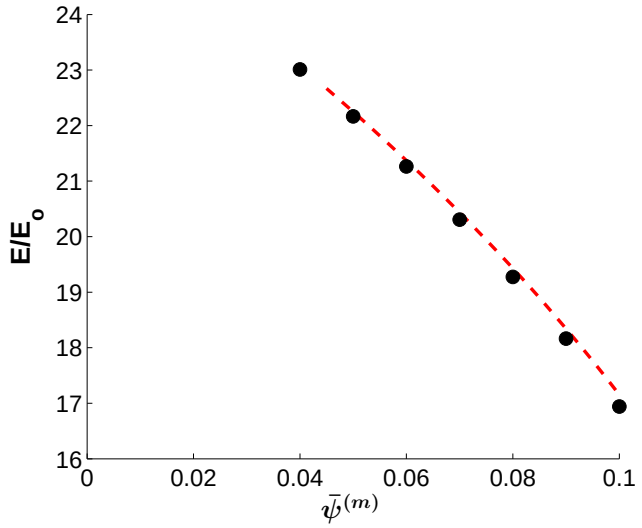

Figure 4.7: Comparison between normalized modulus of elasticity calculated by homogenization and numerical simulation for the configuration in Fig. 4.1d (red $--$ and black circles respectively).

is possibly the easiest way to reconfigure the magneto-elastic hexagonal lattice studied. In contrast with the hexagonal patterns, the re-entrant lattice is anisotropic. Fig. 4.10(a) defines the 1 and 2 directions for the re-entrant lattice, which are used to identify the orthotropic properties. Furthermore, the re-entrant lattice cannot exist for all the same values of $k_\tau/k_{\tau o}$ and $\bar{\psi}^{(m)}$ as the hexagonal lattice. Namely, there is an upper limit on $k_\tau/k_{\tau o}$ near 0.1. To explore the tunability of the equivalent mechanical properties of the aforesaid lattices the homogenization procedure as described in Section 4.2 is applied to structures with varying torsional stiffnesses k_τ and magnetization magnitudes $\bar{\psi}^{(m)}$. As in the previous section a contact stiffness of $\alpha = 40$ and a contact distance of $r_c = 0.5r_0$ are used. The properties are normalized with respect to a reference case defining the reference properties E_o and G_o, which is the unmagnetized ($\bar{\psi}^{(m)} = 0$) hexagonal lattice with $k_{\tau o} = 1\ \mathrm{N/rad}$ and $k_{ao} = 1\ \mathrm{N/m}$.

The first results presented are for the two considered hexagonal lattice structures (Figs. 4.2(a) and (b)). The homogenization produces properties that describe an isotropic material, i.e. $E_1 = E_2 = E$, $\nu_{12} = \nu_{21} = \nu$, and $G_{12} = E/(2(1+\nu)) = G$, which is to be expected for regular hexagonal geometry [2]. Variation in k_τ is seen to cause substantial changes in material stiffness so the value of k_τ is incremented exponentially. Indeed, as $k_\tau \to 0$ the quantities $E, G \to 0$ and the lattice approaches a mechanism. In this state the structure's global deformation is dominated by the rotational deformation of the torsional springs. In such a case magnetization has a stiffening effect on the structure, which is evident in Figs. 4.8(a-d) for the cases where $k_\tau/k_{\tau o} = 10^{-3}$ (solid black line), though it is more prominent in the lattice with only repelling magnetic interactions. The stiffening of the structure can be explained predominantly through the repulsion of the next-nearest neighbor interactions, which are repulsive in both of the lattices discussed here. As the lattices are dominated by rotational deformation, the nearest neighbor magnetic interactions do not significantly effect the global properties. The exception comes when the the effective axial stiffness is nearly 0 close to the point of instability for attracting nearest neighbors,

e.g. near $\bar{\psi}^{(m)} = 0.1$. Though next-nearest neighbor interactions can explain the dominant trend for both magnetization patterns, comparison of Fig. 4.8(a) and (b) reveals that more distant magnetic interactions have an non-negligible effect on the structure. Thus, efforts to include the non-nearest neighbor interactions appear to be valuable. Significant tunability is seen for low k_τ when the magnetic interactions dominate the structure's properties. For example, in the case where $k_\tau/k_{\tau o} = 10^{-3}$ in Fig. 4.8(a) E increases by a factor of 48 over the range of $\bar{\psi}^{(m)}$ shown.

Increasing k_τ causes the global deformation of the lattice to be dominated by the deformation of the axial springs in the lattice. In the limit as $k_\tau \to \infty$ the structure will become like the one discussed in [97]. The axial deformation dominated structures are stiffened by repulsive nearest neighbor interactions and softened by attractive nearest neighbor interactions, due to the equivalent linearized axial stiffness of magnetic interactions being positive for repulsion and negative for attraction. The greatest torsional stiffness shown is $k_\tau/k_{\tau o} = 10^2$ (dashed red line). Increasing $k_\tau/k_{\tau o}$ above this does not have a significant effect on the mechanical properties. In addition, decreasing the torsional stiffness below $k_\tau/k_{\tau o} = 10^{-3}$ does not make a significant change. Therefore, the properties of the hexagonal lattices discussed are bounded by the solid black and red dashed curves in Fig. 4.8.

An interesting property of both magnetization patterns is that the Poisson's ratio can be either positive or negative depending on the torsional stiffness k_τ and the magnetization (Figs. 4.8(e) and (f)). In the limit as $k_\tau \to 0$, when the compliance of the system is dominated by the torsional springs, it is observed that $\nu \to 1$, as expected for the analogous structure of the regular hexagonal honeycomb with slender beams [2]. In the limit as $k_\tau \to \infty$ it is observed that $\nu \to -1/3$, which is consistent with equations given by [97] for regular hexagonal lattices with the angles between bars constrained. In this second case the structure's compliance is dominated by the axial springs. Thus, it is clear that the ratio between rotational and axial stiffness affects the sign of ν. Since magnetization can have a similar effect to changing the rotational stiffness, as discussed above, for proper values of

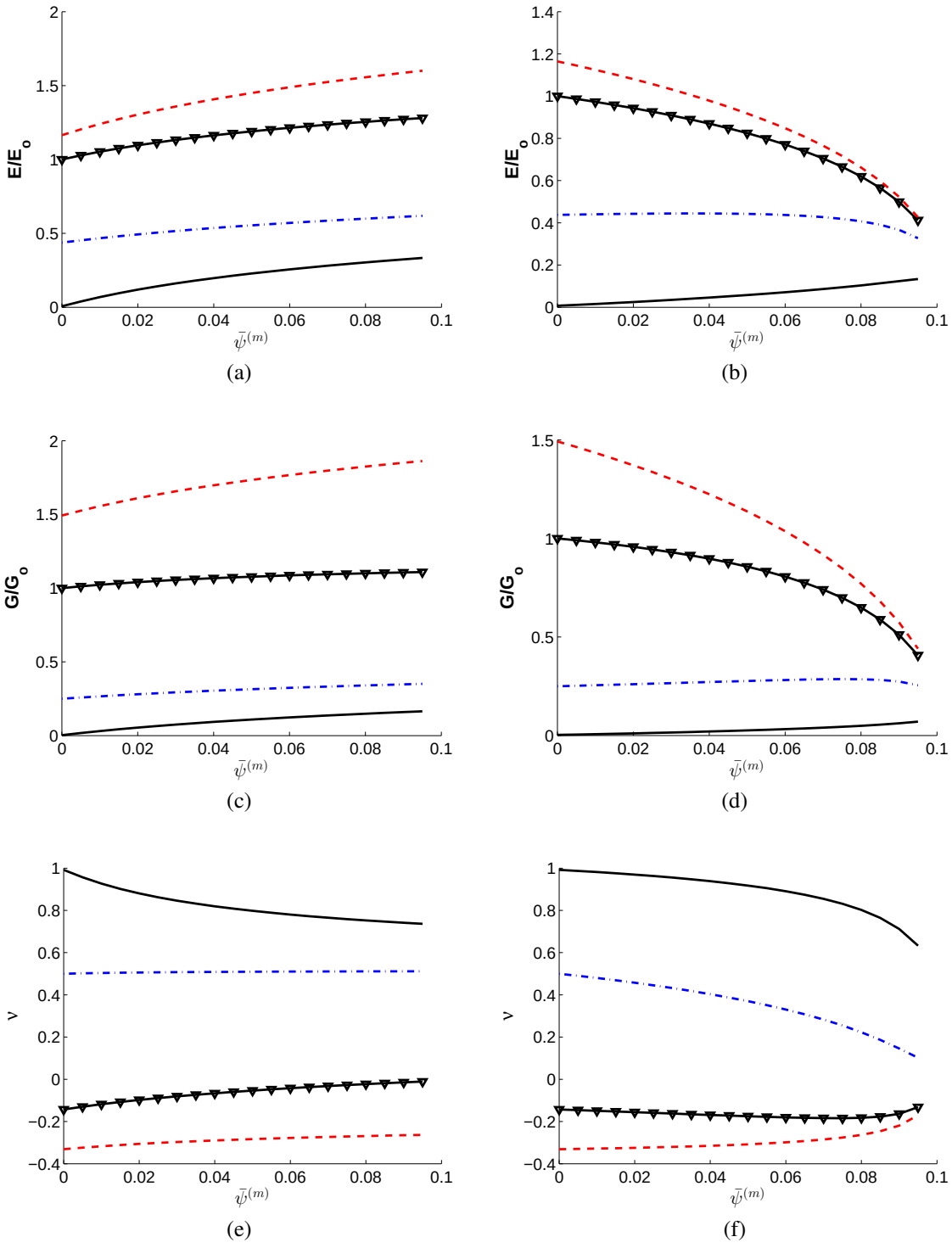

Figure 4.8: Normalized moduli and Poisson's ratio for the hexagonal lattice with repelling magnets (a, c, and e) and with attracting nearest neighbors (b, d, and f). $k_\tau/k_{\tau o} = 10^2$ (red $--$), $k_\tau/k_{\tau o} = 10^0$ (black triangles), $k_\tau/k_{\tau o} = 10^{-1}$ (blue $-\cdot$), and $k_\tau/k_{\tau o} = 10^{-3}$ (black $-$).

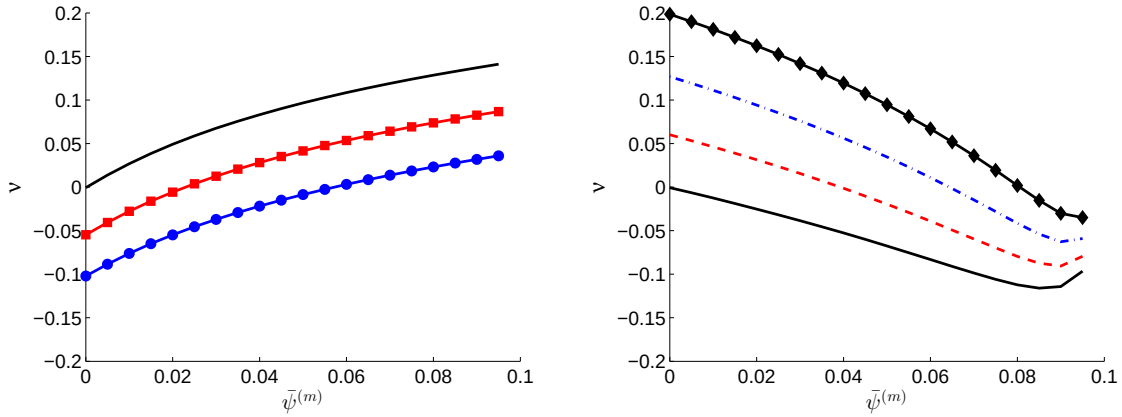

(a) (b)

Figure 4.9: Poisson's ratio for the hexagonal lattice with repelling magnets (a) and with attracting nearest neighbors (b) for values of k_τ that allow changes in $\bar{\psi}^{(m)}$ to change the sign of ν. $k_\tau/k_{\tau o} = 10^{-0.1}$ (blue circles), $k_\tau/k_{\tau o} = 10^{-0.2}$ (red squares), $k_\tau/k_{\tau o} = 10^{-0.3}$ (black $-$), $k_\tau/k_{\tau o} = 10^{-0.4}$ (red $--$), $k_\tau/k_{\tau o} = 10^{-0.5}$ (blue $-\cdot$), and $k_\tau/k_{\tau o} = 10^{-0.6}$ (black diamonds).

k_τ it is possible to switch between positive and negative ν simply by changing $\bar{\psi}^{(m)}$. The ranges of k_τ that allow for such tunability of ν for both magnetization patterns discussed are shown in Fig. 4.9.

As stated previously the magneto-elastic hexagonal lattice with attracting nearest neighbors can be reconfigured into the re-entrant lattice (Fig. 4.2(c)) where strong contact forces hold the structure in equilibrium against magnetic attraction. The homogenized properties for varying values of $k_\tau/k_{\tau o}$ and $\bar{\psi}^{(m)}$ are presented in Fig. 4.11 and they are compared to the hexagonal lattices that reconfigure into them. In contrast to analyses of re-entrant lattices such as those by [2] or [50], where the geometry of a cell is explicitly defined, the re-entrant lattices discussed in this article have their geometry defined by the equilibrium configuration associated with a chosen value of $\bar{\psi}^{(m)}$. The equilibrium length of one axial spring relative to another may differ by more than 10% depending on the choice of $k_\tau/k_{\tau o}$ and $\bar{\psi}^{(m)}$, but the equilibrium lengths are approximately equal for low $k_\tau/k_{\tau o}$ and $\bar{\psi}^{(m)}$. Therefore, the tuning of properties with changing $\bar{\psi}^{(m)}$ discussed hereafter are caused in part by the change in the re-entrant lattice equilibrium geometry.

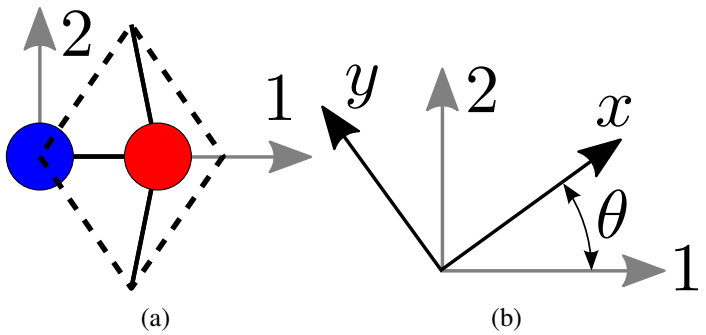

Figure 4.10: Re-entrant unit cell with coordinate system 1,2 pictured (a), and θ defined as the angle between coordinate axes 1,2 and x, y (b)

Reconfiguration from the hexagonal to the re-entrant lattice has a drastic effect on the stiffness of the lattice. The drastic change is seen comparing in Fig. 4.11 and Fig. 4.8(b, d, and f). Two choices of $k_\tau/k_{\tau o}$ are used. The value $k_\tau/k_{\tau o} = 10^{-1}$ is near the maximum value of $k_\tau/k_{\tau o}$ for which the re-entrant lattice can exist, and the value $k_\tau/k_{\tau o} = 10^{-3}$ is representative of the asymptotic solution as $k_\tau/k_{\tau o} \to 0$. Values for E_1 and E_2 (Fig. 4.11(a) and (b)) in the re-entrant lattices are generally much higher than E in hexagonal lattices of equal $k_\tau/k_{\tau o}$. The internal structure of the re-entrant lattice makes strain along the 1 and 2 directions produce axially dominant local deformation, regardless of the torsional stiffness. Furthermore, the stiff contact interactions make E_1 stiffer than values of E associated with axial deformation dominant hexagonal lattices with the same $\bar{\psi}^{(m)}$ and magnetization pattern. In the 2 direction, the increased density from the reconfiguration makes values of E_2 stiffer than associated values of E for axial deformation dominant hexagonal lattices. For the $k_\tau/k_{\tau o} = 10^{-3}$ case the Young's moduli of the hexagonal configuration are dominated by magnetic interactions, so since the minimum magnetization for the existence of the re-entrant configuration is low in this case the Young's moduli can be increased by more than 2 orders of magnitude simply through structural reconfiguration to the re-entrant lattice. Even for higher magnetizations there is over a 10-fold increase in stiffness due to reconfiguration. For $k_\tau/k_{\tau o} = 10^{-1}$ the structure is still significantly stiffened by reconfiguration, but not as drastically as in the previous case. The $k_\tau/k_{\tau o} = 10^{-1}$ also has a more limited

range of $\bar{\psi}^{(m)}$ in which it can exist in the re-entrant configuration.

As in the hexagonal lattice the shear modulus G_{12} in the re-entrant lattice is dependent on k_τ. When $k_\tau/k_{\tau o} = 10^{-3}$ reconfiguration can account for over order of magnitude increase in G_{12}, but when $k_\tau/k_{\tau o} = 10^{-1}$ the shear moduli for the hex and re-entrant lattices are more comparable. The Poisson's ratios also change significantly with reconfiguration, with the re-entrant lattices exhibiting lower Poisson's ratios than corresponding hexagonal lattices in general. Although the re-entrant lattice structure is generally known for being auxetic [2] this magneto-elastic example has positive ν_{12} and ν_{21} because of the stiff contact interactions that prevent the structure from folding in on itself. However, sufficiently soft contact interactions do allow negative ν_{12} and ν_{21}.

In the re-entrant lattice the shear moduli are small compared to the axial stiffnesses, and this produces significant variation of stiffness with respect to direction. Figure 4.12 shows the variation of the equivalent properties in the x, y coordinate system, which is redefined here to be oriented by θ with respect to the nominal coordinate system 1,2 as defined in Fig. 4.10(b). The properties of a re-entrant lattice (solid black line) with $k_\tau/k_{\tau o} < 10^{-1.5}$ is compared to its hexagonal configuration (dashed blue line). Note that the radii of the polar plots in Figs. 4.12(a-c) are logarithmic. It is evident that the re-entrant lattice is much softer for $\theta = 45$ degrees (Fig. 4.12(a) and (b) solid black line) than $\theta = 0$ degrees, becoming over half an order of magnitude softer. As the Young's moduli soften with changing θ the shear modulus stiffens by almost one order of magnitude (Fig. 4.12(c)). Simultaneously, there are substantial changes in the Poisson's ratios, though they remain positive. So, even when E_1 and E_2 are nearly equal the re-entrant lattice is far from isotropic in contrast to the hexagonal lattice.

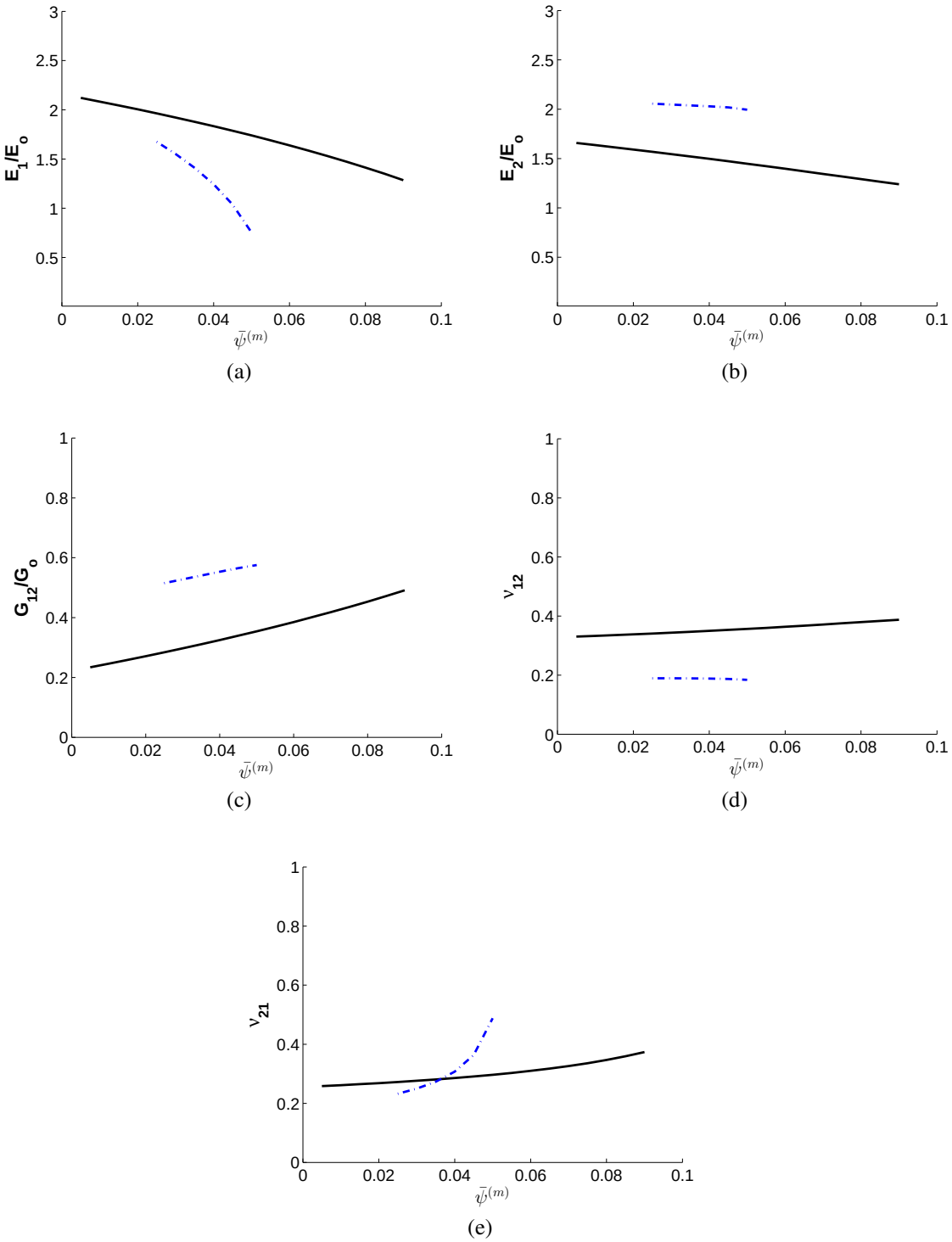

Figure 4.11: Normalized equivalent orthotropic properties for the re-entrant lattice with $\alpha = 40$ and $k_\tau/k_{\tau o} = 10^{-1}$ (blue $\cdot-$), and $k_\tau/k_{\tau o} = 10^{-3}$ (black $-$).

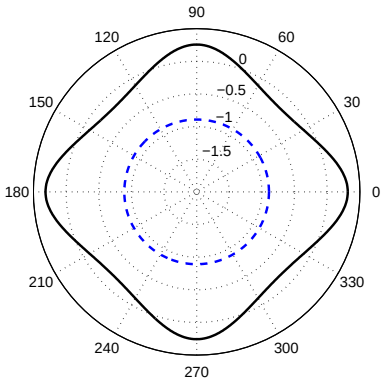

(a) $\log_{10}(E_x/E_o)$

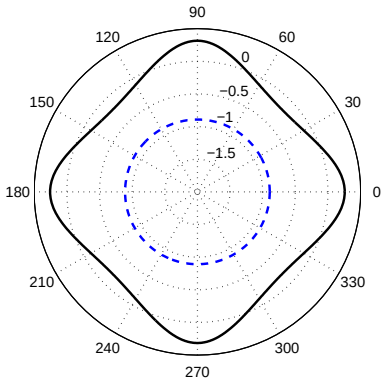

(b) $\log_{10}(E_y/E_o)$

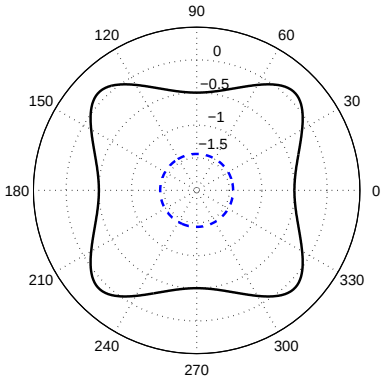

(c) $\log_{10}(G_{xy}/G_o)$

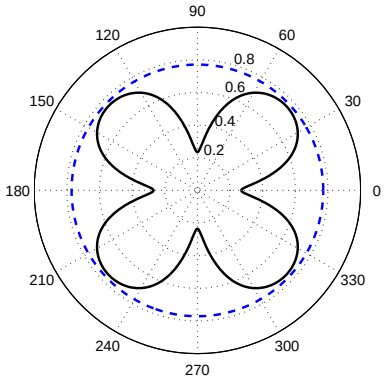

(d) ν_{xy}

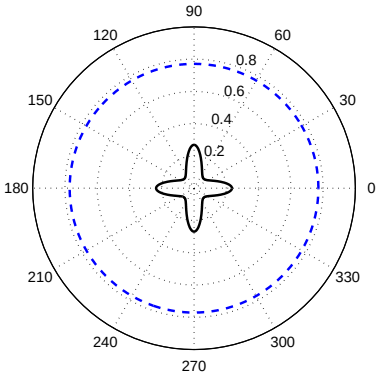

(e) ν_{yx}

Figure 4.12: Variation of mechanical properties with coordinate axis orientation θ of the hexagonal (blue $--$) and re-entrant lattice (black $-$) with $k_\tau/k_{\tau o} = 10^{-1.5}$, $\bar{\psi}^{(m)} = 0.01$, $\alpha = 40$.

CHAPTER 5
TOPOLOGICALLY PROTECTED BOUNDARY MODES

5.1 Chapter overview

This chapter aims to develop a framework for designing lattices which support propagation of topologically protected helical edge states in mechanical systems. The approach for converting from quantum-mechanical to mechanical lattices presented by Süsstrunk and Huber [74] for square lattices is extended to general planar lattices in a simple and systematic way, thereby developing a family of mechanical lattices. First the applied theoretical approach is described. Next, the lattices used to illustrate the effectiveness of the approach are described, which include a hexagonal and Lieb lattice. Finally, the results are presented for both lattices, showing the existence of helical edge modes of mechanical wave propagation with analytical band diagrams and transient numerical simulations.

5.2 Theory: from quantum to classical mechanical systems

Quantum mechanical systems exhibiting topologically protected edge states are governed by the eigenvalue problem that arises from the Schrödinger equation, but in mechanical systems it arises from Newton's laws of motion. In both cases creating a lattice exhibiting TPBMs relies on the existence of two overlapping pairs of Dirac cones in the dispersion relations, which may be separated to form a topologically nontrivial bandgap introducing so-called spin-orbital coupling [57]. The attributes of a quantum mechanical system with helical edge states are discussed first, and then its mechanical analogue is derived.

Let $\boldsymbol{H}$ be the tight-binding Hamiltonian of the quantum system for a lattice with up and down spin electrons denoted by subscript μ which takes values in $\{-1, 1\}$. A lattice with only nearest neighbor interactions and spin orbital coupling as those in [98] are considered.,

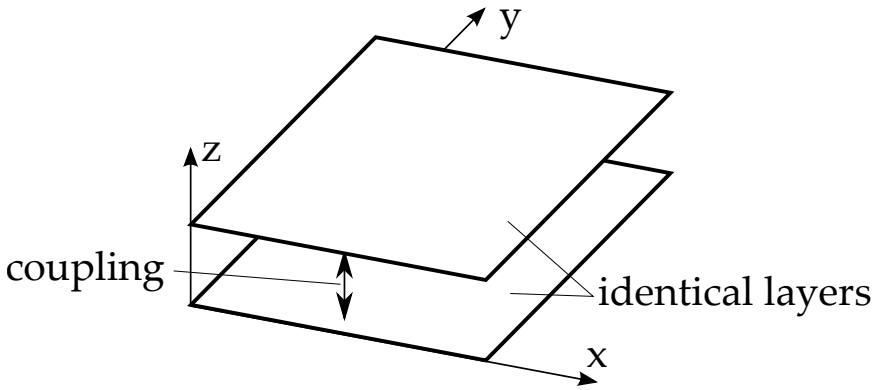

Figure 5.1: Schematic of bi-layered lattice, made of two identical layers, with interlayer coupling between them.

with their interaction strengths denoted by k_{nn} and λ_{iso}, respectively. Let $\boldsymbol{d}_{pq}$ denote the vector connecting two lattice sites (p, q). Let $\boldsymbol{n}_{pq} = \boldsymbol{d}_{pr} \times \boldsymbol{d}_{rq}/|\boldsymbol{d}_{pr} \times \boldsymbol{d}_{rq}|$ denote the unit vector in terms of the bond vectors which connect next nearest neighbor lattice sites p and q via the unique intermediate site r. Let $\sigma_p, p \in \{x, y, z\}$ denote the set of Pauli matrices and let $\boldsymbol{e}_z$ denote the unit normal vector in the $z-$direction. Following the second neighbor tight binding model [57] and assuming that our lattice is located in the xy plane, the Hamiltonian for this planar lattice can then be expressed in the form

$$\boldsymbol{H} = -k_{nn} \sum_{\langle pq \rangle;\mu} \hat{s}^{\dagger}_{p,\mu} \hat{s}_{q,\mu} - i\lambda_{iso} \sum_{\langle\langle pq \rangle\rangle;\mu} (\boldsymbol{n}_{pq} \cdot \boldsymbol{e}_z) \sigma_{z,\mu\mu} \hat{s}^{\dagger}_{p,\mu} \hat{s}_{q,\mu} \tag{5.1}$$

Here $\hat{s}_p$ and $\hat{s}^{\dagger}_p$ denote the standard creation and annihilation operators, respectively, and $\sigma_{z,\mu\mu}$ equals the value of μ. The notation $\langle pq \rangle$ denotes nearest neighbor pairs of p and q, and the notation $\langle\langle pq \rangle\rangle$ denotes next-nearest neighbors. The eigenvalue problem arising from the above Hamiltonian has helical edge modes for a range of values of λ_{iso} and k_{nn}.

We now describe the procedure to get a mechanical analogue of the above system. In the mechanical system, the stiffness matrix comprises of real terms for forces arising from passive components and the eigenvalue problem arises from applying a traveling wave assumption to Newton's laws. Noting that unitary transformations preserve the eigenvalues and thus the topological properties of the band structures, we apply the following unitary

transformation [74] to the quantum eigenvalue problem towards obtaining a corresponding Hamiltonian with the desired properties in a mechanical system:

$$\boldsymbol{U} = u \otimes \mathbb{1}_N, \quad u = \frac{1}{\sqrt{2}} \begin{pmatrix} 1 & -i \\ 1 & i \end{pmatrix} \tag{5.2}$$

where N is the number of sites in the lattice. Under this unitary transformation, the mechanical Hamiltonian, is obtained by $\boldsymbol{D}_H = \boldsymbol{U}^\dagger \boldsymbol{H} \boldsymbol{U}$. Noting that $u^\dagger \sigma_z u = i\sigma_y$ and $u^\dagger u = \mathbb{1}_2$, the mechanical Hamiltonian has the following expression:

$$\boldsymbol{D}_H = -k_{nn} \sum_{\langle pq \rangle;\mu} \hat{s}^\dagger_{p,\mu} \hat{s}_{q,\mu} - \lambda_{iso} \sum_{\langle\langle pq \rangle\rangle;\mu} \mu(\boldsymbol{n}_{pq} \cdot \boldsymbol{e}_z) s^\dagger_{p,\mu} s_{q,-\mu} \tag{5.3}$$

As required, this equivalent Hamiltonian $\boldsymbol{D}$ has only real terms and it should arise from the eigenvalue problem of a mechanical system.

Similar to the quantum Hamiltonian, the band structure of the dynamical matrix of the corresponding mechanical system requires two overlapping bands, with a bulk band gap between them which breaks the Dirac cones and this band gap arises due to the λ_{iso} coupling. The two overlapping bands are obtained by simply having two identical lattices stacked on top of each other, as illustrated in the schematic in Fig. 5.1. There are masses at the sites. The two lattices have nearest neighbor coupling springs k_{nn} in their respective planes and springs with strength λ_{iso} between the next nearest neighbor sites in the other plane. When $\lambda_{iso} = 0$, the two lattice layers are uncoupled and the band structure for each layer has two Dirac cones in the first Brillouin zone. The couplings introduced by λ_{iso} are inter-layer and connect all next nearest neighbors at the lattice site. In the presence of couplings between the two lattice layers, the Dirac cones are broken, but the bands still overlap. The band structure is now topologically nontrivial and supports edge states similar to the quantum mechanical system.

Assuming the springs in the lattice to follow a linear force displacement law, Newton's

law for displacement $\boldsymbol{u}$ at the lattice site $\boldsymbol{x}$ takes the form $\boldsymbol{M}\ddot{\boldsymbol{u}} + \boldsymbol{K}\boldsymbol{u} = \boldsymbol{0}$. Imposing a harmonic solution with frequency ω of the form $\boldsymbol{u}(t) = \boldsymbol{v}e^{i\omega t}$ results in the eigenvalue problem $\boldsymbol{D}\boldsymbol{v} = \omega^2\boldsymbol{v}$, where $\boldsymbol{D} = \boldsymbol{M}^{-1}\boldsymbol{K}$ is the dynamical matrix. The band structure for an infinite lattice is obtained by imposing the Bloch representation $\boldsymbol{v}(\boldsymbol{x}) = \boldsymbol{v}_0 e^{i\boldsymbol{\kappa}\cdot\boldsymbol{x}}$, where $\boldsymbol{v}_0$ represents the degrees of freedom in a unit cell of the lattice. The eigenvalues of the dynamical matrix ω^2 are positive, in contrast with the eigenvalues of the mechanical Hamiltonian $\boldsymbol{D}_H$. To have edge modes in the mechanical system with dynamical matrix $\boldsymbol{D}$, we require that its band structure be identical to that of $\boldsymbol{D}_H$. This condition is achieved by translating the bands of $\boldsymbol{D}_H$ upward along the frequency axis, so they are all positive. Adding a term $\boldsymbol{D}_0 = \eta\mathbb{1}_{2N}$ $(\eta > 0)$ to $\boldsymbol{D}_H$ shifts the bands upward and imposing the condition $\boldsymbol{D} = \boldsymbol{D}_H + \boldsymbol{D}_0$ results in identical band structures. Note that adding the term $\boldsymbol{D}_0$ keeps the eigenvectors unchanged while adding a constant term η to all the eigenvalues, and thus it does not alter the topological properties of the bands. Let n_p and m_p denote the number of nearest and next-nearest neighbors at a site p. Then we have the following expression for $\boldsymbol{D}_0$

$$\boldsymbol{D}_0 = \sum_{p;\mu} \eta \hat{s}^{\dagger}_{p,\mu}\hat{s}_{p,\mu}, \quad \eta = \max_p \left(k_{nn}m_p + \lambda_{iso}n_p\right). \tag{5.4}$$

In a mechanical system, the stiffness $k_{pp} = k_{nn}m_p + \lambda_{iso}n_p$ arises at lattice site p when there are springs connecting two lattice sites. The dynamical matrix as a result is diagonally dominant and the term $\boldsymbol{D}_0$ arises naturally as a result of spring interactions. Any additional stiffness required at a lattice site p can be achieved by adding a ground spring stiffness equal to the difference between η and k_{pp}. We will demonstrate in the next section that topological phase transitions can arise if the ground spring stiffness deviates from this value.

(a) (b)

Figure 5.2: Schematic of (a) normal and (b) reverse springs. A clockwise rotation in one disk induces a clockwise (counter-clockwise) torque on the other from the normal (reverse) spring.

5.3 Mechanical lattice description

Having presented the structure of a dynamical matrix $\boldsymbol{D}$ for realizing edge modes, we now outline the procedure to construct a mechanical lattice using fundamental building blocks, which are disks and two types of linear springs here called: "normal" and "reversed." There is a disk at each lattice site, which can rotate about its center in the $\boldsymbol{e}_z$ direction as its single degree of freedom. It has a rotational inertia I and radius R, and the mass of the springs relative to the disks are assumed to be negligible. The disks interact with each other by a combination of these normal and reversed springs. Figure 5.2(a) displays a schematic of the normal spring, composed of a linear axial spring of stiffness k_N connecting the edges of disks (i, j). Figure 5.2(b) displays a schematic of a reversed spring, an axial spring joining opposite sides of a disk. For small angular displacements θ_i, θ_j the torque exerted on disk i due to the normal and reversed springs are $k_N R^2(\theta_j - \theta_i)$ and $k_R R^2(-\theta_j - \theta_i)$, respectively. The aforementioned torque-displacement relations remain a reasonable approximation when the inter-layer springs are nearly parallel to the lattice, which is assumed. Otherwise, a scale factor can be added.

We present the explicit construction of two lattice configurations: the hexagonal and the Lieb lattice. Figure 5.3(a) displays the schematic of a cell of the hexagonal lattice. It is

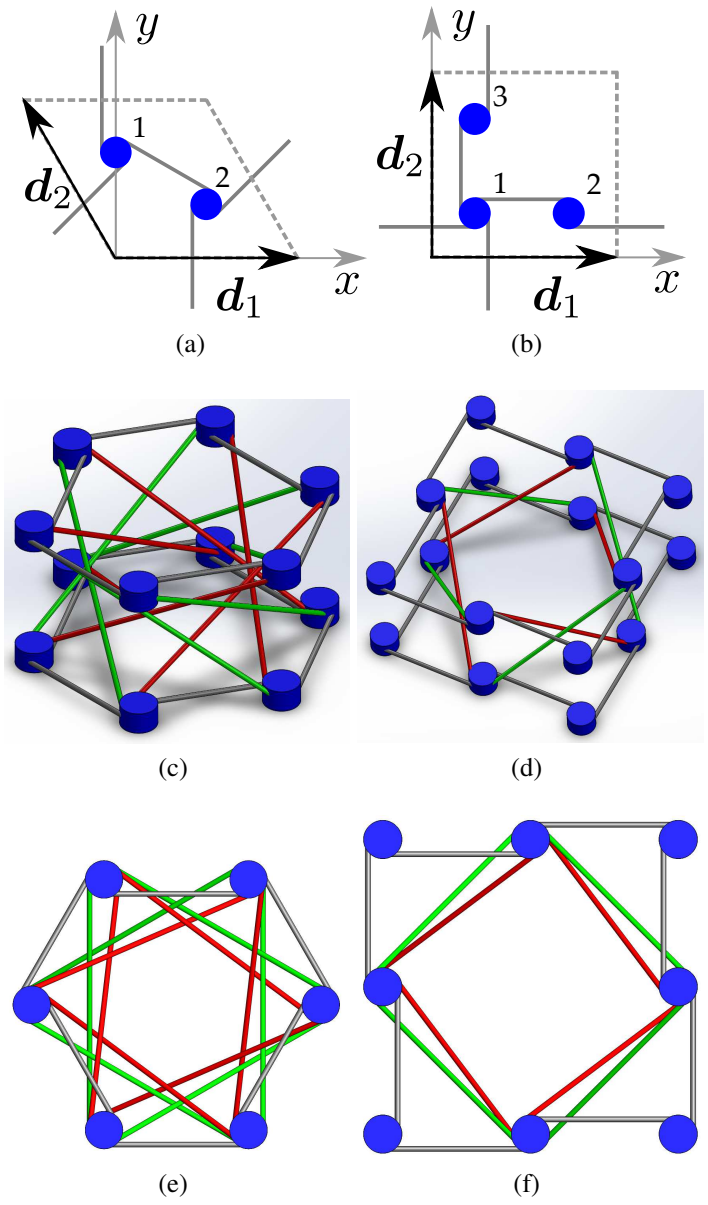

Figure 5.3: Hexagonal and Lieb lattice respectively (a,b) unit cell defined by the lattice vectors $\boldsymbol{d}_1$ and $\boldsymbol{d}_2$ with nearest-neighbor interactions in gray, (c,d) trimetric view, and (e,f) top view. (c-f) Bars represent axial springs and the only DOF of each blue cylinder is rotation about its longitudinal axis. Gray bars act within one layer. Red and green bars couple the layers.

composed of two layers of disks, with the disks on the top and bottom layer analogous to the up and down spin electrons at each site in a quantum mechanical system. The arrangement of couplings is chosen to achieve the desired form of $\boldsymbol{D}$, with normal in-plane springs (gray color) of stiffness k_{nn}/R^2 between nearest neighbors. There are two sets of interlayer springs between the next-nearest neighbors, normal springs (green) and reversed springs (red), both having stiffness k_{iso}/R^2. The inter-layer spring between two sites (p, μ) and $(q, -\mu)$ is of normal or reversed type depending on the sign of $\mu(\boldsymbol{n}_{pq} \cdot \boldsymbol{e}_z)$ in Eqn. (5.3). Figure 5.3 displays a schematic of the Lieb lattice. Note that the Lieb lattice also requires some normal springs connected to the rigid ground due to the mismatch between η and k_{pp}. In order to practically implement the described mechanical systems a fixture is required to constrain the translation and undesired rotation of the disks. One can envision a stiff plate or truss above and below the lattice with rods connecting the two through the disks. As long as the fixture is designed with higher frequency wave modes than the bi-layered lattice it should not interfere with the desired TPBMs.

We present the complete equations of motion for the disks in a unit cell for both the lattices considered in this work in the following subsections. Consider an infinite lattice divided into unit cells, and each unit cell is indexed by a pair of integers (i, j), denoting its location with respect to a fixed coordinate system. Let I be the rotational inertia of each disk and let $\theta_{i,j}^{a,b}$ denote the angular displacement of a disk. The two subscripts (i, j) identify the unit cell and and the two super-scripts identify the location of the disk within the unit cell (i, j). The first super-script index denotes its location in the xy-plane while the second super-script index denotes whether the disk is in top (t) or bottom (b) layer.

5.3.1 Hexagonal lattice

Figure 5.3(a) displays the top layer of a unit cell of the hexagonal lattice. Each layer has two disks, indexed as illustrated. The equations of motion of the four disks of the unit cell

are

$$I\ddot{\theta}^{1,t}_{i,j} = k_{nn}\left(\theta^{2,t}_{i,j} + \theta^{2,t}_{i,j-1} + \theta^{2,t}_{i-1,j} - 3\theta^{1,t}_{i,j}\right) - 6k_{iso}\theta^{1,t}_{i,j} + k_{iso}\left(\theta^{1,b}_{i+1,j} + \theta^{1,b}_{i-1,j+1} + \theta^{1,b}_{i,j-1}\right) - k_{iso}\left(\theta^{1,b}_{i,j+1} + \theta^{1,b}_{i-1,j} + \theta^{1,b}_{i+1,j-1}\right) \quad (5.5a)$$

$$I\ddot{\theta}^{2,t}_{i,j} = k_{nn}\left(\theta^{1,t}_{i,j} + \theta^{1,t}_{i,j+1} + \theta^{1,t}_{i+1,j} - 3\theta^{2,t}_{i,j}\right) - 6k_{iso}\theta^{2,t}_{i,j} + k_{iso}\left(\theta^{2,b}_{i,j+1} + \theta^{2,b}_{i-1,j} + \theta^{2,b}_{i+1,j-1}\right) - k_{iso}\left(\theta^{2,b}_{i+1,j} + \theta^{2,b}_{i-1,j+1} + \theta^{2,b}_{i,j-1}\right) \quad (5.5b)$$

$$I\ddot{\theta}^{1,b}_{i,j} = k_{nn}\left(\theta^{2,b}_{i,j} + \theta^{2,b}_{i,j-1} + \theta^{2,b}_{i-1,j} - 3\theta^{1,b}_{i,j}\right) - 6k_{iso}\theta^{1,b}_{i,j} + k_{iso}\left(\theta^{1,t}_{i+1,j} + \theta^{1,t}_{i-1,j+1} + \theta^{1,t}_{i,j-1}\right) - k_{iso}\left(\theta^{1,t}_{i,j+1} + \theta^{1,t}_{i-1,j} + \theta^{1,t}_{i+1,j-1}\right) \quad (5.5c)$$

$$I\ddot{\theta}^{2,b}_{i,j} = k_{nn}\left(\theta^{1,b}_{i,j} + \theta^{1,b}_{i,j+1} + \theta^{1,b}_{i+1,j} - 3\theta^{2,b}_{i,j}\right) - 6k_{iso}\theta^{2,b}_{i,j} + k_{iso}\left(\theta^{2,t}_{i,j+1} + \theta^{2,t}_{i-1,j} + \theta^{2,t}_{i+1,j-1}\right) - k_{iso}\left(\theta^{2,t}_{i+1,j} + \theta^{2,t}_{i-1,j+1} + \theta^{2,t}_{i,j-1}\right) \quad (5.5d)$$

5.3.2 Lieb lattice

Figure 5.3(b) displays the top layer of a unit cell of the Lieb lattice. Each layer has three disks, indexed as illustrated. Let $k_g = \max(2k_{nn} + 4\lambda_{iso}, 4k_{nn})$ be the additional term required to shift all the bands upward. The equations of motion of the six disks of the unit

cell are

$$I\ddot{\theta}^{1,t}_{i,j} = k_{nn}\left(\theta^{2,t}_{i,j} + \theta^{3,t}_{i,j} + \theta^{3,t}_{i,j-1} + \theta^{2,t}_{i-1,j}\right) - k_g\theta^{1,t}_{i,j}, \tag{5.6a}$$

$$I\ddot{\theta}^{2,t}_{i,j} = k_{nn}\left(\theta^{1,t}_{i,j} + \theta^{1,t}_{i+1,j}\right) - k_g\theta^{2,t}_{i,j} + k_{iso}\left(\theta^{3,b}_{i+1,j} - \theta^{3,b}_{i,j} + \theta^{3,b}_{i,j-1} - \theta^{3,b}_{i+1,j-1}\right) \tag{5.6b}$$

$$I\ddot{\theta}^{3,t}_{i,j} = k_{nn}\left(\theta^{1,t}_{i,j} + \theta^{1,t}_{i,j+1}\right) - k_g\theta^{3,t}_{i,j} + k_{iso}\left(\theta^{2,b}_{i-1,j+1} - \theta^{2,b}_{i-1,j} + \theta^{2,b}_{i,j} - \theta^{2,b}_{i,j+1}\right) \tag{5.6c}$$

$$I\ddot{\theta}^{1,b}_{i,j} = k_{nn}\left(\theta^{2,b}_{i,j} + \theta^{3,b}_{i,j} + \theta^{3,b}_{i,j-1} + \theta^{2,b}_{i-1,j}\right) - k_g\theta^{1,b}_{i,j}, \tag{5.6d}$$

$$I\ddot{\theta}^{2,b}_{i,j} = k_{nn}\left(\theta^{1,b}_{i,j} + \theta^{1,b}_{i+1,j}\right) - k_g\theta^{2,b}_{i,j} + k_{iso}\left(\theta^{3,t}_{i+1,j} - \theta^{3,t}_{i,j} + \theta^{3,t}_{i,j-1} - \theta^{3,t}_{i+1,j-1}\right) \tag{5.6e}$$

$$I\ddot{\theta}^{3,b}_{i,j} = k_{nn}\left(\theta^{1,b}_{i,j} + \theta^{1,b}_{i,j+1}\right) - k_g\theta^{3,b}_{i,j} + k_{iso}\left(\theta^{2,t}_{i-1,j+1} - \theta^{2,t}_{i-1,j} + \theta^{2,t}_{i,j} - \theta^{2,t}_{i,j+1}\right) \tag{5.6f}$$

Note that the disks indexed 1 and $\{2,3\}$ have different number of neighbors and hence ground springs are required to ensure that all the bands are shifted by the same amount. The ground stiffness is required on either the 1 disks or on the $\{2,3\}$ depending on the relative magnitudes of k_{nn} and k_{iso}. Its value is $4k_{iso} - 2k_{nn}$ on disk 1 if $2k_{iso} > k_{nn}$ or $2k_{nn} - 4k_{iso}$ on disks $\{2,3\}$ in each unit cell.

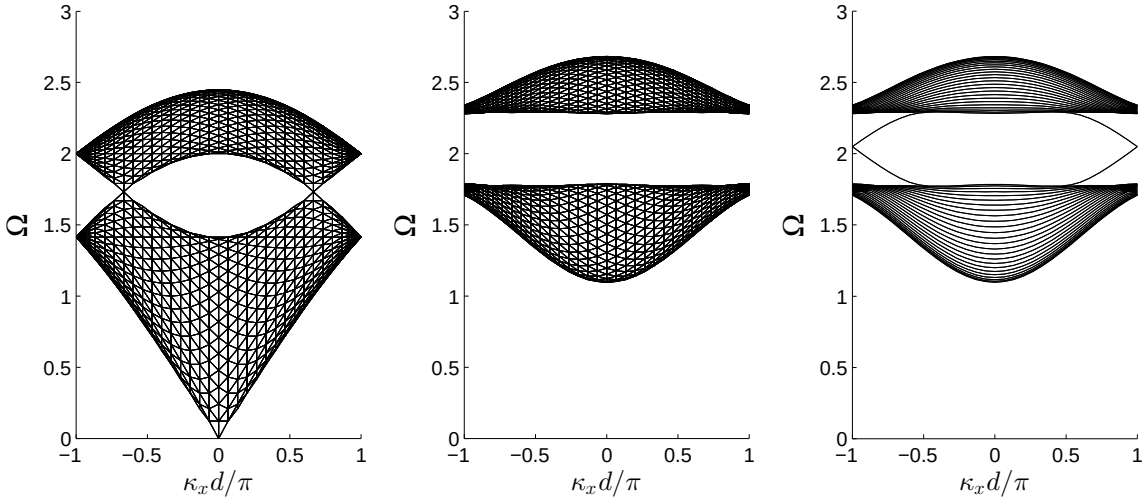

Figure 5.4: Bulk band structure with (a) $\lambda_{iso} = 0$, (b)$\lambda_{iso} = 0.2$, and (c) band diagram of a periodic strip with fixed ends and $\lambda_{iso} = 0.2$ coupling.

5.4 Results: edge modes in bi-layered mechanical lattices

Bloch wave analysis [90, 91, 3] is conducted to show the existence of TPBMs on lattice boundaries. Numerical simulations are used to verify the presence of edge states and demonstrate the excitation of a desired one-way propagating mode. The equations of motion of the lattice are solved using a 4th-order Runge-Kutta time-marching algorithm.

5.4.1 Mechanical hexagonal lattice with TPBMs

Figure 5.4 displays a projection of the dispersion surface of the hexagonal lattice onto the $x\Omega$-plane. It illustrates the progression from a structure with no bandgap to one with a topologically nontrivial bulk band gap that exhibits TPBMs. The wavenumber along x, κ_x, is normalized by the lattice vector magnitude $d = |\boldsymbol{d}_1| = |\boldsymbol{d}_2|$ and π for viewing convenience, and $\Omega = \omega/\omega_0$ where $\omega_0^2 = k_{nn}/I$. Figures 5.4(a) and 5.4(b) are dispersion relations for a 2D, periodic lattice defined by the unit cell in Fig. 5.3(a), which approximate the behavior of a lattice far from its boundaries. Figure 5.4(a) shows the dispersion relation of an uncoupled bilayer system with $k_{nn} = 1$ and $\lambda_{iso} = 0$. It consists of two identical

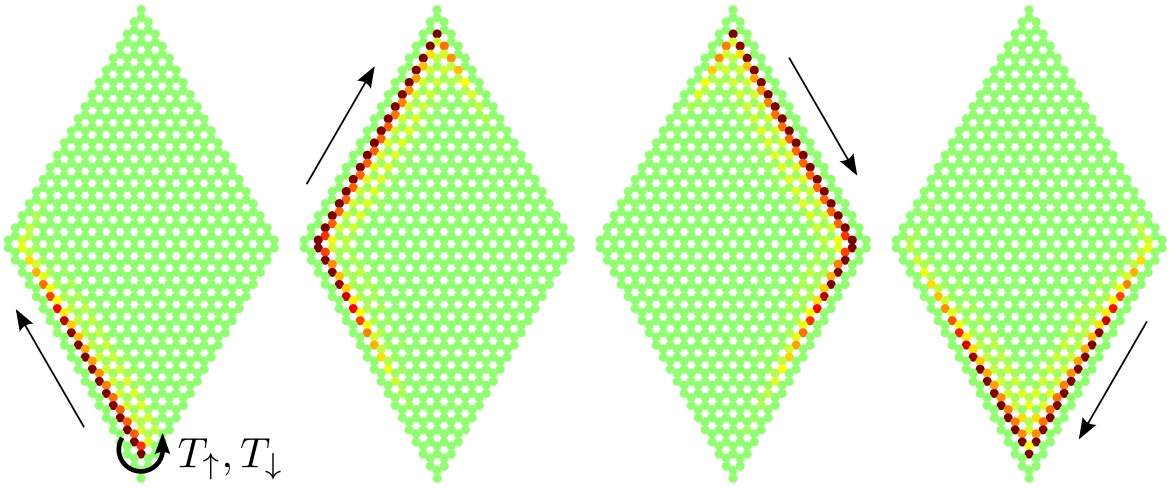

(a) $\tau = 100$ (b) $\tau = 200$ (c) $\tau = 300$ (d) $\tau = 400$

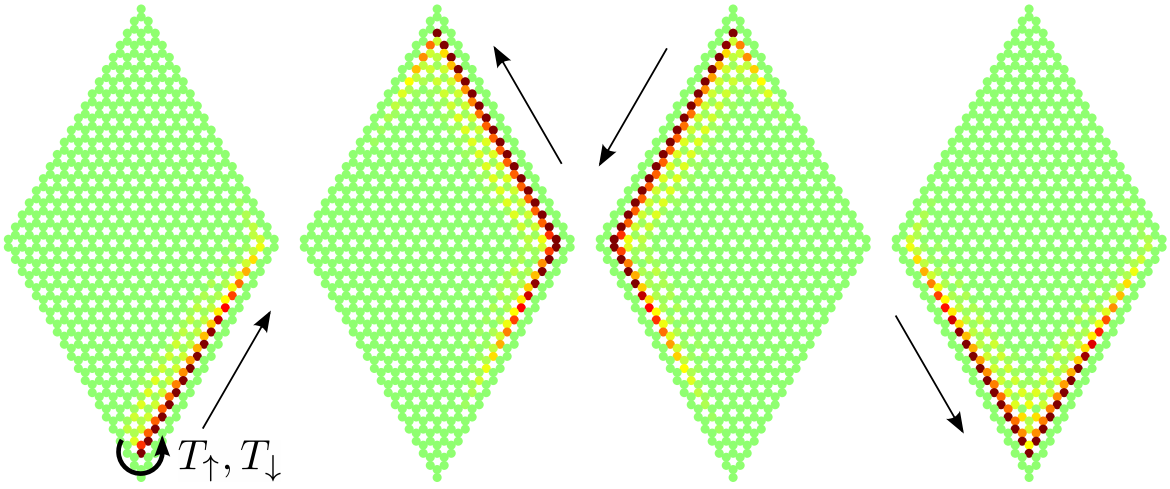

(e) $\tau = 100$ (f) $\tau = 200$ (g) $\tau = 300$ (h) $\tau = 400$

Figure 5.5: RMS displacement at each lattice site for different moments in time τ. (a-d) Clockwise propagation. (e-h) Counter-clockwise propagation. Red denotes the greatest displacement and green denotes none.

dispersion surfaces superimposed. If λ_{iso} is instead 0.2 a topologically nontrivial bandgap opens up in the coupled bi-layered system (Fig. 5.4(b)), so waves at frequencies $\Omega \approx 1.7$ to 2.3 cannot propagate in the bulk of the lattice, i.e. far from the boundaries. This is referred to as the "bulk bandgap" [63]. Also note that low frequency waves can no longer propagate and there is a band gap at low frequencies due to the presence of both normal and reverse springs. Note that reverse springs prevent zero frequency modes at zero wavenumber. To observe this, consider a chain of disks connected by reverse springs. The equation of motion of disk i is $I\ddot{\theta}_i + k_R R^2(2\theta_i + \theta_{i+1} + \theta_{i-1}) = 0$ and the dispersion relation of the system is $\omega = 2|\cos(kL/2)|$. They allow low frequency waves only at k close to π. On the other hand, a chain of disks connected by normal springs have dispersion relation $\omega = 2|\sin(kL/2)|$ and they do not permit low frequency waves close to π. Hence a combination of these normal and reverse leads to a complete band gap at low frequencies.

Bloch wave analysis is performed on a strip of the hexagonal lattice to analyze the wave modes localized on the lattice boundaries [67, 65].

A convenient way to check for the existence of TPBMs is to calculate the band diagram for the 1D, periodic system created in the following way. The unit cell is tessellated a finite number of times along one lattice vector to make a strip, and then made periodic along the other lattice vector. The result is a system with two parallel boundaries. TPBMs, if they exist in a specific structure, will manifest in the frequency range of the bulk bandgap due to the bulk-edge correspondence principle [99, 100]. Furthermore, the deformation associated with these modes, i.e. the eigenvectors, will be localized at one of the boundaries. Indeed, there is some redundancy in solving for edge modes this way, as an infinite half space would describe only one edge. However, this method requires only a small modification from a 2D Bloch analysis implementation and is therefore quite convenient and practical.

For the results shown in this article a strip of the hexagonal lattice is made by repeating 27 unit cells along $\boldsymbol{d}_1$ and then made periodic along $\boldsymbol{d}_2$ by assuming the traveling wave solution. The disks of the unit cells at each end of the strip are rigidly fixed, so there are

25 unit cells elastically connected to two rigid "walls". Similarly, to analyze another type of edge, the ends of the strip can be left free. For the Lieb lattice the strip is also made by repeating 27 unit cells (Fig. 5.3(b)) along $\boldsymbol{d}_1$, rigidly fixing the unit cells at each end of the strip, and making the strip periodic along $\boldsymbol{d}_2$.

The disks at each end of the strip are fixed. Figure 5.4(c) displays the band diagram, showing 2 boundary modes spanning the bulk bandgap. Note that there are actually 4 modes as each mode superimposes another mode. On each boundary, there are 2 modes, propagating in opposite directions and they have different polarizations [74]. Thus, an edge excited with a polarization corresponding to a boundary mode will have a wave propagating in only one direction along the boundary.

Numerical simulations are performed to demonstrate the excitation of a TPBM on a finite structure. The hexagonal lattice unit cell is tessellated into a 20 by 20 cell lattice and the outer layer of cells is fixed. One site is excited such that the torque is $T_\uparrow = \cos(\Omega\tau)$ and $T_\downarrow = \sin(\Omega\tau)$ on the top and bottom layer respectively, where time t is normalized by defining $\tau = t\omega_0$. A Hanning window is applied to $T_\uparrow$ and $T_\downarrow$ so only 60 cycles of forcing are applied, and $\Omega = 2$. The result is plotted in Fig. 5.5(a-d) for different moments in the simulation. The coloring of each site corresponds to the root mean square (RMS) of the displacement at that site, considering the disks in both the top and bottom layer. The simulations show that only one wave mode is excited, which propagates in a clockwise direction around the structure, and that this wave mode passes around the two corner types on the lattice boundary without back-scattering. The displacement magnitude is also seen to decay quickly with increasing distance from the boundary. There is little dispersion given the relatively constant slope for the edge mode at $\Omega = 2$, so the variation of the amplitude along the boundary is primarily due to the windowing of the excitation.

If the excitation to the lattice is modified so that $T_\downarrow = -\sin(\Omega\tau)$ but $T_\uparrow$ remains the same, only the wave mode which propagates counter-clockwise around the lattice is excited (Fig. 5.5(e-h)). Thus, the direction of energy propagation can be selected via the

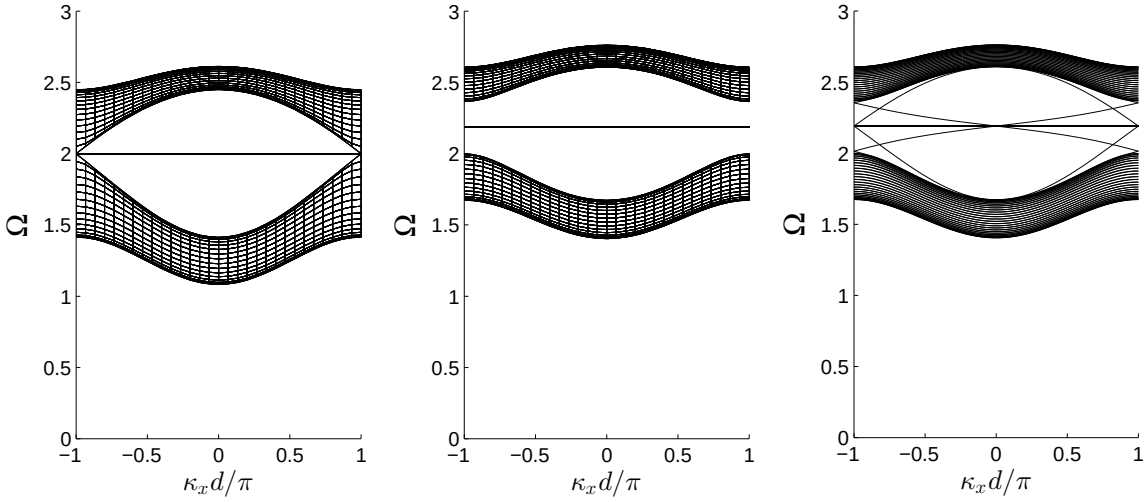

Figure 5.6: Bulk band structure with (a) $\lambda_{iso} = 0$, (b)$\lambda_{iso} = 0.2$, and (c) band diagram of a periodic strip with fixed ends and $\lambda_{iso} = 0.2$ coupling.

polarization of the input to the system.

5.4.2 Mechanical Lieb lattice with TPBMs

Our final example studies the Lieb lattice. The bulk dispersion surface of the mechanical Lieb lattice with $k_{nn} = 1$ and $\lambda_{iso} = 0$ is pictured in Fig. 5.6(a), projected on the $x\Omega$-plane with the wavenumber κ_x normalized as in the previous subsection. Low frequency waves cannot propagate, due to the presence of ground springs. The addition of inter layer coupling with $\lambda_{iso} = 0.2$ opens two bandgaps spanning $\Omega \approx 2.0$ to 2.2 and $\Omega \approx 2.2$ to 2.4.

A strip of the Lieb lattice is analyzed in the same way as the hexagonal lattice, with the disks at the boundary fixed. Note that there are two types of edges arising in the Bloch analysis of a strip. The first edge corresponds to the edge of a unit cell closer to the x-axis in the schematic in Fig. 5.3b, while the second type corresponds to the opposite edge of the unit cell. Figure 5.6(c) displays the corresponding dispersion diagram. There are 4 distinct modes localized at the boundary which span the bulk bandgaps. They correspond to the left and right propagating modes on the two distinct boundaries.

For numerical simulations, first a lattice is considered with all boundaries identical.

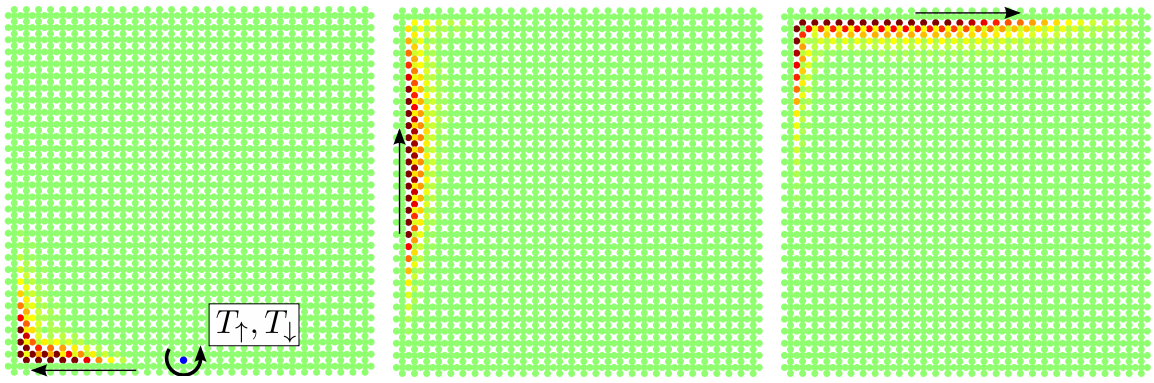

(a) $\tau = 300$ (b) $\tau = 600$ (c) $\tau = 900$

(d) $\tau = 200$ (e) $\tau = 400$ (f) $\tau = 600$

Figure 5.7: RMS displacement at each lattice site for different moments in time τ. (a-c) Clockwise propagation with one edge type. (d-f) Clockwise propagation with two edge types. Red denotes the greatest displacement and green denotes none.

The edge described by the upper end of the strip, i.e. positive y in Fig. 5.3(b), is used to demonstrate the excitation of a TPBM in a simulation of the Lieb lattice. The unit cell is tessellated into a 30 by 30 cell lattice and sites are added where needed to make all the boundaries of the same construction. Then, the outer layer of cells is fixed. The same forcing input as for the hexagonal lattice is used except $\Omega = 2.1$. With $T_\uparrow = \cos(\Omega\tau)$ and $T_\downarrow = \sin(\Omega\tau)$ a clockwise-propagating mode is excited, but if $T_\downarrow = -\sin(\Omega\tau)$, a counter-clockwise propagating wave is excited. Figure 5.7(a-c) depicts the results, and the waves are seen to transition between edges without reflections.

Next, we present numerical simulations of a wave propagating from one boundary type to another (Fig. 5.7(d-f)). The same forcing input is used as in the aforementioned simulation, and the simulation domain is a 30 by 30 cell lattice with the outer layer of cells fixed. The wave packet propagates on both edge types at different velocities, and exhibits no back-scattering when transitioning from one edge to the other. In Fig. 5.7(e-f) the wave packet looks smaller than in Fig. 5.7(a-c) because the "smooth" edge type is not as dispersive as the other, and the wave has not had as much time to disperse. Indeed, this behavior is consistent with the trends observed in the band diagram, where there are two group velocities at each frequency in the bulk bandgap region. Each mode corresponds to a localized wave on a particular boundary type and they are all unidirectional. As the wave traverses from one boundary type to the other, there is thus a change in group velocity as the wave transitions from one branch to another.

CHAPTER 6
EXPERIMENTATION ON METASTRUCTURES

6.1 Chapter overview

The purpose of this chapter is to present and discuss experiments performed on lattice structures. The first is a novel approach for the experimental characterization of the dispersion properties of in-plane waves in lattice structures using high speed cameras and digital image correlation (DIC). A 3D printed hexagonal lattice excited with a narrow-band signal is used as a benchmark for the investigation. The transient response of the lattice is recorded to measure the displacement throughout the lattice in time and processed to unveil the different directional features of longitudinal and transverse waves propagating through the structure. In the discussion of the results, elaboration on both the advantages and disadvantages of the proposed approach are discussed by comparing it to a 3D LDV. First, the experimental methodologies are described, followed by the results and discussion.

The second experiment is performed on elastic hexagonal lattices to validate the transient dynamic model used for the simulations discussed in Chapter 2. An impact event in which a brass weight is dropped on a lattice is recorded and simulated and the results are compared. The experimental procedure is first discussed, followed by the approach used to simulate the same impact event. Finally, the results of the simulation and experiment are compared.

6.2 Measurement of in-plane elastic waves in lattice structures via digital image correlation

6.2.1 Experimental methods

Hexagonal lattice fabrication

The hexagonal honeycomb lattice is manufactured out of polylactic acid (PLA) using fused deposition manufacturing (FDM). The lattice is characterized by 56x36 unit cells of dimensions $l = 3$ mm, $t = 0.8053$ mm (Fig. 6.1.a), and out-of-plane width $w = 10$ mm. The number of cells is maximized in relation to the overall area than can be fabricated by available machines. The beams comprising the hexagons have slenderness ratio $l/t \approx 3.73$ which leads to a fairly small material to void ratio. A densely filled region on the lattice boundary is included to facilitate fixturing and approximate a rigid boundary. A reflective mirror spray paint is applied to the lattice, enhancing its ability to reflect the bright lights required for short camera exposures and protects the structure from overheating. Before painting, the structure is sanded with 240 grit sandpaper to give more defined features for DIC to utilize.

Experimental setup of excitation and recording

The experimental setup is shown in Fig. 6.2. The excitation to the lattice is provided by a resonant piezoelectric (PZT) stack assembly (APC 90-4060) attached to the lattice in the location shown. The PZT resonance frequency is the considered excitation frequency $f_e = 16.74$ kHz. The excitation is applied in the form of a sinusoidal burst, with modulation being provided by an 11-cycle Tuckey window. The motion of the structure is recorded by a high-speed camera (Photron Fastcam SA1.1) which is set to record images at a rate of $f_s = 5,000$ frames per seconds. The interleaving process described below considers $n = 14$ properly delayed takes, so that the effective sampling frequency is $f_{s,eff} = nf_s = 70k$Hz. Each recording is repeated 16 times and averaged to minimize

noise. Recording is started by a manual switch connected to the camera. Once the recording started, the camera triggers a first function generator (FG1 - Agilent 33120A), which produces a square wave. The falling edge of the square wave then triggers the excitation signal produced by second function generator (FG2 - Agilent 33220A). Imposing the frequency of the first signal generator allows us to enforce the time delay needed to achieve the effective sampling rate $f_{s,eff}$. The excitation signal is then fed to the PZT exciter through an amplified (E&I 1040L). The motion of one point of the lattice is also monitored through a Laser Doppler Vibrometer (LDV) (Polytec PDV 100). The location of the monitored point is shown also in Fig. 6.2. The LDV measurements are employed to verify the repeatability of the excitation and motion during various takes and excitation cycles, as well as to compare the time histories recorded at the monitored location with those extracted from the DIC procedure. During data collection, uniform illumination of the lattice is provided by two lamps. These lamps are observed to have a small but detectable flicker in brightness at 120 Hz which is filtered out by a high-pass filter applied before the interleaving. In addition, mean subtraction in time is applied to remove any low frequency motion that may contribute to noise. A Hamming window is then applied in the time domain to minimize spectral leakage.

FE modeling and Bloch analysis

Bloch analysis is implemented numerically by using the FE commercial code ABAQUS/ Standard [101]. The unit cell, represented in Fig. 6.4, is discretized by using three-dimensional hexahedral C3D8R ABAQUS elements. The Bloch conditions, depending on the wavenumber $\boldsymbol{\kappa}$, are enforced on the nodal displacement of the boundaries of two identical unit cells, defined as real and imaginary unit cells. An eigenvalue problem is solved for the frequency ω for each value of $\boldsymbol{\kappa}$ used to discretize the Irreducible Brillouin Zone in order to obtain the dispersion relation $\omega = \omega(\boldsymbol{\kappa})$ for the structure. The material is modeled as linear elastic with Young's modulus $E = 2.46$ GPa, obtained by previously gained empirical knowledge,

mass density $\rho = 1250\ kg/m^3$ and Poisson's ratio $\nu = 0.36$.

6.2.2 Results: measured in-plane waves

The considered DIC approach is applied for the detection of in-plane wave motion of the periodic hexagonal lattice shown in Fig. 6.1.a. Motion is evaluated by tracking the position of the lattice intersections, or nodes, in the recorded images. These intersections are identified by setting a brightness threshold to each black and white image of the kind in Fig. 6.1.a, which produces a binary representation of material and void as illustrated in Fig.s 6.1.c,d. Pixels with brightness above the threshold are denoted as "material pixels". A tolerance brightness level is applied to connect each material pixel to its neighbors whose brightness may fall just below the threshold, but are still part of the lattice material, which corrects for inaccuracies resulting from the non-uniform illumination of the lattice. The search for lattice intersections proceeds by counting the number of material points within a radius $r = t/\sqrt{3}$ from each material pixel. Here, t denotes the wall thickness of the lattice, so that the radius r corresponds to the theoretical area occupied by an intersection, which is denoted as A_i in Fig. 6.1.d. It is expected that the material points with the largest number of neighbors within radius r correspond to the location of the intersection. The process is guided by the approximate estimate of the ratio of the area occupied by an intersection relative to the area of a unit cell. Based on the schematic of Fig. 6.1.d, the area occupied by three beams connected at one node is $A \approx 3/2lt$, where l denotes the length of a ligament and the distance between neighboring nodes, while the area occupied by an intersection is $A_i \approx \pi t^2/3$. The considered aspect ratio $l/t \approx 3.725$ gives $A_i/(A + A_i) \approx 15.8\%$. This ratio is employed for an initial estimate of the number of pixels, out of those identified from the thresholding, that are expected to define an intersection. This target number is lowered by an 80% factor to account and correct for variability in the thresholding process related to imperfections in manufacturing, limitations in image resolution and slight inhomogeneities in illumination. This value is chosen empirically based on comparisons

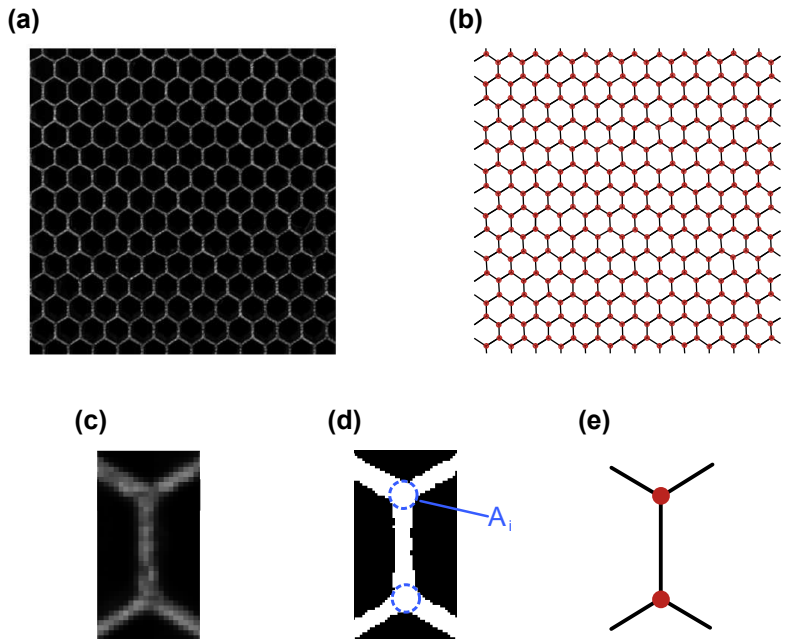

Figure 6.1: Picture of hexagonal lattice (a) and identified lattice geometry consisting of intersection points (red dots) connected by lines (black lines). Schematic of process followed for the identification of intersections and of lattice geometry (c-e).

of identified geometry and original images, and is found to provide accurate detection of all nodes. Finally, the location of the intersection is defined by the centroid of the material points within each cluster of radius r . Once the intersections are evaluated, their connectivity is determined by looking for intersections which are approximately l apart. This results in the geometrical description of the lattice as an assembly of points connected by lines as shown in Fig. 6.1.e at the local level, and in Fig. 6.1.b for the lattice assembly. This is simple procedure is limited to the specific lattice topology considered, and will require to be extended to handle a variety of topologies with complex connectivities and a variety of intersections characterized by different coordination numbers.

The intersection identification process is applied to every image recorded during the acquisition time, so that displacements can be evaluated through DIC [102, 103]. The DIC process in this work employs the open-source code by Eberl et al. [104], here adapted to track the intersection points. DIC applied to 19x19 pixel image subsets that are located at

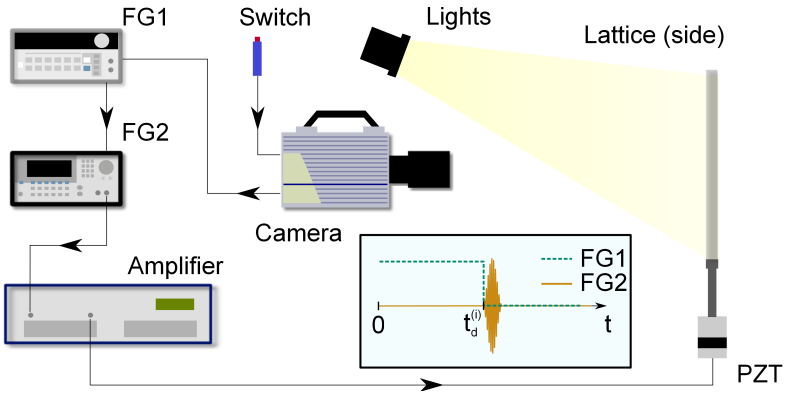

Figure 6.2: Schematic of experimental set-up.

each lattice intersection, which provides a measure of the two in-plane displacement components relative to the initial reference lattice position. The recorded motion corresponds to the transient wave induced in the lattice by a piezoelectric (PZT) stack disks assembly designed to resonate at a specified frequency. The motion of the structure is recorded by a high-speed camera which is triggered by the excitation signal. A schematic of the experimental set-up is depicted in Fig. 6.2, while details of the equipment and excitation parameters are provided in the 'Methods' section. The excitation system is selected to provide repeatable forcing and, as a result, repeatable wave motion in the lattice. This has two main advantages. First, hardware limitations of the camera impose a trade-off between frame rate and image size, *i.e.* the number of pixels captured in each frame. To circumvent this, images from n recordings at a frame rate of f_s are interleaved to obtain an effective higher frame rate $f_{s,eff} = nf_s$ [105]. This is implemented by controlling the time delay between the start of an excitation and the beginning of a recording. The time delay corresponding to the i-th recording is given by:

$$t_d^{(i)} = \frac{1}{f_s}\frac{i-1}{n} \tag{6.1}$$

where $i \in 1, ..., n$, with n denoting is the number of the recordings. In this work, we used $n = 14$ delayed recordings to realize an effective $f_{s,eff} = 14 \times f_s$, where $f_s = 5$ kHz is the frame rate provided by the video camera utilized. A schematic of the interleaving process

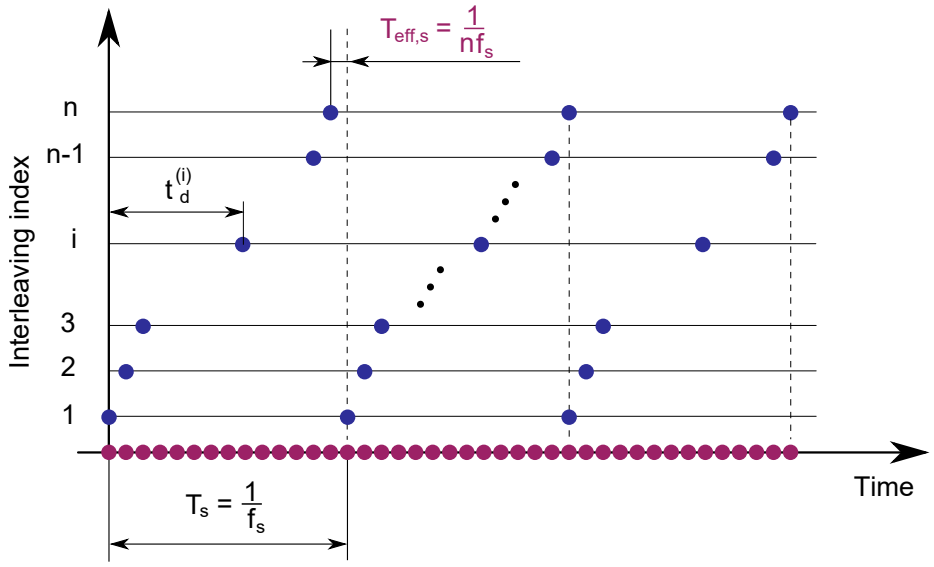

Figure 6.3: Schematic of interleaving process for enhancement of effective sampling rate.

is presented in Fig. 6.3. A second advantage is that it provides a wide effective field of view that allows capturing a sufficiently large portion of the surface area of the lattice. We elected to capture the motion only of half of the lattice, invoking symmetry of geometry and loading configuration. The monitored half surface is further divided into 4 tiles as illustrated in Fig. 6.4. Recordings are first conducted on each of the tiles. A composite video is then obtained from the combination of the 4 tiles which is obtained by aligning the intersection locations in planned overlapping regions. The composite images are obtained by first rotating each tile's coordinate system so that the edges of the overlapping area align with the global coordinate axes. Then, each tile is translated so that the centroid of its overlap region matches that of its pairing neighbor.

The recorded motion of the lattice can be represented in the form of the time snapshots in Fig.s 6.5, where the color code is associated with the resultant of the in-plane displacement components .

In addition, the motion of individual points can be extracted from the recorded images to obtain individual time-traces that can be compared with point measurements obtained for example from a single point LDV. An example of such a comparison is shown in Fig. 6.6

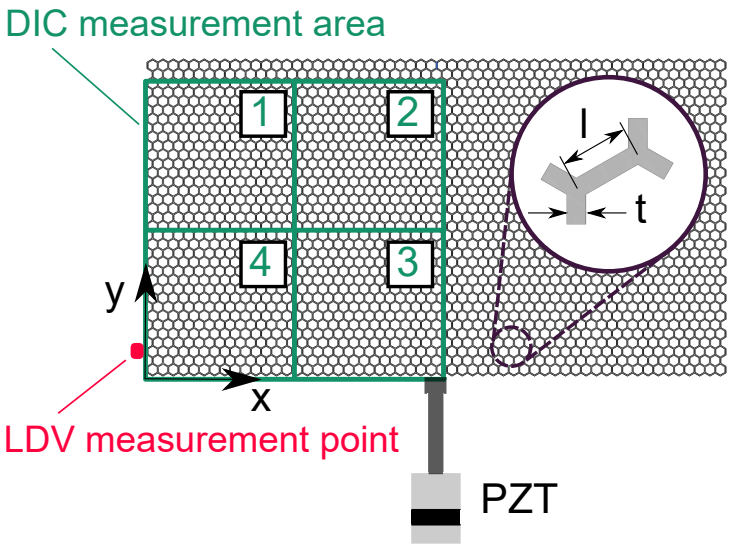

Figure 6.4: Schematic of monitored portion of surface area of the lattice, and subdivision into 4 tiles. The figure also illustrates the point of excitation as well as the location of the LDV measurements.

to illustrate how the method proposed herein is capable of providing information that is comparable with that recorded by the LDV. While the results from the DIC (black solid line) appear more noisy, which is evident from the recorded signal prior to the arrival of the wave, which occurs at $t \approx 1.5$ ms, they compare well in general trends in terms of amplitude, and of rising and decaying trends. Of note is the fact the the LDV's data were obtained from numerical integration of the LDV velocity outputs. In addition, no perfect alignment of the LDV beam relative to the lattice may lead to contribution of both horizontal and vertical displacement component, which could be considered as reasons for the relative mismatch between the data. The comparison of the two time traces indicates how the DIC technique can be employed for the description of wave motion through measurements that contain sufficient information in space and time for subsequent characterization of the wave mechanics of the lattice as discussed in the upcoming "Discussion" section.

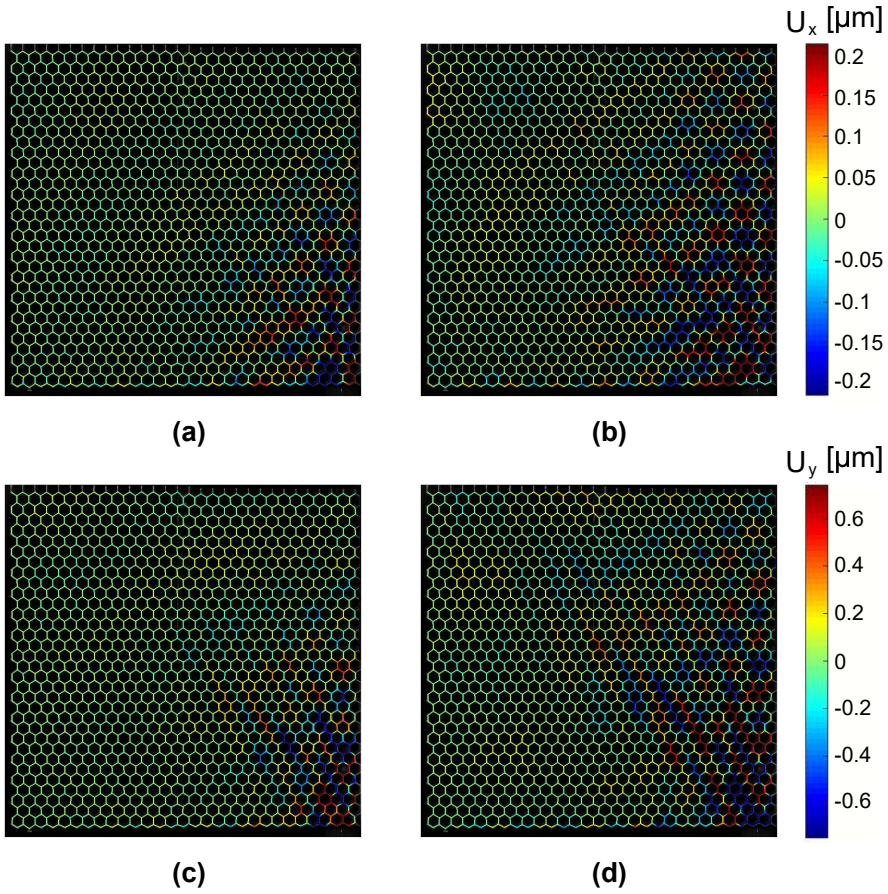

Figure 6.5: Time snapshots of the recorded wave motion in the lattice resulting from the DIC process presented: $t = 3.78$ ms (a,c), $t = 3.99$ ms (b,d) (Horizontal x component (a,b), Vertical y component (c,d)).

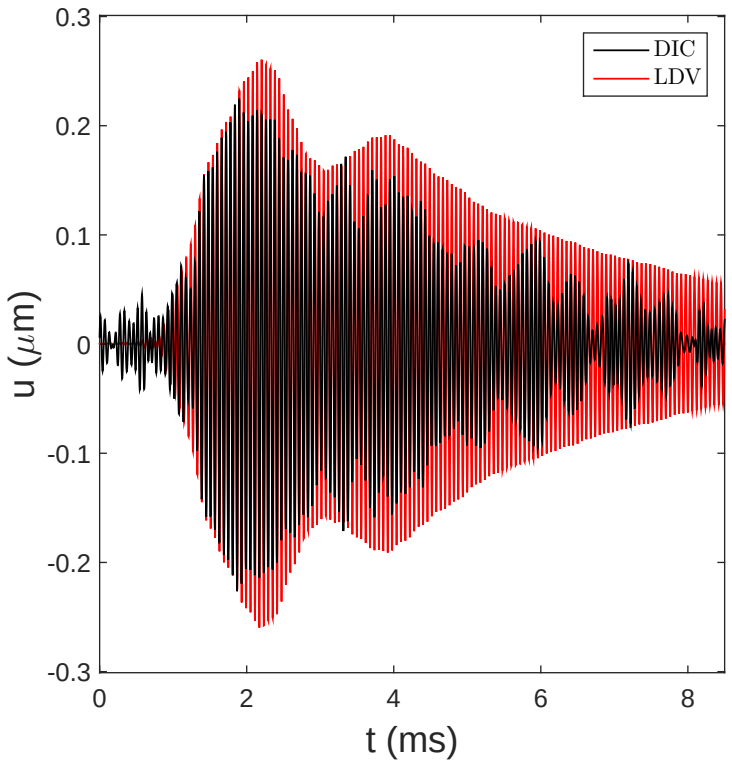

Figure 6.6: Comparison of DIC time trace with LDV measurements recorded at the location shown in Fig. 6.4.

6.2.3 Discussion

Analysis of the wave motion of the lattice as recorded through the process described in the previous section reveals some of the interesting properties that characterize the hexagonal topology here considered. The results also suggest how this measurement approach may be applied to investigate the properties of a variety of lattice topologies. Examples of such investigation enabled by the in-plane detection of wave motion are described in the following paragraphs.

The time snapshots of Fig.s 6.5 illustrate how the response of the lattice at the considered excitation frequency ($f_e = 16.74$ kHz - see "Methods" Section) is directional in space, i.e. wave motion occurs preferentially along the vertical (y) direction. This is the result of the anisotropy of this lattice which is documented for example in [30]. Such directionality can be predicted numerically by performing the dispersion analysis of the lattice as described for example in [31]. The experimental determination of the directional properties however is complicated by the fact that the recorded responses a superposition of the in-plane wave modes corresponding to longitudinal (P-mode) and transverse (S-mode) polarizations.

The availability of the in-plane displacement vector $\boldsymbol{u} = u\boldsymbol{i} + v\boldsymbol{j}$, with $\boldsymbol{i}, \boldsymbol{j}$ denoting the unit vectors aligned with the horizontal (x) and vertical (y) axes respectively, however affords the possibility to effectively separate the two modal contributions. This is achieved by employing Helmholtz decomposition to express the displacement $\boldsymbol{u}$ as a function of the scalar P-wave potential ϕ and the vector S-wave potential $\boldsymbol{\psi}$ [32]:

$$\boldsymbol{u} = \nabla\phi + \nabla \times \boldsymbol{\psi} \tag{6.2}$$

where the divergence $\nabla \cdot \boldsymbol{u} = \nabla^2\phi$ and of the nonzero component of the curl $\nabla \times \boldsymbol{u} = -\nabla^2\psi$ of the wavefield, in this case directed along the out-of-plane direction z, separate P and S-wave contributions, respectively. The spatial derivatives required for the com-

putation in eq. 6.2 are computed by first interpolating the displacements of the hexagonal grid onto a rectangular grid. This is based on a natural neighbor interpolation routine available in the Matlab environment. Next, a central difference scheme is employed for the computation of derivatives. The time snapshots of $\mathcal{P}(x, y, t) = \nabla \cdot \boldsymbol{u}$ and of $\mathcal{S}(x, y, t) = \nabla \times \boldsymbol{u}|_z$ shown in Fig. 6.7 illustrate the differences in speed, wavelength and directionality between the two wave modes. In both figures, the color map is based on normalized data, with red and blue respectively denoting maximum positive and negative values. Most notably, and as expected, the P-mode has a significantly larger wavelength and appears more isotropic than the S-mode, which is anisotropic with preferential propagation along the positive y direction and towards the top left corner of the structure. The maps of the separated modes also show that the S-mode dominates the overall response shown in Fig. 6.5. Directionality and wave speeds can be characterized and quantified by representing the two modal components $\mathcal{P}(x, y, t), \mathcal{S}(x, y, t)$ in the Fourier domain, i.e. $\hat{\mathcal{P}}(k_x, k_y, \omega), \hat{\mathcal{S}}(k_x, k_y, \omega)$ at a specific frequency. The contour plots of Figs. 6.8 correspond to the magnitudes $|\hat{\mathcal{P}}(k_x, k_y, \omega)|, |\hat{\mathcal{S}}(k_x, k_y, \omega)|$ at the excitation frequency $f_e = 16.74$ kHz and provide a distribution map of the energy content of the recorded response in the wavenumber domain. The maps also superimpose the iso-frequency contours of the theoretical dispersion surfaces for the lattice, which are represented by the solid black lines in both Fig.s 6.8. The theoretical dispersion relations are evaluated by applying established methods based on the Finite Element (FE) discretization of a unit cell, and the application of Bloch periodic conditions [31]. Both maps in Fig.s 6.8 show a good match between theoretical predictions and measured data, which demonstrates that the detected motion is descriptive of the wave properties of the lattice, and that the representation of the measured wavefields in the wavenumber space can be an effective tool for the estimation of the dispersion properties, and therefore the mechanical properties of a lattice under investigation. Of note is the fact that the iso-frequency contour has the form of a circle for the P-mode (Fig. 6.8.a), which matches the theoretical predictions well, while the S-mode reflects more

predominantly the hexagonal geometry of the lattice and its six-fold symmetry (Fig. 6.8.b).

The theoretical predictions of dispersion can be further elaborated to obtain the group velocities for the two modes at designated frequencies. Theoretical group velocities for the two modes are shown in Fig. 6.9 illustrate their different anisotropy, and further highlight the directional properties of the S-mode in particular. The group velocity directional variations provide an estimate of the shape of the wave front corresponding to the propagation in the lattice of a wave packet. Thus, at a particular time, one may superimpose the predicted wavefront to the one actually measured to once again illustrate the capabilities of the method presented here along with the theoretical estimation of dispersion to investigate wave propagation characteristics in terms of both magnitude of group velocity and directional dependence. Specific to the results in Fig. 6.9, isotropy of the P-mode at $f_e = 16.74$ kHz is confirmed by the corresponding group velocity plot, which is almost a perfect circle, signaling that the energy carried by the P-mode spreads in all the direction, with about the same average speed approximately equal to 820 m/s. The "star" pattern shown in Fig. 6.8.b instead captures the anisotropic propagation of the S-waves, which is in good agreement with theoretical predictions showing directions along which the energy is focused by the S-wave with 6-fold symmetry, with faster components of the wave traveling at about 320 m/s.

6.3 Experimental validation of the lattice model

6.3.1 Specimen description and experimental procedure

To perform a large deformation experiment, a hexagonal lattice is fabricated using two-material rapid prototyping technology. The beams comprising the lattice are made of a stiff material (Stratasys VeroWhitePlus RGD835) and the intersections or nodes of the lattice are made of an elastomer (Stratasys TangoPlus FLX930). The elastomeric nodes act as the torsional springs in the model discussed in Section 2.2. The deformation of the nodes from longitudinal loads acts as the axial springs in the aforementioned lattice model. The

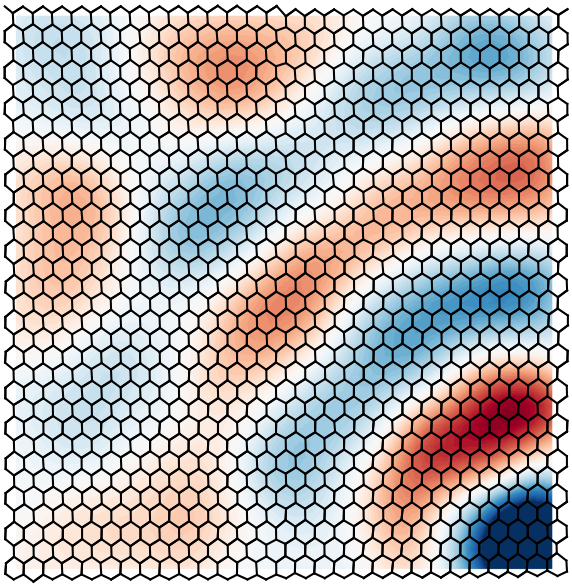

(a)

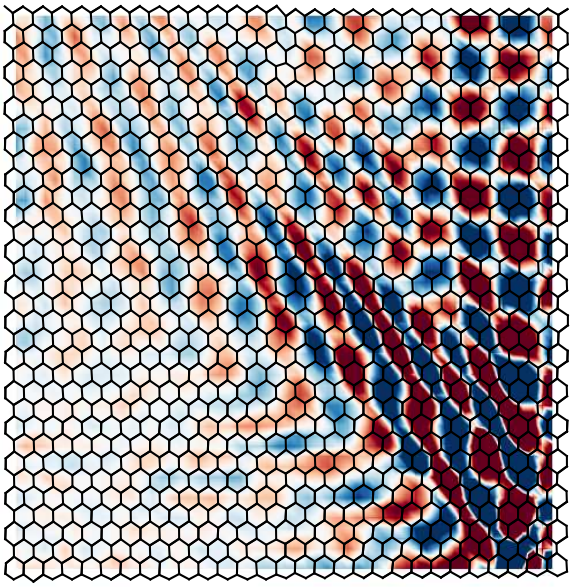

(b)

Figure 6.7: Snapshot of divergence $\mathcal{P}(x, y, t)$ (a) and curl $\mathcal{S}(x, y, t)$ (b) of the measured displacement field at $t = 3.78$ ms and $t = 4.14$ ms, respectively.

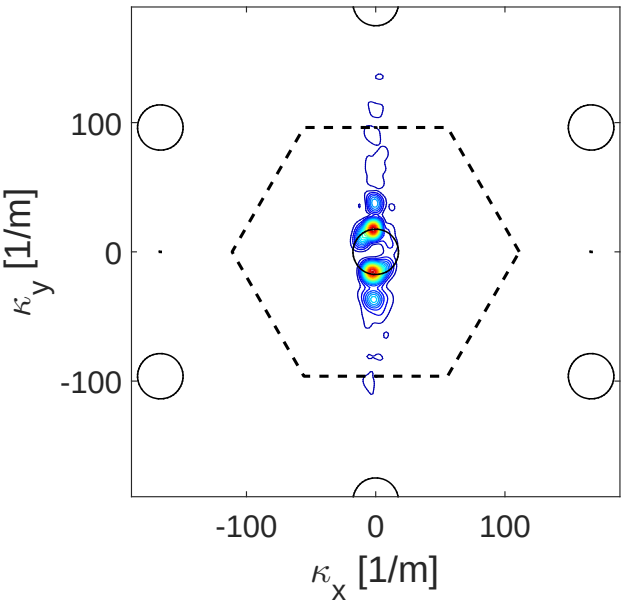

(a)

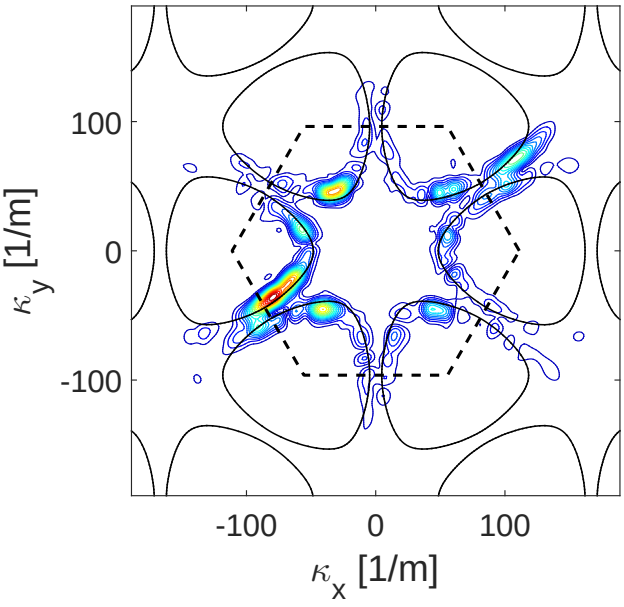

(b)

Figure 6.8: Wavenumber domain representation $|\hat{\mathcal{P}}(k_x, k_y, \omega)|$ (a), and $|\hat{\mathcal{S}}(k_x, k_y, \omega)|$ (b) at the excitation frequency and comparison with theoretical iso-frequency dispersion contours (solid black lines). The dashed black line outlines the First Brillouin Zone of the reciprocal space for the lattice [3][106].

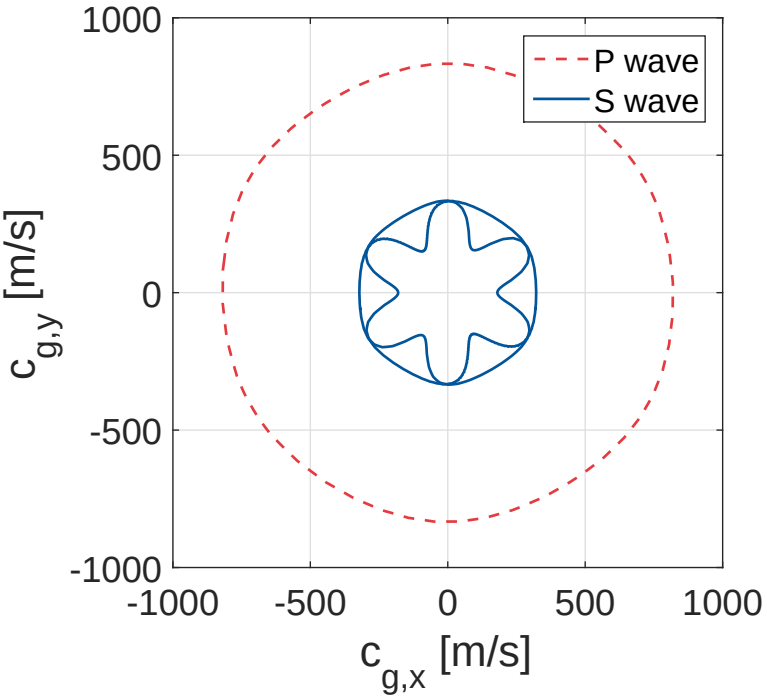

Figure 6.9: Direction variations of group velocity at the excitation frequency $f_e = 16.74$ kHz: S-mode: solid blue line, P-mode: dashed red line.

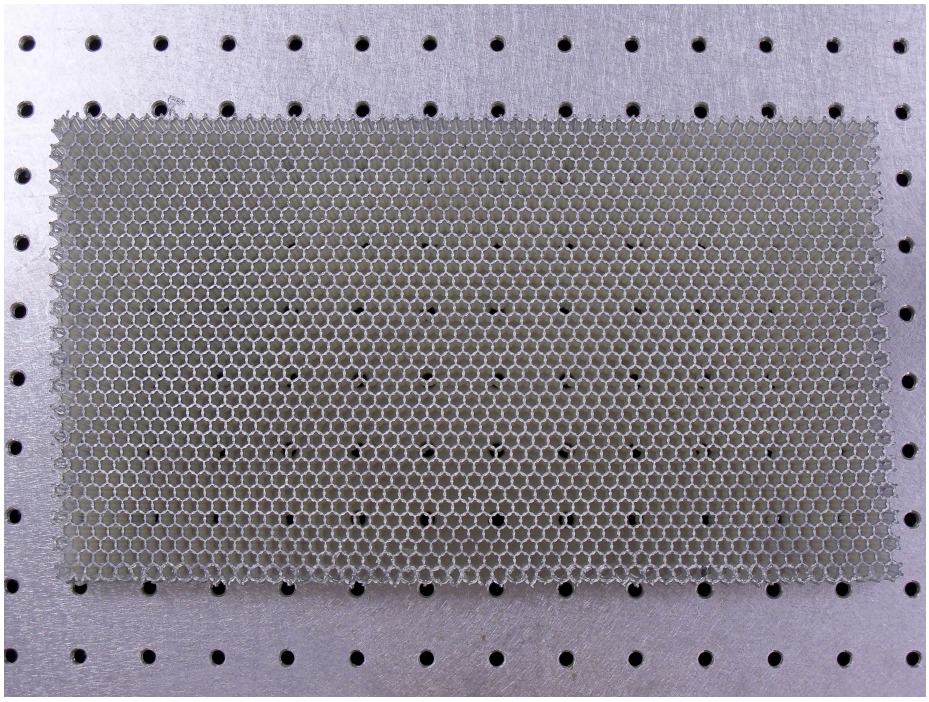

Figure 6.10: The fabricated lattice

lattice is painted with a reflective mirror paint to protect it from the bright lights required for high frame-rate photography and to reduce the amount of light required to sufficiently illuminate it. A brass cylinder with a knob on top is used as an impactor and is dropped from heights ranging from about 150 mm to 600 mm to achieve impact velocities of 1.2, 1.7, and 2.3 m/s.

A Photron Fastcam SA1.1 camera is used to record the impact events at 5,400 frames per second. To achieve sufficient lighting across the lattice two bright lamps are used to illuminate the structure. The lattice specimen is placed on a stage. A loop of string is tied to the knob on top of the impactor and another string is used to hang the impactor from this loop. A frame over the stage suspends the impactor above the lattice and the impactor is raised and dropped by hand to impact the lattice. The camera is automatically triggered to record when the impactor enters the field of view. Since the velocity of the impactor is measured to determine a simulation input, the exact height of the impactor before release is not a concern. Symmetry was intentionally broken by dropping the impactor about 1 cell

off the center of the lattice since it is expected that the fabricated specimen will not be as symmetric as the simulated lattice. By intentionally breaking symmetry, it is assumed that bifurcations that may have been driven by random fabrication error in a symmetric loading scenario will not be a factor in the performed experiment.

6.3.2 Lattice impact simulation: model specifics

To simulate the experimental impact an impactor model is added to the lumped-parameter lattice model described in Section 2.2 as follows. The impactor is modeled as a rigid rectangle with the mass and in-plane rotational inertia of the brass impactor. A phenomenological model of contact with the impactor is implemented in which lattice particles are allowed to penetrate the impactor and receive a force perpendicular to the surface of penetration directly proportional to the depth of penetration. The constant used for this proportional relationship is 2 times the contact stiffness, since two intersections in series define the contact stiffness αk_a, and only one node is involved in the contact interaction with the comparatively rigid impactor. Hence, the stiffness is $2\alpha k_a$. No energy dissipation or friction regarding impactor contact is included. Thus, the force on particle i by the impactor is:

$$\vec{f_i} = 2\alpha k_a \delta_p \hat{n}_s$$

where δ_p is the depth of penetration measured perpendicular from the impactor surface and $\hat{n}_s$ is the outward facing unit normal vector of the surface of entry. The reaction forces from the particles contacting the impactor are applied to the impactor center of gravity G as a net force $\vec{F}_G$ and moment $\vec{M}_G$, which are:

$$\vec{F}_G = -\sum_i \vec{f_i} \tag{6.3}$$

$$\vec{M}_G = -\sum_i \vec{r}_{i/G} \times \vec{f_i} \tag{6.4}$$

where $\vec{r}_{i/G}$ is the location of $\vec{f}_i$ relative to G. Equations (6.3) and (6.4) are integrated in time with the lattice equations of motion to obtain the impactor's motion. In addition, gravity is added to the simulation by applying the weight of each particle and the impactor at each time step. To achieve the correct initial lattice position, the initial lattice equilibrium calculation also includes gravity.

The particles on the boundary which corresponds to the side of the lattice contacting the table are fixed against translating. The other lattice boundaries are left free.

Identification of physical properties

The mass of the painted lattice is $m_l = 299.8$ g. Composed of $N_b = 6,010$ bars, the average bar mass is $m_b = m_l/N_b$. Since the mass of the bars is lumped to the intersections, assigning $m_b/2$ to each, and all non-boundary intersections join 3 bars, the particle mass for non-boundary intersections is

$$m_p = \frac{3}{2}m_b = \frac{3}{2}\frac{m_l}{N_b} = 74.8 \text{ mg}$$

Particles on the lattice boundary where there are only two bars per intersection have a mass of $2m_p/3$.

The lumping of mass at the intersections causes the rotational inertia of the beams to be artificially high by a factor of 3 if rotating about their centers and by a factor of 1.5 if rotating about their ends. However, the rotational inertia of the bars is insignificant compared to the torsional stiffness of the intersections. Consider a bar from the lattice pivoting about one intersection with a rotational inertia of $I_b^e = mr_0^2/3$. The resonant frequency of this simple system is 2.9 kHz when attached to a torsional spring of the stiffness identified for the lattice below. The impact event takes some 90 ms and therefore has a significantly lower frequency content than concerns the inertia of the bars pivoting about the intersections. In addition, the rotational inertia of the intersections is neglected, i.e. $I = 0$.

The torsional stiffnesses used to model the lattice are obtained using a 3D nonlinear finite element model of an elastomeric intersection. The 3rd order Ogden model recorded in [107] for Stratasys TangoPlus FLX930 is used. Two of the locations on the intersection that would attach to stiff beams are made fixed. The third location that would attach to the last beam is constrained to move as a rigid entity, and has a rotation applied to it. The reaction torque on the rotated boundary is measured. A linear fit is applied to the results to estimate an equivalent linear stiffness for modelling the rotational stiffness of the intersection. The slope is $k_{eff} = 1.271 \times 10^{-3}$ Nm/rad, which is the effective stiffness of the two branches with fixed ends in parallel, connected to the rotated branch in series. Hence, the torsional spring has the stiffness $k_\tau = 3k_{eff}/2 = 1.907 \times 10^{-3}$ Nm/rad.

It is clear from observing the lattice under arbitrary forcing that the angular deformation of the intersections dominates the compliance of the lattice, since the length of the bars does not change noticeably and the orientation of bars about an intersection change significantly under the same loading. Consider the deformation from a force F on the end of a lever of length r_0 attached to a torsional spring of stiffness k_τ. The deformation along the arc swept by the lever is $\delta_\tau = Fr_0^2/k_\tau$. The deformation of an axial spring under the same load F is $\delta_s = F/k_a$. The comparison of these deformations is

$$\phi = \frac{\delta_s}{\delta_\tau} = \frac{k_\tau}{k_a r_0^2} \tag{6.5}$$

which, when using the lattice parameters, gives a measure of which type of elastic interaction dominates the compliance of the lattice. Therefore, the observation that the lattice compliance is dominated by angular deformation of the intersections implies that ϕ for the lattice is low, i.e. below 10^{-1}. As long as ϕ is small, its precise value should have little effect on the large deformation results simulated. A value of $\phi = 10^{-2}$ is chosen.

Since the axial compliance $1/k_a$ comes mostly from the series deformation of the nodes at either end of a bar, and the soft nodes are deforming serially during contact, the contact

stiffness is expected to be the same order of magnitude as the axial stiffness. The contact stiffness is assumed to be $3k_a$, i.e. $\alpha = 3$ as it is expected to be stiffer than the axial interactions. However, since the primary lattice compliance comes from the torsional springs the exact value of the contact stiffness should not be of great importance. Energy dissipation in the lattice was not measured and is not included in the simulations, so all damping parameters are 0.

The mass of the impactor and the string loop used to suspend it is $m_I = 228.9$ g. The geometry of the knob on top of the cylinder and the blind hole that it threads into are neglected when calculating the rotational inertia. Hence a cylinder with the dimensions of the main body of the impactor but the total mass of the impactor and string loop is used. The rotational inertia is:

$$I_I = \frac{m_I}{12}\left(3\left(\frac{W}{2}\right)^2 + H^2\right) \tag{6.6}$$

The diameter of the impactor is $W = 31.70$ mm and the height of the cylinder is $H = 32.44$ mm, so the rotational inertia used is 3.444×10^{-5} kgm^2.

The position of the center of the impactor's bottom face in a frame was measured by manually identifying the two bottom corners of the impactor in a frame and averaging their position. Distance in meters is measured from the frames using the known size of the lattice cells. The angular orientation θ_I of the impactor is also measured using the two identified corners (x_1, y_1) and (x_2, y_2) such that

$$\theta_I = \arctan\left(\frac{y_2 - y_1}{x_2 - x_1}\right)$$

The position of the impactor is measured in the first 11 frames before the impactor contacts the lattice. The initial velocity of the impactor is obtained from a linear fit to these positions, which assumes the impactor is moving at a constant velocity over the 2 ms before impact. Velocities of 1.2, 1.7, and 2.3 m/s are measured for the impact events considered.

6.3.3 Comparison of experimental and numerical results

The simulated and recorded lattices are pictured at three moments after impact for each of the three ascending impactor velocities in Figs. 6.11, 6.12, and 6.13 respectively. Each greater impact velocity produces deeper penetration, which brings about the collapse of a larger number of hexagonal cells. Repeated experiments produce qualitatively similar results.

One notable difference between the simulation and the experiment is the flattening of the first row of cells contacted by the impactor. This could possibly be due to the frictionless contact assumed between the impactor and the lattice. The response of the cells near the impactor on the impacted surface appear similar in the simulation as in the experiment. Due to the nature of the lattice fabrication, it is possible that some defects, which are associated with movement errors of the rapid prototyping machine and the periodicity of the structure, will be periodic. Periodic errors could effect the global behavior of the lattice and may bias the reconfiguration. An avenue for future work that may be of value is intentional biasing of lattice geometry and properties to guide global reconfigurations.

The measured and simulated impactor positions over time are superimposed in Fig. 6.14 for a direct comparison. Given the approximation introduced in modeling the lattice with lumped parameters in 2D without damping, the simulation is not far off from the experiment. The comparison of the impactor positions shows that the effect of viscoelastic nature of the experimental lattice, which is expected to be the largest contributer to energy dissipation, is a significant component of the recorded phenomenon. The simulation does not include damping and hence exhibits less deceleration of the impactor while in contact with the lattice, leading to deeper lattice penetration. Furthermore, the speed of the impactor when returning to $y = 0$ is approximately equal to the initial speed in the simulations. In contrast, the experimental impactor leaves the lattice with a noticeably lower velocity magnitude than its initial velocity.

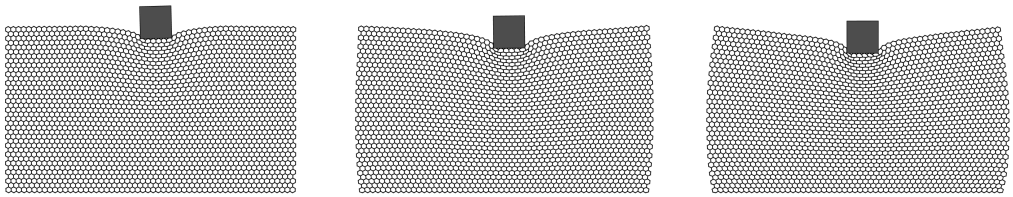

(a) $t = 11.7$ ms (b) $t = 23.3$ ms (c) $t = 35.0$ ms

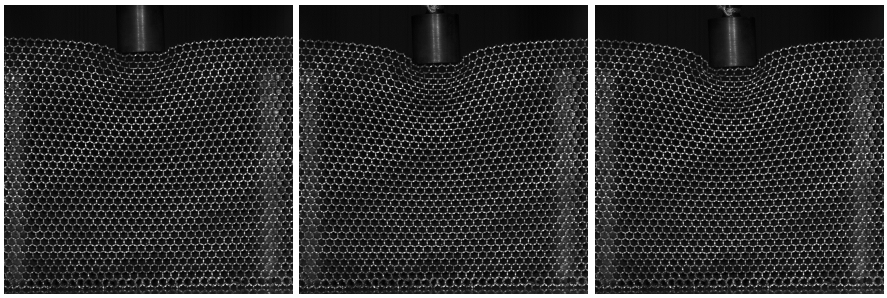

(d) $t = 11.7$ ms (e) $t = 23.3$ ms (f) $t = 35.0$ ms

Figure 6.11: The simulated (a-c), and experimental lattice (d-f) at 3 instances in time after the impactor contact at 1.2 m/s

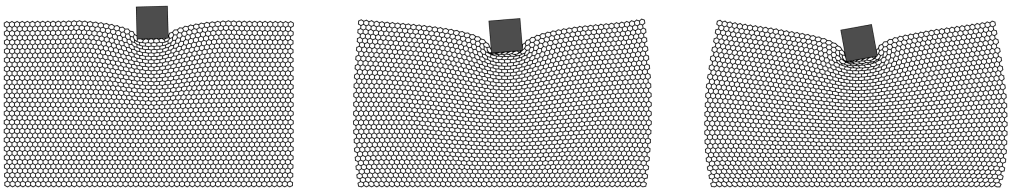

(a) $t = 11.7$ ms (b) $t = 23.3$ ms (c) $t = 35.0$ ms

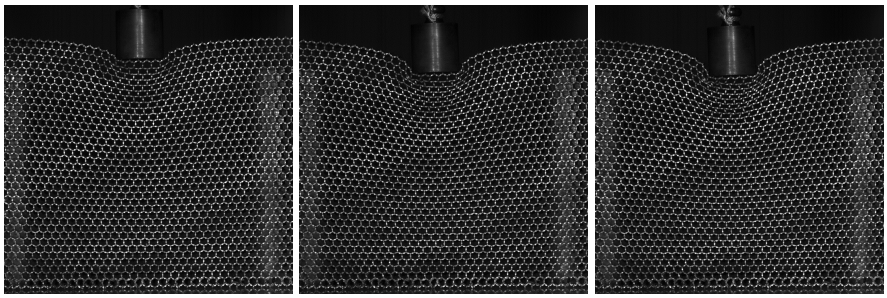

(d) $t = 11.7$ ms (e) $t = 23.3$ ms (f) $t = 35.0$ ms

Figure 6.12: The simulated (a-c), and experimental lattice (d-f) at 3 instances in time after the impactor contact at 1.7 m/s

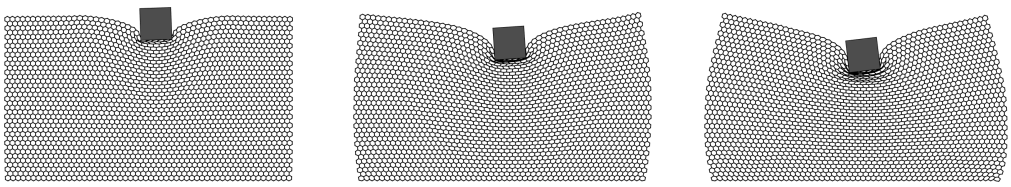

(a) $t = 11.7$ ms (b) $t = 23.3$ ms (c) $t = 35.0$ ms

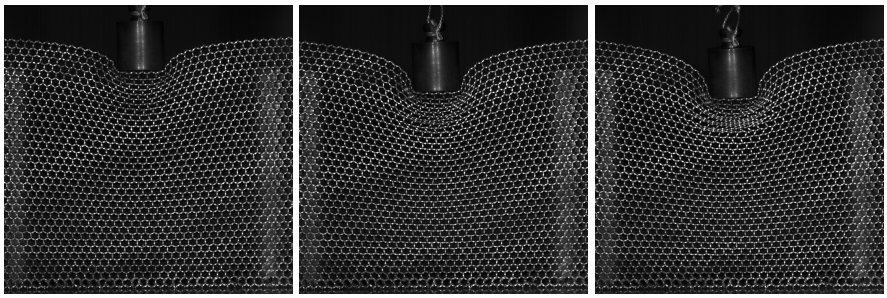

(d) $t = 11.7$ ms (e) $t = 23.3$ ms (f) $t = 35.0$ ms

Figure 6.13: The simulated (a-c), and experimental lattice (d-f) at 3 instances in time after the impactor contact at 2.3 m/s

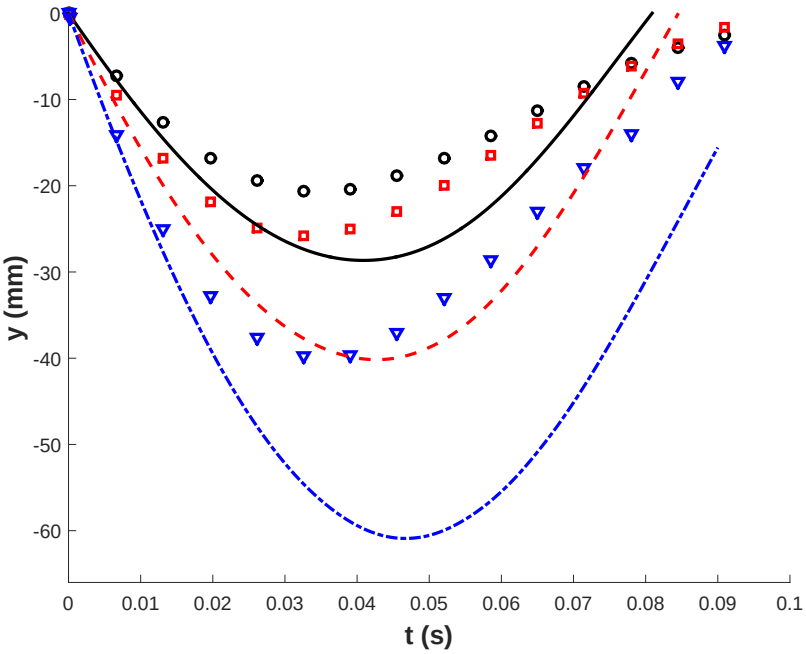

Figure 6.14: Direct comparison of experimental (points) and simulated (curves) impactor position for 1.2 m/s (black circles and solid curve, 1.7 m/s (red squares and dashed curve), and 2.3 m/s (blue triangles and dot-dashed curve))

CHAPTER 7
CONCLUSION

7.1 Summary

This thesis presents the investigation of lattice structures for the purpose of providing novel pathways for wave and mechanical property control. Structures of the type studied are often called "metamaterials" or "metastructures" as they behave in a way that is beyond their constituents. Magneto-elastic lattices are the primary focus, since they are generally multistable, allowing one structure to assume various geometric configurations, which can correspond to various functional modes, providing the possibility for adaptive structures. Periodic structures are considered for their unique wave properties, as well as for ease of design and application, including: 2D hexagonal, re-entrant, and kagome lattices.

A fundamental step to the analysis of reconfigurable structures is the identification of possible stable configurations. By minimizing energy a variety of configurations are identified for further study. A method for transition from one stable configuration to another is required to make use of the reconfiguration. So, dynamic reconfiguration is investigated as a fast and versatile method for switching configurations via transient numerical simulations. Bloch wave analysis is applied to models of magneto-elastic lattices to investigate the possible wave propagation changes. The introduction of anisotropic wave propagation, opening of bandgaps, and changes in wave speeds are observed as a result of geometric lattice reconfiguration. Reconfiguration also drastically effects static properties. The equivalent continuum properties of magneto-elastic lattice structures are calculated using a homogenization methodology. Reconfiguration from hexagonal to re-entrant lattices produces over an order of magnitude change in stiffness while converting the lattice from having isotropic to orthotropic properties.

While magneto-elastic structures are the primary focus, this thesis also addresses two other topics relevant to the development of periodic structures that seek to control wave energy. The first, pursuing novel wave control, is topologically protected edge modes, or edge states. Building by analogy from quantum mechanics, elastic mechanical structures are designed that carry special waves modes, which are termed helical edge states, in only one direction along a lattice boundary. A hexagonal and Lieb lattice are investigated as examples of a methodology developed which defines a family of mechanical lattices that can exhibit such wave modes. Analytical approaches predict the phenomena and numerical simulations verify the predictions. Another topic is the development of a methodology for measuring in-plane waves in lattice structures, which is needed for the experimental validation of the theoretical wave propagation results found in this thesis. In-plane waves modes are very common in metastructures research, but there is presently no easy way to measure such waves. As a new methodology, digital image correlation is combined with high-speed photography. The transient propagation of in-plane waves in an elastic hexagonal honeycomb lattice is measured to develop the method, and comparisons are made to finite element predictions to show the efficacy.

7.2 Contributions

The following contributions are made to the understanding of metastructures:

1. Introduction of magneto-elastic structures for adaptation of wave properties through geometric reconfiguration. A lumped parameter model is developed to illustrate the fundamentals of reconfigurable magneto-elastic structures (Section 2.2). Various stable configurations , which have different wave propagation properties are identified through energy minimization (Section 2.3), and are analyzed using Bloch analysis (Section 3.2). Both periodic configurations and arbitrary finite configurations are possible, allowing a rich set of possibilities. Both 1D (Section 3.3) and 2D (Section 3.4) structures are investigated though analytical and numerical calculations,

and significant changes in wave propagation result from reconfiguration.

2. Introduction of dynamic reconfiguration as a means for adapting wave properties of magneto-elastic structures. Controlled dynamic forcing leads to transient dynamics that determine a final structural configuration, as does tailoring the unit cell energy profile (Section 2.4). By determining the final configuration, the wave properties of the structure are controlled. The dynamic reconfiguration code is also validated against an impact experiment (Section 6.3).

3. Quantification of the effect of magneto-elastic structural reconfiguration on equivalent continuum properties. A methodology is extended to fit magneto-elastic lattices (Section 4.2), showing that the equivalent orthotropic mechanical properties of 2D magneto-elastic lattices can change by over an order of magnitude due to reconfiguration alone (Section 4.4). Reconfigurations of 1D lattices are also seen to have a significant effect on equivalent lattice stiffness (Section 4.3).

4. Identification of new mechanical topological insulators. New mechanical lattices are added to a presently short list of lattices which can exhibit one-way wave propagation along their boundaries. A methodology is developed which allows the conversion from a set of quantum-mechanical systems to elastic analogs (Section 5.2) and analytical results are verified against numerical simulations (Section 5.4).

5. Development of a new technique for measuring in-plane waves in lattice structures. High-speed photography and digital image correlation (DIC) are combined with geometry recognizing algorithms to measure the time history of the in-plane displacements of lattice nodes (Section 6.2).

7.3 Future work

7.3.1 Dynamic reconfiguration

Of the contributions outlined in Section 7.2 undertaken with magneto-elastic lattices, the one which has the most closely related work left open is dynamic reconfiguration as a means of adapting wave properties. The primary piece missing is a method for planning the transition path of a structure. Ideally, one could specify an initial structure and a desired final configuration, and then calculate the proper forcing and lattice construction required to achieve the final configuration. Such a capability would be indispensable for the application of reconfiguration as a means for control in the application of metastructures. The nudged elastic band method [108, 109, 110] was applied to address this need, but was found insufficient as it was not robust.

A step towards the larger goal of finding transition paths to arbitrary configurations is investigating the propagation of 2D and 3D transition fronts in lattices, *i.e.* the traveling boundary between two different configurations of a lattice. Presently only 1D transition fronts have received much attention. A description of the velocity of the triangular transition front seen in Section 2.4 as a function of lattice parameters and forcing would a good next step. Floppy modes [80] are another possible avenue to understanding a subset of possible reconfigurations. Given their topological nature floppy modes may be a robust reconfiguration mechanism.

7.3.2 Wave propagation control through reconfiguration

The design and evaluation of acoustic devices that can be made with reconfigurable lattices would develop what is the end goal of this research, *i.e.* adaptable devices, which can be applied by engineers. Therefore, useful examples of reconfigurable devices would motivate further research in this field. Such devices could include acoustic lenses, cloaks, multiplexes, filters, or other signal processors, etc.

A larger set of reconfigurable lattices would also allow more possibilities for adaptable devices. Expanding further into elastic-only lattices could simplify applications, while including other multi-physics lattices outside of magneto-elasticity would allow for the most broad range of applications. The consideration of 3D lattices, though much more difficult, would be the greatest extension of reconfigurable lattice identification, and is required for the broad application of such structures.

7.3.3 Topologically protected boundary modes

Affecting TPBMs through reconfiguration is not expected to be an unreasonable task. An experiment recorded in [79] demonstrates, with a time reversal symmetry (TRS) breaking structure, that a hexagonal and re-entrant lattice of gyroscopes have one way chiral TPBMs that propagate in opposite directions, and in-between the hexagonal and re-entrant states there is a state with no edge mode. This shows that reconfiguration is a valid way to affect the existence of TPBMs. The proposed goal is to extend the concept to other lattices, such as those preserving TRS and exhibiting helical TPBMs. As a possible component for designing structures with TPBMs, investigations regarding the breaking of the linearized stiffness matrix symmetry through the asymmetry in magnetic torques [78] is suggested. Preliminary efforts towards this end were taken, but no significant results were obtained. If magnetic interactions become a key component in achieving the TPBMs it is likely that they will also lead to multistability.

Overall, the understanding of TPBMs in mechanical structures is still very young. Deeper understanding and more examples are required. Simple examples of mechanical lattices exhibiting helical edge modes are specifically in great need. In conjuncture, literature that makes the methodologies more usable for mechanical-focused researches would benefit the research community significantly, as much of the fundamentals are buried deep inside quantum-mechanics. Experiments exhibiting helical edge modes are still in short supply. A particular step that would be good to take is a simple, lumped mass lattice,

which requires no constrains on its degrees of freedom to achieve TPBMs, *i.e.* a passive structure that can stand alone with no grounding frame. Such a structure will be the first of its kind and, if simple enough, will be able to demonstrate some fundamentals that are lost in lattices requiring high degree of freedom finite element calculations such as the structure in [77].

REFERENCES

[1] T. A. Schaedler, A. J. Jacobsen, and W. B. Carter, "Toward lighter, stiffer materials," *Science*, vol. 341, no. 6151, pp. 1181–1182, 2013.

[2] L. J. Gibson and M. F. Ashby, *Cellular solids: Structure and properties*. Cambridge university press, 1999.

[3] M. I. Hussein, M. J. Leamy, and M. Ruzzene, "Dynamics of phononic materials and structures: Historical origins, recent progress, and future outlook," *Applied Mechanics Reviews*, vol. 66, no. 4, p. 040 802, 2014.

[4] M.-H. Lu, L. Feng, and Y.-F. Chen, "Phononic crystals and acoustic metamaterials," *Materials Today*, vol. 12, no. 12, pp. 34–42, 2009.

[5] P. Deymier, *Acoustic metamaterials and phononic crystals*, ser. Springer Series in Solid-State Sciences. Springer, 2013.

[6] H. N. Wadley, "Multifunctional periodic cellular metals," *Philosophical Transactions of the Royal Society A: Mathematical, Physical and Engineering Sciences*, vol. 364, no. 1838, pp. 31–68, 2006.

[7] M. Ruzzene, F. Scarpa, and F. Soranna, "Wave beaming effects in two-dimensional cellular structures," *Smart materials and structures*, vol. 12, no. 3, p. 363, 2003.

[8] B. J. Olson, S. W. Shaw, C. Shi, C. Pierre, and R. G. Parker, "Circulant matrices and their application to vibration analysis," *Applied Mechanics Reviews*, 2014.

[9] R. G. S. Barsoum, "Protection against tbi using polymers for shock mitigation," in *A Survey of Blast Injury across the Full Landscape of Military Science*, RTO Human Factors and Medicine Panel (HFM) Symposium, 2011.

[10] M. Carrara, M. R. Cacan, M. J. Leamy, M. Ruzzene, and A. Erturk, "Dramatic enhancement of structure-borne wave energy harvesting using an elliptical acoustic mirror," *Applied Physics Letters*, vol. 100, no. 20, 204105, p. 204 105, 2012.

[11] J. O. Vasseur, O. B. Matar, J. F. Robillard, A.-C. Hladky-Hennion, and P. A. Deymier, "Band structures tunability of bulk 2d phononic crystals made of magneto-elastic materials," in *AIP Advances*, AIP, 2011, p. 041 904.

[12] F. Moon and P. J. Holmes, "A magnetoelastic strange attractor," *Journal of Sound and Vibration*, vol. 65, no. 2, pp. 275–296, 1979.

[13] R. Harne and K. Wang, "A review of the recent research on vibration energy harvesting via bistable systems," *Smart Materials and Structures*, vol. 22, no. 2, p. 023 001, 2013.

[14] M. Lapine, I. V. Shadrivov, D. A. Powell, and Y. S. Kivshar, "Magnetoelastic metamaterials," *Nature materials*, vol. 11, no. 1, pp. 30–33, 2011.

[15] J. N. Grima, R. Caruana-Gauci, M. R. Dudek, K. W. Wojciechowski, and R. Gatt, "Smart metamaterials with tunable auxetic and other properties," *Smart Materials and Structures*, vol. 22, no. 8, p. 084 016, 2013.

[16] J. N. Grima, E. Chetcuti, E. Manicaro, D. Attard, M. Camilleri, R. Gatt, and K. E. Evans, "On the auxetic properties of generic rotating rigid triangles," *Proceedings of the Royal Society A: Mathematical, Physical and Engineering Science*, vol. 468, no. 2139, pp. 810–830, 2012.

[17] K Bertoldi and M. Boyce, "Mechanically triggered transformations of phononic band gaps in periodic elastomeric structures," *Physical Review B*, vol. 77, no. 5, p. 052 105, 2008.

[18] K. Bertoldi, P. M. Reis, S. Willshaw, and T. Mullin, "Negative poisson's ratio behavior induced by an elastic instability," *Advanced materials*, vol. 22, no. 3, pp. 361–366, 2010.

[19] P. Wang, F. Casadei, S. Shan, J. C. Weaver, and K. Bertoldi, "Harnessing buckling to design tunable locally resonant acoustic metamaterials," *Physical review letters*, vol. 113, no. 1, p. 014 301, 2014.

[20] K. Bertoldi, S. H. Kang, S. Shan, and F. Candido, "Shape programmable structures," in *ASME 2014 International Mechanical Engineering Congress and Exposition (IMECE2014)*, 2014.

[21] V. Smirnov, O. Gendelman, and L. Manevitch, "Front propagation in a bistable system: How the energy is released," *Physical Review E*, vol. 89, no. 5, p. 050 901, 2014.

[22] N. Nadkarni, C. Daraio, and D. M. Kochmann, "Dynamics of periodic mechanical structures containing bistable elastic elements: From elastic to solitary wave propagation," *Physical Review E*, vol. 90, no. 2, p. 023 204, 2014.

[23] A. Cherkaev, E. Cherkaev, and L. Slepyan, "Transition waves in bistable structures. i. delocalization of damage," *Journal of the Mechanics and Physics of Solids*, vol. 53, no. 2, pp. 383–405, 2005.

[24] L. Slepyan, A. Cherkaev, and E. Cherkaev, "Transition waves in bistable structures. ii. analytical solution: Wave speed and energy dissipation," *Journal of the Mechanics and Physics of Solids*, vol. 53, no. 2, pp. 407–436, 2005.

[25] L. Slepyan and M. Ayzenberg-Stepanenko, "Localized transition waves in bistable-bond lattices," *Journal of the Mechanics and Physics of Solids*, vol. 52, no. 7, pp. 1447–1479, 2004.

[26] V. S. Guthikonda and R. S. Elliott, "Modeling martensitic phase transformations in shape memory alloys with the self-consistent lattice dynamics approach," *Journal of the Mechanics and Physics of Solids*, vol. 61, no. 4, pp. 1010–1026, 2013.

[27] L. Truskinovsky and A. Vainchtein, "Kinetics of martensitic phase transitions: Lattice model," *SIAM Journal on Applied Mathematics*, vol. 66, no. 2, pp. 533–553, 2005.

[28] F. E. Hildebrand and R. Abeyaratne, "An atomistic investigation of the kinetics of detwinning," *Journal of the Mechanics and Physics of Solids*, vol. 56, no. 4, pp. 1296–1319, 2008.

[29] O. Kastner and G. Ackland, "Mesoscale kinetics produces martensitic microstructure," *Journal of the Mechanics and Physics of Solids*, vol. 57, no. 1, pp. 109–121, 2009, cited By 12.

[30] S. Gonella and M. Ruzzene, "Analysis of in-plane wave propagation in hexagonal and re-entrant lattices," *Journal of Sound and Vibration*, vol. 312, no. 1, pp. 125–139, 2008.

[31] G. Trainiti, J. Rimoli, and M. Ruzzene, "Wave propagation in undulated structural lattices," *International Journal of Solids and Structures*, pp. –, 2016.

[32] F Casadei and J. Rimoli, "Anisotropy-induced broadband stress wave steering in periodic lattices," *International Journal of Solids and Structures*, vol. 50, no. 9, pp. 1402–1414, 2013.

[33] C. Goffaux and J. P. Vigneron, "Theoretical study of a tunable phononic band gap system," *Phys. Rev. B*, vol. 64, p. 075 118, 7 2001.

[34] X. Li, F. Wu, H. Hu, S. Zhong, and Y. Liu, "Large acoustic band gaps created by rotating square rods in two-dimensional periodic composites," *Journal of Physics D: Applied Physics*, vol. 36, no. 1, p. L15, 2003.

[35] H. Yin, L. Sun, and J. Chen, "Magneto-elastic modeling of composites containing chain-structured magnetostrictive particles," *Journal of the Mechanics and Physics of Solids*, vol. 54, no. 5, pp. 975–1003, 2006.

[36] J.-H. Park, S. Lee, J.-M. Kim, H.-T. Kim, Y. Kwon, and Y.-K. Kim, "Reconfigurable millimeter-wave filters using cpw-based periodic structures with novel multiple-contact mems switches," *Microelectromechanical Systems, Journal of*, vol. 14, no. 3, pp. 456–463, 2005.

[37] M. Karim, A. Liu, A Alphones, and A. Yu, "A novel reconfigurable filter using periodic structures," in *Microwave Symposium Digest, 2006. IEEE MTT-S International*, IEEE, 2006, pp. 943–946.

[38] V. Kapko, M. M. J. Treacy, M. F. Thorpe, and S. D. Guest, "On the collapse of locally isostatic networks," *Proceedings of the Royal Society A: Mathematical, Physical and Engineering Science*, vol. 465, no. 2111, pp. 3517–3530, 2009.

[39] R. Hutchinson and N. Fleck, "The structural performance of the periodic truss," *Journal of the Mechanics and Physics of Solids*, vol. 54, no. 4, pp. 756 –782, 2006, ISSN: 0022-5096.

[40] A. Souslov, A. J. Liu, and T. C. Lubensky, "Elasticity and response in nearly isostatic periodic lattices," *Phys. Rev. Lett.*, vol. 103, p. 205 503, 20 2009.

[41] K. Sun, A. Souslov, X. Mao, and T. C. Lubensky, "Surface phonons, elastic response, and conformal invariance in twisted kagome lattices," *Proceedings of the National Academy of Sciences*, vol. 109, no. 31, pp. 12 369–12 374, 2012.

[42] R. Hutchinson, N. Wicks, A. Evans, N. Fleck, and J. Hutchinson, "Kagome plate structures for actuation," *International Journal of Solids and Structures*, vol. 40, no. 25, pp. 6969 –6980, 2003, ISSN: 0020-7683.

[43] D. Symons, R. Hutchinson, and N. Fleck, "Actuation of the kagome double-layer grid. part 1: Prediction of performance of the perfect structure," *Journal of the Mechanics and Physics of Solids*, vol. 53, no. 8, pp. 1855 –1874, 2005, ISSN: 0022-5096.

[44] D. Symons, J. Shieh, and N. Fleck, "Actuation of the kagome double-layer grid. part 2: Effect of imperfections on the measured and predicted actuation stiffness," *Journal of the Mechanics and Physics of Solids*, vol. 53, no. 8, pp. 1875 –1891, 2005, ISSN: 0022-5096.

[45] S. L. dos Santos e Lucato and A. G. Evans, "The load capacity of a kagome based high authority shape morphing structure," *Trans. ASME*, vol. 73, pp. 128–33, 2006.

[46] X. Mao and T. C. Lubensky, "Coherent potential approximation of random nearly isostatic kagome lattice," *Phys. Rev. E*, vol. 83, p. 011 111, 1 2011.

[47] X. Mao, O. Stenull, and T. C. Lubensky, "Elasticity of a filamentous kagome lattice," *Phys. Rev. E*, vol. 87, p. 042 602, 4 2013.

[48] Y. Liu, X.-z. Sun, W.-z. Jiang, and Y. Gu, "Tuning of bandgap structures in three-dimensional kagome-sphere lattice," *Journal of Vibration and Acoustics*, vol. 136, no. 2, p. 021 016, 2014.

[49] Y.-Z. Wang, F.-M. Li, K. Kishimoto, Y.-S. Wang, and W.-H. Huang, "Band gap behaviours of periodic magnetoelectroelastic composite structures with kagome lattices," *Waves in Random and Complex Media*, vol. 19, no. 3, pp. 509–520, 2009.

[50] S. Gonella and M. Ruzzene, "Homogenization and equivalent in-plane properties of two-dimensional periodic lattices," *International Journal of Solids and Structures*, vol. 45, no. 10, pp. 2897 –2915, 2008, ISSN: 0020-7683.

[51] A. Suiker, A. Metrikine, and R De Borst, "Comparison of wave propagation characteristics of the cosserat continuum model and corresponding discrete lattice models," *International Journal of Solids and Structures*, vol. 38, no. 9, pp. 1563–1583, 2001.

[52] A. A. Maradudin, E. W. Montroll, G. H. Weiss, and I. Ipatova, *Theory of lattice dynamics in the harmonic approximation*. Academic press New York, 1963, vol. 12.

[53] M. Born, *Huang dynamical theory of crystal lattices*, 1954.

[54] J. N. Grima, R. Gatt, A. Alderson, and K. E. Evans, "On the auxetic properties ofrotating rectangles' with different connectivity," *Journal of the Physical Society of Japan*, vol. 74, no. 10, pp. 2866–2867, 2005.

[55] F. Haldane, "Model for a quantum hall effect without landau levels: Condensed-matter realization of the "parity anomaly"," *Physical Review Letters*, vol. 61, no. 18, p. 2015, 1988.

[56] Y Zhang, Y. Tan, H. Stormer, and P Kim, "Experimental observation of the quantum hall effect and berry's phase in graphene," *Nature*, vol. 438, no. 7065, pp. 201–204, 2005.

[57] C. Kane and E. Mele, "Quantum spin hall effect in graphene," *Physical review letters*, vol. 95, no. 22, p. 226 801, 2005.

[58] C Kane and E Mele, "Z2 topological order and the quantum spin hall effect," *Physical review letters*, vol. 95, no. 14, p. 146 802, 2005.

[59] B. Bernevig, T. Hughes, and S. Zhang, "Quantum spin hall effect and topological phase transition in hgte quantum wells," *Science*, vol. 314, no. 5806, pp. 1757–1761, 2006.

[60] N Goldman, W Beugeling, and C. Smith, "Topological phase transitions between chiral and helical spin textures in a lattice with spin-orbit coupling and a magnetic field," *EPL (Europhysics Letters)*, vol. 97, no. 2, p. 23 003, 2012.

[61] W Beugeling, N Goldman, and C. Smith, "Topological phases in a two-dimensional lattice: Magnetic field versus spin-orbit coupling," *Physical Review B*, vol. 86, no. 7, p. 075 118, 2012.

[62] F. Haldane and S Raghu, "Possible realization of directional optical waveguides in photonic crystals with broken time-reversal symmetry," *Physical review letters*, vol. 100, no. 1, p. 013 904, 2008.

[63] L. Lu, J. D. Joannopoulos, and M. Soljacic, "Topological photonics," *Nature Photonics*, vol. 8, pp. 821–829, 2014.

[64] V Peano, C Brendel, M Schmidt, and F Marquardt, "Topological phases of sound and light," *ArXiv preprint arXiv:1409.5375*, 2014.

[65] E Prodan and C Prodan, "Topological phonon modes and their role in dynamic instability of microtubules," *Physical review letters*, vol. 103, no. 24, p. 248 101, 2009.

[66] L Zhang, J Ren, J. Wang, and B Li, "Topological nature of the phonon hall effect," *ArXiv preprint arXiv:1008.0458*, 2010.

[67] P Wang, L Lu, and K Bertoldi, "Topological phononic crystals with one-way elastic edge waves," *Phys. Rev. Lett.*, vol. 115, p. 104 302, 10 2015.

[68] T Kariyado and Y Hatsugai, "Manipulation of dirac cones in mechanical graphene," *ArXiv preprint arXiv:1505.06679*, 2015.

[69] A. Khanikaev, R Fleury, S. Mousavi, and A Alù, "Topologically robust sound propagation in an angular-momentum-biased graphene-like resonator lattice," *Nature communications*, vol. 6, 2015.

[70] R Fleury, A Khanikaev, and A Alu, "Floquet topological insulators for sound," *ArXiv preprint arXiv:1511.08427*, 2015.

[71] Z Yang, F Gao, X Shi, X Lin, Z Gao, Y Chong, and B Zhang, "Topological acoustics," *Physical review letters*, vol. 114, no. 11, p. 114 301, 2015.

[72] N Swinteck, S Matsuo, K Runge, J. Vasseur, P Lucas, and P. A. Deymier, "Bulk elastic waves with unidirectional backscattering-immune topological states in a time-dependent superlattice," *Journal of Applied Physics*, vol. 118, no. 6, p. 063 103, 2015.

[73] G. Salerno, T. Ozawa, H. M. Price, and I. Carusotto, "Floquet topological system based on frequency-modulated classical coupled harmonic oscillators," *ArXiv preprint arXiv:1510.04697*, 2015.

[74] R Süsstrunk and S. Huber, "Observation of phononic helical edge states in a mechanical'topological insulator'," *Science*, vol. 349, no. 6243, pp. 47–50, 2015.

[75] M Xiao, W. Chen, W. He, and C. Chan, "Synthetic gauge flux and weyl points in acoustic systems," *Nature Physics*, 2015.

[76] P. A. Deymier, K. Runge, N. Swinteck, and K. Muralidharan, "Torsional topology and fermion-like behavior of elastic waves in phononic structures," *Comptes Rendus Mécanique*, vol. 343, no. 12, pp. 700–711, 2015.

[77] S. H. Mousavi, A. B. Khanikaev, and Z. Wang, "Topologically protected elastic waves in phononic metamaterials," *Nature communications*, vol. 6, 2015.

[78] P. B. Landecker, D. D. Villani, and K. W. Yung, "An analytic solution for the torque between two magnetic dipoles," *Physical Separation in Science and Engineering*, vol. 10, no. 1, pp. 29–33, 1999.

[79] L. M. Nash, D. Kleckner, V. Vitelli, A. M. Turner, and W. Irvine, "Topological mechanics of gyroscopic metamaterials," *ArXiv preprint arXiv:1504.03362*, 2015.

[80] C. Kane and T. Lubensky, "Topological boundary modes in isostatic lattices," *Nature Physics*, vol. 10, no. 1, pp. 39–45, 2014.

[81] R. Zhu, X. Liu, G. Hu, C. Sun, and G. Huang, "A chiral elastic metamaterial beam for broadband vibration suppression," *Journal of Sound and Vibration*, vol. 333, no. 10, pp. 2759 –2773, 2014, ISSN: 0022-460X.

[82] K. H. Matlack, A. Bauhofer, S. Krdel, A. Palermo, and C. Daraio, "Composite 3d-printed metastructures for low-frequency and broadband vibration absorption," *Proceedings of the National Academy of Sciences*, vol. 113, no. 30, pp. 8386–8390, 2016.

[83] P. Celli and S. Gonella, "Laser-enabled experimental wavefield reconstruction in two-dimensional phononic crystals," *Journal of Sound and Vibration*, vol. 333, no. 1, pp. 114 –123, 2014, ISSN: 0022-460X.

[84] R. Zhu, X. N. Liu, G. K. Hu, and C. T.S.G. L. Huang, "Negative refraction of elastic waves at the deep-subwavelength scale in a single-phase metamaterial," *Nature Communications*, vol. 5, p. 5510, 2014.

[85] E. du Trémolet de Lacheisserie, D. Gignoux, and M. Schlenker, Eds., *Magnetism: Fundamentals*. Springer, 2005.

[86] A. J. Petruska and J. J. Abbott, "Optimal permanent-magnet geometries for dipole field approximation," *Magnetics, IEEE Transactions on*, vol. 49, no. 2, pp. 811–819, 2013.

[87] K. W. Yung, P. B. Landecker, and D. D. Villani, "An analytic solution for the force between two magnetic dipoles," *Magnetic and Electrical Separation*, vol. 9, pp. 39–52, 1998.

[88] H. Goldstein, *Classical mechanics*. Addison-Wesley Publishing Company, Inc., 1953, p. 318.

[89] S. S. Rao, *Engineering optimization: Theory and practice*, 4th. John Wiley & Sons, 2009.

[90] F. Bloch, "Über die quantenmechanik der elektronen in kristallgittern," *Zeitschrift für physik*, vol. 52, no. 7-8, pp. 555–600, 1929.

[91] L. Brillouin, *Wave propagation in periodic structures: Electric filters and crystal lattices*. Dover Publications, Inc., 1953.

[92] R. Thurston, "Direct calculation of the group velocity," *Sonics and Ultrasonics, IEEE Transactions on*, vol. 24, no. 2, pp. 109–110, 1977.

[93] A. S. Phani, J Woodhouse, and N. Fleck, "Wave propagation in two-dimensional periodic lattices," *The Journal of the Acoustical Society of America*, vol. 119, no. 4, pp. 1995–2005, 2006.

[94] J. P. Wolfe, *Imaging phonons: Acoustic wave propagation in solids*. Cambridge University Press, 2005.

[95] R. D. Cook, D. S. Malkus, and M. E. Plesha, *Concepts and applications of finite element analysis*, 3rd ed. John Wiley & Sons, 1989.

[96] M. Abramowitz, I. A. Stegun, *et al.*, *Handbook of mathematical functions*, 5. Dover New York, 1972, vol. 1.

[97] J. N. Grima, R. Caruana-Gauci, K. W. Wojciechowski, and K. E. Evans, "Smart hexagonal truss systems exhibiting negative compressibility through constrained angle stretching," *Smart Materials and Structures*, vol. 22, no. 8, p. 084 015, 2013.

[98] W Beugeling, J. Everts, and C. M. Smith, "Topological phase transitions driven by next-nearest-neighbor hopping in two-dimensional lattices," *Physical Review B*, vol. 86, no. 19, p. 195 129, 2012.

[99] R Jackiw and C Rebbi, "Solitons with fermion number $1/2$," *Physical Review D*, vol. 13, no. 12, p. 3398, 1976.

[100] M. Hasan and C. Kane, "Colloquium: Topological insulators," *Reviews of Modern Physics*, vol. 82, no. 4, p. 3045, 2010.

[101] M. Åberg and P. Gudmundson, "The usage of standard finite element codes for computation of dispersion relations in materials with periodic microstructure," *The Journal of the Acoustical Society of America*, vol. 102, no. 4, pp. 2007–2013, 1997.

[102] E. Jones, *Improved digital image correlation*, http://www.mathworks.com/matlabcentral/fileexchange/43073-improved-digital-image-correlation–dic-, 2013.

[103] E. Jones, M. Silberstein, S. R. White, and N. R. Sottos, "In situ measurements of strains in composite battery electrodes during electrochemical cycling," *Experimental Mechanics*, vol. 54, no. 6, pp. 971–985, 2014.

[104] C Eberl, R. Thompson, and D. Gianola, "Free digital image correlation and tracking functions," *Preprint at http://www. mathworks. com/matlabcentral/fileexchange /12413*, 2010.

[105] A. Darnton, "Phase based guided wave methods for damage mapping in multilayered structures," PhD thesis, Georgia Institute of Technology, 2016.

[106] C. Kittel, *Introduction to solid state physics*. Wiley, 2004.

[107] A. J. Cloonan, D. Shahmirzadi, R. X. Li, B. J. Doyle, E. E. Konofagou, and T. M. McGloughlin, "3d-printed tissue-mimicking phantoms for medical imaging and computational validation applications," *3D printing and additive manufacturing*, vol. 1, no. 1, pp. 14–23, 2014.

[108] G. Henkelman and H. Jonsson, "Improved tangent estimate in the nudged elastic band method for finding minimum energy paths and saddle points," *The Journal of Chemical Physics*, vol. 113, no. 22, pp. 9978–9985, 2000.

[109] G. Henkelman, B. P. Uberuaga, and H. Jónsson, "A climbing image nudged elastic band method for finding saddle points and minimum energy paths," *The Journal of Chemical Physics*, vol. 113, no. 22, pp. 9901–9904, 2000.

[110] V. Lasrado, D. Alhat, and Y. Wang, "A review of recent phase transition simulation methods: Transition path search," in *ASME 2008 International Design Engineering Technical Conferences and Computers and Information in Engineering Conference*, American Society of Mechanical Engineers, 2008, pp. 93–101.